

כּוּשֵׁר הַהִתְאֻשְׁשׁוֹת שֶׁל עֲצֵי אֹרֶן יְרוּשָׁלַיִם מִתְקוּפוֹת חוּם וַיּוֹבֵשׁ כְּתָלוֹת בַּמִּשְׁךְ הָעֵקֶה

בַּעֲוֹנָה הִיבְשָׂה

עבודת גמר

מוגשת לפקולטה לחקלאות, מזון וסביבה ע"ש רוברט ה. סמית

האוניברסיטה העברית בירושלים

לשם קבלת תואר

'מוסמך למדעי החקלאות'

על ידי

איתי עוז

ספטמבר 2021

רחובות

אב תשפ"א

Resilience of *Aleppo pine* trees to drought and heat as a function of the duration of the stress period during the dry season

M.Sc. Thesis

Submitted to the Robert H. Smith Faculty of
Agriculture, Food & Environment

The Hebrew University of Jerusalem

For the Degree
'Master of Sciences'

By
Itay Oz

September 2021

Rehovot

This work was done under the supervision of

Prof. José M. Grünzweig

The Robert H. Smith Faculty of Agriculture, Food and
Environment, the Hebrew University of Jerusalem, Rehovot,
Israel

And

Prof. Dan Yakir

Weizmann Institute of Science, Rehovot, Israel

Acknowledgments

I would like to thank my advisors, Prof. Dan Yakir and Prof. Jose Gruenzweig for letting me be part of your research for the past three years. For guiding me through my first steps of my research and for teaching me how to approach the nature science world. For allowing me to do things in my own pace and push me when needed. Dan and Jose, it was a pleasure, I will have nothing but good memories from working with both of you. Thank you.

Thanks to Dr. Eyal Rotenberg, for your willingness to advise, direct and have fruitful and interesting discussions. Working with you has been a significant part of my understanding of environmental science research.

Thanks to Jonathan Müller and Dr. Fyodor Tatrarinov who worked with and without me for many hours on data analysis and other projects of my research.

Thanks to all the Ecophysiology group members with whom I worked throughout the past two years. Rafat, Huan Huan, Rafael, Efrat, Vladislav Dubinin, David, Junjing and Diriba. It was a pleasure working with you.

Thank you Hagai Sagi, Dalia Madhala, Ofra Ashkenazi, Alona Frenkel, Dror Barzilay, Boaz Ninyo-Setter. Except for the fact that you always solved every problem and answered every question, you did so in a welcoming and pleasant way. Thank you all for that.

Special gratitude to Dr. Yakir Preisler and Madi Amer. To Yakir, who pushed me to join the group, guided me in my first steps and all along the way. And to Madi for making the period we worked together much more fun and interesting in every possible way. Thanks for your great help and friendships.

To Ori Ahiman, you taught me a lot and opened my mind for new ideas and ways of thinking. Thanks for the help and support with any issue at any time.

To my current roommates, Amnon, Nitai and Dan. Thanks for the help and advice at any given moment and for making it just more fun to come to work every day.

To the 'Children of the Forest', Revital Weic, Sagi Gotlive, Eitan Ribak, Omri Garini, Yoni Darom, Omer Kessler, Guy Sadot and Ariealla Augenbroun. Who have worked with me over the years, we were a work team that turned every field day into success and pure fun.

I would like also to thank my colleague-friends for fruitful discussions along the way: Avi Gross, Roni Tal and Almog Ram.

To my friends who went through this long path with me, thank you for moments of ease and fun and for your endless support.

To my family, parents and brother. Thank you for always giving me a boost of energy from your love and support.

And last and most important to my partner for life, Lital, who is always there for me, in the good moments and in the bad ones. You have helped me deal with any crisis, professional or personal and you have always done so with the kindness and care that characterizes you.

Abstract

Future climate in the Mediterranean basin is predicted to be hotter and drier, and semi-arid forests in this region represent ‘high-risk ecosystems’ under such scenarios. Consequently, assessing the trees’ resilience to stress becomes increasingly important, but the factors influencing tree recovery from heat and drought stress are largely unknown. The main objective of this study was to evaluate the effect of the duration of the two main environmental stressors in the semi-arid Yatir forest, soil drought (SWC; the ‘supply side’) and atmospheric drought (VPD; the ‘demand side’), on the recovery and resilience of the physiological indicators (photosynthetic net assimilation, A_{net} , Evapotranspiration, E , and branch conductance, g_b). To achieve this objective, we first examined the links between the two stressors to the seasonal cycle of the physiological indicators to better understand the effect of the different stressors on the different physiological parameters.

We have used an automatic branch chambers system to measure leaf gas exchange (LGE) continuously and in-situ in the Yatir forest since 2017. We quantified the patterns of the annual cycles of the environmental stressors together with the different LGE variables (A_{net} , E , and g_b). This allowed us to assess the links of the trees’ recovery time (R_t), recovery rate (R_r), and post-stress peak activity level (Pr) with the antecedent stress duration and intensity. To accurately quantify the LGE variables, we also had to develop a new methodology to estimate effective leaf area using image analysis accounting for self-shading effects inside the branch chambers, which was successfully tested and validated.

The results revealed that the annual cycle of E was strongly linked to that of soil water content (SWC), but that of g_b and A_{net} was more strongly linked to changes in atmospheric vapor pressure deficit (VPD). This resulted in high water use efficiency (WUE; A_{net}/E) during autumn when the stress relief in VPD preceded that in SWC, contributing to the ecosystem resilience. In addition, while R_t correlated with the length of the seasonal stress period, no such correlation was observed for R_r and post-stress peak activity, which were dominated by the concurrent post-stress conditions.

Our results demonstrated that E responded differently from A_{net} and g_b to VPD and SWC. However, the extent of the A_{net} response to VPD remained sensitive to SWC, the latter of which is likely the most critical stress factor in this system. In contrast to previous reports, R_r and post-stress peak activity did not show a ‘legacy effect’ related to the duration and intensity of the

preceding seasonal stress, but, instead, reflected environmental conditions in the subsequent activity period.

האקלים העתידי באגן הים התיכון צפוי להיות חם ויבש יותר בעשורים הקרובים. בתרחיש כזה, יערות צחיחים למחצה באזור זה מייצגים 'מערכות אקולוגיות בסיכון גבוה'. על כן, הערכת חוסן העצים מפני עקות אקלימיות הופכת לחשובה יותר ויותר, אולם בשלב זה המידע אודות הגורמים המשפיעים על התאוששות העצים מתקופות בצורת לא מספק. המטרה העיקרית של מחקר זה הייתה להרחיב את הידע בנושא במאמץ לצמצם פער זה. באופן ממוקד יותר, במחקר זה ביקשנו להעריך את הקשר בין שתי העקות הסביבתיות העיקריות איתם מתמודדים העצים ביער יתיר: בצורת הקרקע (ההיצע) ובצורת האטמוספירה (הביקוש), לבין המחזור העונתי של חילופי הגזים של העצים (פוטוסינתזה, דיות ומוליכות פיוניות). נוסף על כך, הערכנו את ההשפעות של תקופות העקה על דפוסי ההתאוששות והפעילות שאחריה.

כדי להשיג את המטרות הנזכרות לעיל השתמשנו במערכת תאי ענפים אוטומטית למדידת חילופי גזים המודדת באופן רציף ביער יתיר מאז 2017. כימתנו את דפוסי המחזוריים השנתיים של העקות הסביבתיות יחד עם אלה של המשתנים השונים של חילופי הגזים. מדידות אלה אפשרו לנו להעריך את הקשרים בין זמן התאוששות העצים, קצב ההתאוששות ורמת הפעילות בשיא לאחר העקות, לבין אורך ועוצמת העקות שהעצים חוו. כדי לכמת במדויק את הפרמטרים של חילופי הגזים ברמת הענף, פיתחנו שיטה חדשה לאומדן שטח העלים הפעיל. זאת באמצעות ניתוח תמונות המתייחס להשפעות ההצללה ההדדית שנבדקה ותוקפה בהצלחה.

התוצאות הראו כי מחזור הפעילות השנתי של הדיות היה קשור באופן הדוק לזה של תכולת המים בקרקע. ואילו מחזורי הפעילות השנתיים של מוליכות הפיוניות והפוטוסינתזה הראו קשר חזק יותר לשינויים בגירעון לחץ האדים האטמוספרי. התגובה השונה של מרכיבי חילוף הגזים לעקות השונות יחד עם ההקלה בעקת היובש האטמוספרי שקדמה להקלה של עקת יובש הקרקע בתקופת ההתאוששות, הביאו לעלייה ביעילות ניצול המים ובכך תרמו לחוסן המערכת האקולוגית. נוסף על כך, בעוד שזמן ההתאוששות נמצא בהתאמה עם אורך תקופת העקה, לא נצפה מתאם כזה עם קצב ההתאוששות או עם רמת שיא הפעילות שלאחר העקה. אלה נשלטו על ידי התנאים הסביבתיים ששררו באותה העת.

לאורן של התוצאות שנזכרו הסקנו שמרכיבי חילוף הגזים מגיבים באופן שונה לבצורת האטמוספרי ולזו של הקרקע. עם זאת, היקף תגובת הפוטוסינתזה לגירעון לחץ האדים נותר רגיש גם ליובש הקרקע, שהוא ככל הנראה גורם העקה הקריטי ביותר במערכת אקולוגית מוגבלת מים. בניגוד לציפיות ולדיווחים קודמים, מצאנו שרמת פעילות השיא לאחר העקה לא ביטאה 'אפקט מורשת' הקשור לאורך ועוצמת העקה בעונה הקודמת, אלא שיקפה את תנאי הסביבה בתקופת הפעילות שלאחר מכן.

Table of content

Contents

Acknowledgments.....	4
Abstract.....	5
Table of content	7
List of abbreviations	9
1. Introduction.....	11
1.1 Forests and climate change	11
1.2 Leaf gas exchange measurements	12
1.3 Stress intensity, duration, and post-stress recovery	13
1.4 Post-stress recovery framework	15
1.5 Yatir Forest as a model forest for research	17
2. Objectives	18
2.1 Specific objectives.....	18
2.2 Main hypotheses.....	19
3. Methods.....	19
3.1 Site description.....	19
3.2 Environmental variable	19
3.2.1 Soil moisture.....	19
3.2.2 Temperature.....	20
3.2.3 Vapor pressure deficit and potential evapotranspiration	20
3.2.4 PAR	20
3.3 Experimental setup.....	21
3.4 Data processing	22

3.4.1 Data filtering.....	22
3.5 Leaf area measurements	23
3.5.1 Total leaf surface area calculations	24
3.6 Effective leaf area.....	25
3.6.1 Estimating ELA by light attenuation measurements	25
3.6.2 Estimating ELA using image-based calculation.....	25
3.6.3 Estimating ELA by flux attenuation measurements	26
3.6.4 Leaf-scale gas exchange measurement campaign	28
3.7 Leaf Water potential (Ψ_w) measurements	29
3.8 Stress parameters.....	29
3.8.1 Detection of SWC and VPD stress period.....	29
3.8.2 Minimal activity period	29
3.9 Detection of minimal activity period	30
3.10 Detection of recovery time and rate	31
3.11 Statistical analysis	32
4. Results.....	33
4.1 Effective leaf area.....	33
4.1.1 Light attenuation by leaf self-shading	33
4.1.2 Image-based leaf area correction	33
4.1.3 Flux-based leaf are correction	35
4.1.4 Response of WUE to PPFD.....	36
4.1.5 Leaf chamber gas exchange.....	36
4.1.6 Validation of the leaf area correction methods.....	38
4. 2 Environmental conditions and stress period	40
4.3 Recovery parameters, peak activity and WUE.....	44

4.3.1 Leaf gas exchange recovery time and rate.....	44
4.3.2 Yearly trend of WUE.....	46
4.3.3 Leaf gas exchange Recovery rate	46
4.3.4 Leaf gas exchange peak activity and its duration	47
4.3.5 WUE during the peak period	50
4.4 Stress legacy effects on recovery	52
5. Discussion.....	54
5.1 Effective leaf area quantification	54
5.2 Interactions of precipitation patterns, soil moisture, and stress period	56
5.3 The onset of minimal activity period (MAP) in response to SWC and VPD	57
5.4 Recovery from SWC and VPD stress of LGE parameters.....	59
5.5 Possible interactions of recovery parameters and stress period length	59
5.6 Interactions of post-stress peak rates and the stress period length.....	61
5.7 WUE reflects differential environmental effects on the different LGE components.....	62
5.8 Conclusions	63
6. References.....	65
7. Supplementary information	76

List of abbreviations

Soil Water Content	SWC
Potential Evapotranspiration	PET
Precipitation	P

Aridity index	AI
Photosynthetic photons flux density	PPFD
Photosynthetic Active Radiation	PAR
Infra-Red Gas Analyzer	IRGA
Branch level Photosynthesis	Anet
Branch level Evapotranspiration	E
Branch level conductance to H ₂ O vapor	gb
Effective leaf area	ELA
Image-based effective leaf area	ELAP
Flux based effective leaf area	ELAf
Image projected leaf area	IPLA
Total leaf surface area	TLSA
Projected leaf area, fascicle based	PLA_1D
Projected leaf area, needle-based	PLA_2D
Transpirable soil water content	tSWC
Minimal activity period	MAP
Day of year	DOY
Leaf Gas Exchange	LGE
Recovery rate	Rr
Recovery time	Rt
Peak rate	Pr
Peak time	Pt
Water use efficiency	WUE

1. Introduction

1.1 Forests and climate change

Forests cover ~30% of the terrestrial surface area (Bonan, 2008; Dangel, 2016). A recent estimation done by Bastin et al., (2017) suggested that the area covered by dryland forests globally is 40-47% higher than previously estimated, which would increase the total forest area estimation by at least 9%. Climate change-related processes are likely to cause wider areas to fall under the definition of drylands, and accordingly, the dryland forest cover is expected to further increase (Huang et al., 2016). In contrast to the uncertainty regarding the dryland's forest area estimations (Cruz, Quintana-Ascencio, Cayuela, Espinosa, & Escudero, 2017; Gregersen, Lundgren, & Byron, 1998), the importance of dryland's forests and their ecosystem services is well established (Eyal Rotenberg & Yakir, 2010; Griffith et al., 2017; Poulter et al., 2014; Tal & Billig, 2020).

Forests are a crucial component in the Earth's carbon cycle and climate change mitigation efforts. By using the energy of sunlight for photosynthesis, forests sequester nearly 30% of the anthropogenic carbon dioxide (CO₂) emission (Bonan, 2008). As described by Poulter et al., (2014), semi-arid ecosystems play an important role in the interannual variability of the global carbon sink. These authors showed that, particularly in wet years, semi-arid ecosystems act as a large CO₂ sink, thus significantly influencing the concentration of atmospheric CO₂.

Current climate models view the biosphere and atmosphere as a coupled system. Recent studies had shown that an increase in anthropogenic CO₂ emissions and, subsequently, in temperature, caused land vegetation gross primary productivity (GPP) to increase (Haverd et al., 2020). The increase in GPP in response to changing conditions help keep a stable CO₂ "airborne fraction" over the last decades (the ratio of the annual CO₂ increase in the atmosphere to the annual anthropogenic emissions, which is around 0.5) and demonstrates the ability of land and ocean systems to adapt to changing conditions (Raupach, Canadell, & Le Quéré, 2008). Despite the adaptability of terrestrial vegetation, rising temperatures above a certain threshold might lead to a 'tipping point' where the photosynthesis rate starts to decrease, while the total ecosystem respiration (Re) increases. In such a situation, forest ecosystems will transform from a sink to a source of CO₂ to the atmosphere, which, in turn, intensifies climate warming, and further strengthens the decline in vegetation productivity through a negative feedback loop (Duffy et al., 2021). In light of such expectations, a better understanding of the factors influencing the recovery

of plant and ecosystem activities after stress periods can help us estimate the response of the land biosphere to the ongoing climatic changes.

While the warming trend is projected with high certainty for most regions on Earth, the precipitation regime is predicted to be highly variable. However, it is expected that wider areas of the Earth's surface will become warmer and drier in the next decades (Gray, 2007; Jarraud & Steiner, 2012; Masson-Delmotte et al., 2018). Such predictions include the Eastern Mediterranean, and southern Israel in particular. The decrease in the amount of precipitation described by the models often shows a specific pattern of reduction in precipitation at the beginning and end of the rainy season (Evans, 2009; Mariotti et al., 2008; Yu, Roiloa, & Alpert, 2016; Ziv, Saaroni, Pargament, Harpaz, & Alpert, 2014). This pattern will result in an increased length of drought periods accompanied by high temperatures, and thus, longer periods of low soil water content (SWC) together with higher water vapor demand (VPD). As a result, trees have narrow 'windows of opportunity' for effective carbon assimilation, which is vital to maintaining metabolic functioning under drought (Freeman, 1980; Martínez-Vilalta, Piñol, & Beven, 2002; Väänänen, Osem, Cohen, & Grünzweig, 2020). Klein et al., (2015) showed that at the end of the dry season, both photosynthesis and respiration fluxes are low at least partly due to low carbon pools (Klein & Hoch, 2015), which indicate that further prolonging the dry season may lead to depletion of reservoirs and finally to mortality by "starvation".

Trees growing in semi-arid environments already experience such a narrow window of opportunity to accumulate carbon (Wang, Gitelson, Sprintsin, Rotenberg, & Yakir, 2020), and therefore their fast and efficient recovery at the end of the stress period is of great importance for their survival. The importance of productivity recovery after stress (e.g., heat waves) during the growing season was recently demonstrated at the ecosystem level in Yatir forest - a semi-arid pine forest (Tatarinov et al., 2016). This study estimated that the contribution of the recovery period (October - December) contributes $\sim 13 \pm 1.8\%$ of the annual carbon gain.

1.2 Leaf gas exchange measurements

Ecophysiological research critically relies on measurements of physiological activities which often includes continuous, branch-level gas exchange measurements (Bamberger et al., 2017; Birami et al., 2018a; Breuninger, Oswald, Kesselmeier, & Meixner, 2012; Kooijmans et al., 2017; Preisler, 2020; Tuovinen, 2006). These kinds of measurements provide us with a high-resolution time series

of environmental and gas-exchange variables. However, despite its routine use, a major challenge in branch-chamber gas exchange measurements remains, which is to correctly estimate the active leaf area enclosed in the measuring chamber. The challenge stems from the fact that inside the branch chambers, the spatial organization of the twigs involves mutual shading. This requires, in turn, consideration of the complex needle and twig geometry and arrangement in space. Previous studies demonstrated the effect of canopy structure on PAR penetration to the inner and lower parts of the canopy (Arthur Sampson & Smith, 1993; Navrátil, Špunda, Marková, & Janouš, 2007). Such studies were the basis for the assumption that reliable quantification of the leaf area is also required at the branch chamber scale to improve the accuracy of our flux quantification. A recent study reinforced this by showing that even when sunlight is abundant in ecosystems such as Yatir forest, PPFD may still be a limiting factor for leaf gas exchange, both at the stand and the leaf level (Tsamir et al., 2019). Because of its importance and the lack of a standard approach in previous studies (Nogués et al., 2001; Speckman et al., 2015; Birami et al., 2018), efforts must be invested in correctly quantifying the effective leaf area in ecophysiological studies.

1.3 Stress intensity, duration, and post-stress recovery

The significant contribution of the recovery period to the ecosystem's annual productivity, together with forecasts for increasing stress periods, highlight the importance of resilience, and the trees' ability to both endure and recover from long hot and dry periods. Resilience is a key concept in ecology, which describes the ability to maintain a certain state and recover from disturbances (Ingrisch & Bahn, 2018). Although the importance of resilience is clear under ongoing climate change, the factors influencing recovery from, for example, drought stress and its spatiotemporal patterns are largely unknown (Schwalm et al., 2017).

While plant responses to heat and drought stress have been studied intensively (Grossiord et al., 2020; Klein et al., 2016; McDowell et al., 2008; Salmon et al., 2018), post-stress recovery and resilience received less attention. So far, studies that involve tree recovery and resilience have been conducted mainly in controlled conditions on young seedlings, to ensure that the pre- and post-stress conditions are the same (Birami et al., 2018; Brodribb & McAdam, 2013; Posch & Bennett, 2009). The framework of the controlled conditions studies included quantification of the activity before the stress period (Bs), during stress (S), and after the stress period (As). Those parameters were used to quantify the stress intensity (Bs-S), post-stress recovery (As-S), and

resilience (As/Bs). Such knowledge on the recovery and resilience of woody plants is only beginning to accumulate, and research under field conditions and in mature trees is still scarce (Ruehr et al., 2019). The stress effects on the subsequent recovery and resilience in a natural condition are often opportunistic (e.g. heatwaves) and post-event environmental conditions might have significant effects on estimating the recovery post-stress activities (Ruehr et al., 2019). Few studies have dealt with the recovery and resilience of mature trees in field conditions. In order to quantify the recovery and resilience those studies have used the framework of controlled condition experiments, this fact limits the ability to draw conclusions about the trees ability to recover and their resilience due to changing environmental conditions between seasons (Lloret, Keeling, & Sala, 2011; Serra-Maluquer, Mencuccini, & Martínez-Vilalta, 2018). The lack of studies on resilience and recovery in general, and field studies under natural conditions in particular, highlight the need for comprehensive, long-term field research to fill this knowledge gap.

Characterizing the ability of ecosystems and trees to recover from stress can be based on different variables, which are generally divided into structural and functional variables. The structural variables at the ecosystem level include the ecosystem “ecological state”, that is, the species composition, the species richness, the physical characteristics, and the functioning level of the ecosystem (Ingrisch & Bahn, 2018; Nimmo, Mac Nally, Cunningham, Haslem, & Bennett, 2015). The main functional variables are gross primary production (GPP) and net primary production (NPP), leading to growth and biomass accumulation (Lloret, Keeling, & Sala, 2011; Stuart-Haëntjens et al., 2018). At the tree level, physiological (functional) variables are more commonly used than structural ones. Such parameters include net photosynthetic carbon assimilation (A_{net}), evapotranspiration (E), stomatal conductance (g_s), leaf water potential (ψ_w), photosystem II activity (PSII), abscisic acid concentration (ABA), nonstructural carbohydrate concentration (NSC) in different organs, and leaf conductance (G_{leaf}) (Ruehr et al., 2019). In this study, we used A_{net} , E , and branch conductance (g_b) to assess recovery and post-stress activity levels.

Environmental conditions directly affect tree physiological activity. Trees mediate their gas exchange with the atmosphere mainly through the stomata, which help maintain hydraulic integrity while optimizing carbon uptake according to the environmental conditions (William R.L. Anderegg et al., 2018; Tyree & Sperry, 1989). As illustrated in Fig. 1, environmental stress causes a decrease in the rate of physiological parameters. This decrease reflects the change in

physiological activities according to the stress exerted on the plant. The recovery phase from stress is separately treated, and can be influenced by the intensity of the stress (i.e. how low the activity declines) and the length of the stress period, but can also be independent of the precedent stress, being influenced by the actual conditions during recovery and the subsequent non-stress period. The combination of these effects would determine the extent of recovery (or mortality) and, in turn, the resilience of the ecosystem (the ratio of activity after recovery to that before the onset of the stress). Disturbances of sufficient magnitude or duration can also profoundly affect a plant or ecosystem's recovery time and rate, which has to be considered separately. In semi-arid ecosystems, characterized by prolonged periods of low water availability, accompanied by high water vapor demand, it is yet unclear if the observed interannual variability in the overall stress impact is dominated by the length of the 'stress period' or the 'recovery conditions'.

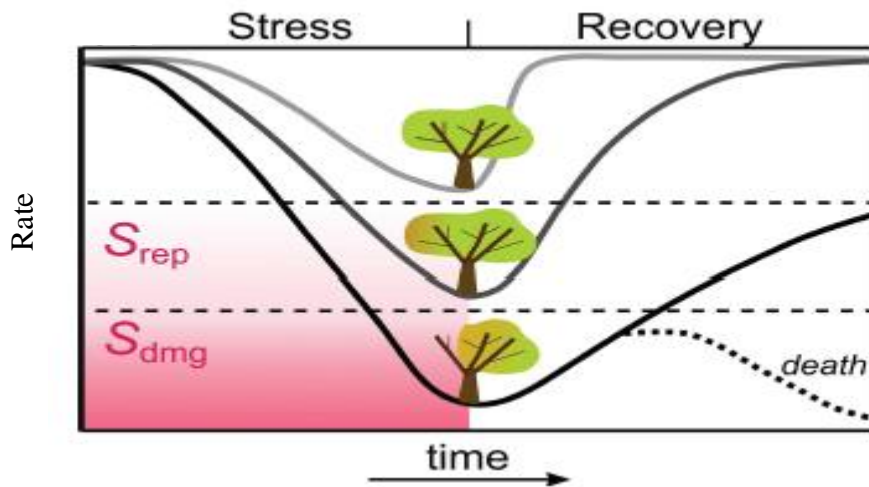


Figure 1. Example of a typical course of decline and recovery for a certain physiological parameter activity rate caused by stress over time. Different stress level showed by the different lines in different shades of gray. Horizontal dashed lines separate between different stress levels. S_{rep} – Repairable damage S_{dmg} – non-repairable damage (Ruehr et.al 2019).

1.4 Post-stress recovery framework

Investigating the effect of stress on post-stress recovery requires a formal framework to assess and quantify observations. A possible approach, adopted here, is to quantify the length of the stress period based on soil moisture (SWC, the supply side controlling plant activity), and atmospheric evaporative demands (VPD; the demand side). These two environmental stressors are considered the main factors that limit trees' physiological activity in a water-limited environment (Birami et

al., 2018a; dos Santos et al., 2013; Preisler, 2020), and the minimal activity period of the different components of leaf gas exchange (LGE).

The independent quantification of the stress and the recovery period allows us first, to examine the relationships between the length of the ‘environmental stress period’ and the actual length of the ‘minimal activity period’ (MAP), and second, to examine the relationship between the length of MAP and the subsequent indicators of recovery, mainly physiological activities (e.g., LGE).

To advance this approach, a formal set of definitions is a critical tool to complement the conceptual scheme presented in Fig. 1. Such an extension, which is increasingly being used in ecosystem research related to climate change (Camarero et al., 2018; Ingrisich & Bahn, 2018; Lloret et al., 2011) is presented in Fig. 2. In this framework, and in order to independently quantify the environmental stress and activity parameters, we propose to define terms that describe the stress cycle separately from those describing the activity cycle.

In Fig. 2 we first define the key parts of the seasonal cycle, which include the ‘*peak activity*’: the 90th percentile of the annual data for a given LGE parameter. ‘*Peak activity period*’: the time between the first and the last day of the ‘peak activity’ (first and fourth stages, Fig.2). After the peak activity period, the stress effects start to build up, physiological activity decreases, and the ‘*low activity period*’ begins. Within the ‘low activity period’ is the ‘*Minimal Activity Period (MAP)*’, when the actual physiological activity is at its annual minimum (\leq lowest 60 days running mean; Fig. 2). The 60-day time window was chosen to balance the identification needs of the activity during the summer period, on the one hand, to represent the summer period in a general enough way that the identification is not sensitive to "spikes" in the data but on the other hand not too wide and includes days of activity outside the dry period. MAP is followed by the ‘*Activity restoration*’: the day when activity exceeds the lowest 60-days summer mean in two or four standard deviations, depending on the noise of the dataset (see methods 3.9) and the ‘*recovery period*’: the time between ‘activity restoration’ and start day of ‘peak activity’, which is the transition point between recovery and the second peak of activity (phases three and four) (Fig. 2). The ‘*low activity period*’ defined above was based on ‘functional parameters’ (LGE). However, it also includes the high-stress periods imposed by the two main ‘environmental stressor’, the ‘*maximal VPD period*’: the period when $VPD \geq$ summer VPD mean; and the ‘*dry season*’: when $SWC <$ transpirable SWC limit (which do not necessarily overlap; (Klein et al., 2014). These ‘environmental stressors’ also help define the ‘*stress onset*’ and ‘*stress relief*’: the start and end

dates of the ‘maximal VPD period’ and ‘dry season’ (with both the ‘maximal VPD period’ and ‘dry season’ are within the ‘stress period’; Fig. 2).

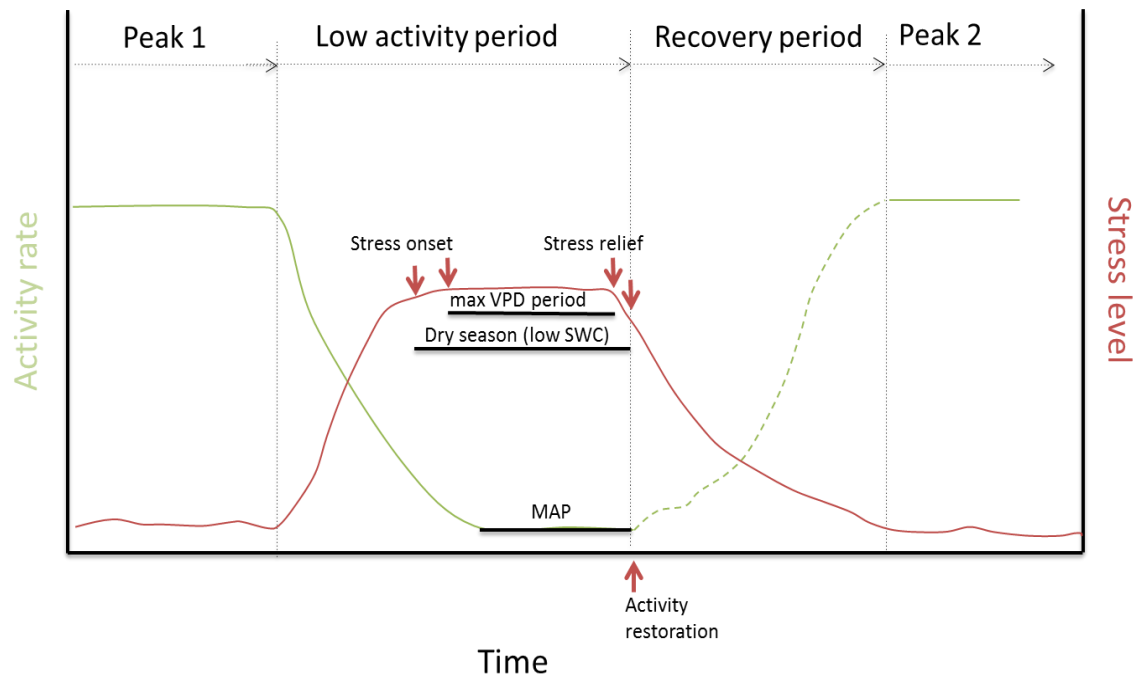


Figure 2. Schematic diagram of the activity and stress cycle and its stages: 1) Peak activity of a given year (Peak 1 and 2). 2) Low activity period stress period, within this time period is the minimal activity period of the different LGE variables (MAP) in black line. 3) Recovery period (dashed red line).

Once we have quantified the parameters illustrated in Fig. 2, including the main parts of the seasonal cycle, and its partitioning to the different functional and environmental stress and recovery components, it will be possible to examine the links between the length of the environmental stress period and the post-stress recovery and activity of trees under field conditions

1.5 Yatir Forest as a model forest for research

Yatir forest provides a useful research site as a “model” semi-arid forest for several reasons. First, the Yatir forest is a forest dominated by Aleppo pine (*Pinus halepensis*), which is one of the most common tree species in the dry Mediterranean region (Klein, 2020). Second, this is one of the driest pine forests in the world, with an aridity index (AI) of 0.22 (Amer, 2020), allowing us to understand the effect of the length of the stress period on the resilience of trees in extreme conditions that are expected to develop in additional regions under climate change. Finally, the

natural conditions at the site include a well defined long drying season (with no rain), and a re-wetting rainy period, without the complications due to groundwater (300 m deep at the site), which allows long-term examination of the factors influencing the resilience to drought in mature trees. To use the unique conditions of Yatir Forest to examine the effect of stress duration on the recovery at the tree level, an extensive system was established a few years ago for in-situ LGE measurements at the branch level providing continuous data of A_{net} , E and g_b (Preisler, 2019).

2. Objectives

The dry Mediterranean region is characterized by a long, hot, and dry summer. Trees' resilience to such a stressful period, which may be exacerbated by climate change, can greatly influence their productivity and survival. The main objective of this study was to evaluate the effect of the duration of the two main environmental stressors in the semi-arid Yatir forest, soil drought ('supply side') and atmospheric drought ('demand side'), on the recovery and resilience of physiological indicators. To achieve this overall objective, we carried out extensive gas exchange measurements in the Yatir semi-arid pine forest accompanied by continuous measurements of environmental conditions.

2.1 Specific objectives

- To differentiate between the environmental stress levels induced by soil and atmospheric drought, and to assess their differential effects on the different leaf gas exchange variables.
- To quantify leaf gas exchange rate under maximal stress effect during the dry season of each year, and to develop quantitative indicators to identify the onset of the recovery from seasonal drought.
- To develop and apply new indicators to assess the factors influencing the timing, rate, and extent of recovery of different components of leaf gas exchange after stress removal.
- To improve estimates of the rates of CO_2 and water vapor gas exchange at the branch scale by quantifying the effective leaf area in branch measurements under field conditions.

2.2 Main hypotheses

H1. The duration and intensity of the seasonal drought stress period influence the timing and rate of the recovery, but not its extent (i.e resilience) of leaf gas exchange recovery after the stress relief.

H2. The different components of leaf gas exchange (photosynthesis, transpiration, and branch conductance) will respond differently to the relief of the different drought stressors (SWC, VPD).

3. Methods

3.1 Site description

The study was carried out in Yatir forest (31° 20' N; 35° 30' E; 600–900 m above sea level; 2800 ha) (Preisler, 2020; Wang et al., 2020), a 55 years old, semi-arid forest dominated by Aleppo pine (*Pinus halepensis* s Mill.). The forest was mainly planted in the mid-1960s (Tatarinov et al., 2016), making it almost completely age- and species-uniform. The study area density was 320 trees per hectare, the mean tree diameter was 19.4 (\pm 0.4) cm and the mean tree height was 11.8 (\pm 1.2) m (Preisler, 2020). The average leaf area index is about 1.70 ($\text{m}^2 \text{m}^{-2}$) (Sprintsin et al., 2011). The soil is mostly composed of light brown Rendzina, 25–100 cm deep. The roots are mostly concentrated in the upper 60 cm and the main fine root zone is between 20-40 cm layer (Grünzweig, Gelfand, Fried, & Yakir, 2007; Preisler, 2014). The forest is located at the northern edge of the Israeli Negev desert, an area with average precipitation (P) of $279 \pm 90 \text{ mm yr}^{-1}$ and potential evapotranspiration (PET) of 1600 mm yr^{-1} (Preisler, 2020), resulting in a low aridity index ($\frac{P}{PET}$) of 0.22 (mean values for 1970–2018) (Amer, 2020). The forest area is characterized by a prolonged dry period that can vary between 200-340 days with no rain (Preisler, 2020). In the course of the dry season, mean soil water content (SWC) drops to 5-10% at 10 – 40 cm depth, while vapor pressure deficit (VPD) can rise up to a daily maximum of ~8.5 KPa in July. In the wet period, mean SWC rises to 35% and VPD decreases to maximum daily values of ~2 KPa in January.

3.2 Environmental variable

3.2.1 Soil moisture

Volumetric SWC profile (10-100 cm) was monitored since August 2016 to date, using five access tubes per plot (PR2/6, Delta T Devices, London, England). In the irrigated plot, 4 short sensors

(10-40 cm) and one long sensor (10-100 cm) were positioned in a way that represented the different distances from the drippers. In the control plot, 5 short sensors were placed. In both plots, the sensors were placed in a way that best represented the heterogeneity of the plot. Gravimetric SWC was measured by weighing the soil samples in the field, drying them in the laboratory oven and re-weighing after drying to obtain a depth- and pit-specific calibration curve. To best represent the water availability to the trees, the average SWC of the main rooting zone (10-40 cm) (Preisler et al., 2019) was used.

3.2.2 Temperature

The temperature of the air as close as possible to the needles was measured continuously in all branch chambers (see below) using custom-made type T (Copper/Constantan) thermocouples (REOTEMP Instrument Corporation, San Diego). The data was stored in AM-25 data logger (Campbell Scientific, Logan, USA). We measured air rather than leaf temperature due to technical difficulties of measuring the temperature of the ~150 needles in the chamber.

3.2.3 Vapor pressure deficit and potential evapotranspiration

VPD was calculated as the difference between the partial water vapor pressure at saturation and the partial water vapor pressure in the air surrounding the leaves.

$$VPD = es - el \quad (1)$$

where es is the water vapor partial pressure at saturation (Pa) and el the water vapor partial pressure in the air surrounding the leaves (Pa) (Buck Arden L., 1981). The partial pressures was derived from the thermocouple in the measuring chambers (see above) and the humidity measured by the IRGA.

PET was calculated by the Priestley-Taylor equation (Priestley & Taylor, 1972). In our study, the values of the parameters of the equation were calibrated by the measured data from the Yatir fluxnet station (Eyal Rotenberg & Yakir, 2010; Tatarinov et al., 2016).

3.2.4 PAR

Photosynthetic photon flux density (PPFD) was measured continuously since July 2020 with 8 sensors (Apogee SQ-500, North Logan, USA), 4 in each plot. The PPFD sensors were placed on an articular arm outside but at the height of the chambers to measure the total incoming PPFD without casting shade on the leaves. To correct the incoming PPFD values to those reaching the needles inside the chambers a calibration curve was created (Fig. s12, s13). Logbook reporting the

integrity of the sensors was filed every week, and bad data was removed in the final data analysis code (J. D. Muller & Oz, 2021).

3.3 Experimental setup

The branch-scale gas exchange experiment included 15 custom-made branch chambers designed to function under harsh field conditions, modified from previous studies (Bamberger et al., 2017; Pumpanen, Heinonsalo, Rasilo, Hurme, & Ilvesniemi, 2009). The chambers were made of a transparent Perspex cylinder enclosed from both sides with doors that can be opened and closed to remove and insert the branches from one side and to close the chamber while measuring at the other side (inner volume: 11.2 L). Each chamber contained a self-made type-T thermocouple for temperature measurements (see above), a small 12 V electronic fan (JAMICON, Belmont, USA) for air circulation in the chamber, and a PPF sensor (Apogee SQ-500) located next to the chambers – available since July 2020.

The chambers were located at mid-canopy (~6m) in two adjacent plots: a manipulation plot (irrigated) and a control (natural condition), with a buffer area of ~ 10 m separating between them (Fig. s1 & s2). In each plot, each of the six measuring chambers contained four twigs, while one empty chamber located in the buffer area served as a reference to constantly examine the chamber effect (blank). In each plot, the chambers were placed on different sides of the canopy to best represent the heterogeneity of the mid-canopy. The chambers were normally open except for the measurement time of 240 seconds, once per hour. To capture the temporal heterogeneity of the fluxes in the chambers, a CR-basic program on a CR1000 datalogger (Campbell Scientific, Logan, USA) was used to randomize the order of chambers closing and solenoid (Baccara, Geva, Israel) opening to allow measurement of one chamber at a time. To sample the air from the measuring chamber and the reference chamber at the same time, two air pumps (KNF, Philadelphia, USA) were used to simultaneously pump air from the two sources at the same flow rate (~9 liter per minute) through the Dekabon ¼ inch tubes (Eaton, ¼ inch; Dekabon, California, USA) of the same length (~25 m), a 1 µm filter (Campbell Scientific, São Paulo –SP, BRASIL), the pumps, a flow meter (TSI 4140/4143, Shoreview, Minnesota, USA), a buffer tube (to reduce pressure fluctuations), and using a vent split and a mass flow controller (ALICAT Scientific, Arizona USA) to reduce the flow rate to 1 L/min into the Infra-Red Gas Analyzers. The parallel measurement of ambient and sample H₂O and CO₂ concentrations was done using a setup that consisted of two

IRGAs, one for ambient air (LI-840A, LI-COR, Lincoln, Nebraska) originating from the reference chamber, and the other one for sample measurements originating from the branch chambers (LI-7000). The LI-7000 was used in the differential mode, with the sample air measured against the ambient air after it passed through the LI-840 analyzer. This allowed us to obtain both the absolute H₂O and CO₂ concentration values and achieve the high sensitivity and precision required for the branch gas exchange measurements. More detail and a diagram of the measurement system were provided in the appendix (Fig. s3).

Weekly based maintenance of the branch chambers included cleaning them with distilled water and soft tissue paper, and cleaning and leveling of the PPFD sensors. Monthly based maintenance included leaf area (LA) measurements (see below) for each chamber and checks of irrigation record and function. Once every 6 months we calibrated the two IRGAs (LI-840A & LI-7000) with 99.999% N₂ for zero and a lab standard cylinder with known CO₂ concentration (checked annually by NOAA, Boulder, CO, USA) for span, and a dew point generator (LI-610) for H₂O calibration.

The data from our measurement system, including gas concentrations, flow rate, temperature, PPFD, etc. as listed in Table S.4. The data was recorded every two seconds using a CR1000 datalogger (Campbell Scientific, Logan, USA), with a raw data file created and stored every hour.

3.4 Data processing

3.4.1 Data filtering

Within the 240 seconds of the chamber measurement period, we accounted for the flushing time of the air from the previous chamber and the time required to reach a new steady-state (Fig. s4). Based on extensive testing, this was set to 210 seconds (Preisler, 2020), thus using the average values of the last 30 seconds of each measurement cycle for the gas exchange calculations. Data for periods of known technical problems, and time with indications of dew formation condition, and occasional data spikes were removed. See detailed filtering parameters in the final analysis script (Muller J and Oz I, 2021).

3.4.2 Data based calculations

Transpiration (E) and photosynthesis (Anet) fluxes were calculated from the differences in the H₂O and CO₂ concentrations between the sample and reference chambers. The calculations were performed using the following equations (von Caemmerer & Farquhar, 1981):

$$E = \left(\frac{f \Delta H_2O}{LA(1-h)} \right) 10^3 \quad (2)$$

$$A_{net} = (f \Delta CO_2 / LA + C_s E) 10^6 \quad (3)$$

where ΔH_2O (mol mol⁻¹) and ΔCO_2 (mol mol⁻¹) are the differences in the concentrations between the ambient and sample air; f represents the flow rate from the sample pump, expressed as the volume of air in moles (mol s⁻¹), LA is the leaf area (m²) and h is the ambient H₂O ambient concentration (mmol H₂O/ mol air). A_{net} was corrected for the dilution via the outgoing transpiration fraction ($C_s E$) from the leaves where C_s is the ambient CO₂ concentration (von Caemmerer & Farquhar, 1981).

Branch conductance (g_b in mol m⁻² s⁻¹) was then computed as follows:

$$g_b = \frac{E \left(\frac{1000 - e_l + e_a}{2} \right)}{e_l - e_a} \quad (4)$$

where e_l is the molar concentration of water vapor within the leaf (mmol H₂O / mol air), which is computed from the leaf temperature T_l (°C) and the total atmospheric pressure P_a (kPa) as follows:

$$e_l = \frac{e^{T_l}}{P} \cdot 1000 \quad (5)$$

The function e^{T_l} is saturation vapor pressure (kPa) at temperature T (°C), e_a is the water concentration in the ambient air plus the H₂O molecules added by transpiration (mmol H₂O/ mol air) (Preisler, 2020). See further and detailed calculations in the analysis script (J. D. Muller & Oz, 2021). The final data output was hourly averaged to include all chambers of each plot within the smallest time window possible.

3.5 Leaf area measurements

Estimating gas exchange fluxes using a branch gas exchange system is challenging from two main aspects. First, needles are arranged in fascicles, in our case, two needles per fascicle. The two needles form one perfect cylinder but are often split. Therefore leaf area can be calculated in

different ways (see Table.1, 1-3), but an “effective leaf area” (ELA) is required to accurately calculate leaf gas exchange. Second, the needles on the twig and the twigs in the branch are organized in a complex spatial array, with significant self-shading, which must be accounted for. Estimating the ELA is, in fact, an attempt to make the branch gas exchange measurements comparable to more conventional single and flat-leaf gas exchange measurements. Because no established method was available to estimate ELA in needle-leaf branch chambers studies, we made extensive efforts to develop such an approach and validate it.

3.5.1 Total leaf surface area calculations

Leaf area was measured every month for every chamber specifically. For each chamber, we harvested one twig adjacent to the chamber to represent the twigs in the chamber in the best possible way, without the need to harvest and change the twig every month. To obtain the total leaf area for the four twigs in the chamber, the measured leaf area calculated for one twig was multiplied by four.

The average needle length and the number of fascicles were recorded for each twig every month, average needle diameter was measured once for each year and plot. The fact that two needles on one fascicle form almost a perfect cylinder make the effective surface area calculation relatively simple.

In one approach, we estimated the total cylinder surface area of the two needles, and cross-section surface area (accounting for the flat surface of the 2-needle; see Fig.s5) using the following equation:

$$TLSA = ((D\pi l) + (Dln)) \cdot N \quad (6)$$

where $TLSA$ is the total leaf surface area D is average needle diameter (m), l average length of the needle in the chamber(m), n is the number of needles in the fascicle (in our case $n=2$) and N is the number of fascicles per twig (Fig. s5).

An alternative way is often used to calculate leaf area for flux calculation is based on the ‘projected leaf area’. In this case, we simply used the fascicle cross-section area, based on the needle diameter and length, i.e., $D \cdot l$ (Birami et al., 2018b; Grace, 1987; Speckman et al., 2015). However, for the projected leaf area calculation we can consider two ways of calculation. One uses the fascicle as the basic unit for the calculation assuming that the two needles are tightly coupled into one cylinder, which we will refer to as method 1D (1 diameter). The other approach uses the needle as

the basic unit for the calculation assuming there is no tight coupling between the needles within the fascicle and both needles are exposed to incoming PAR, and we will refer to this method as 2D (2 diameter).

$$\text{Projected area 1D (m}^2\text{)} = D \cdot l \cdot N \quad (7)$$

$$\text{Projected area 2D (m}^2\text{)} = D \cdot l \cdot N \cdot n \quad (8)$$

where N is the number of fascicles and n is the number of twigs in each fascicle.

3.6 Effective leaf area

3.6.1 Estimating light attenuation by needles inside the branch chamber

PPFD attenuation by increasing leaf self-shading was quantified using two Apogee SQ-500 PPFD sensors. The sensors were placed outside and inside an empty chamber to measure incoming PPFD and PPFD at the bottom of the chamber. Data from both sensors was used to calculate light intensity attenuation by the branches inside the chamber, as the change in PPFD fraction ($\frac{\text{PPFD at the botom sensor}}{\text{incoming PAR}} * 100$) reaching the leaves. The longitudinal side of the chamber was oriented north-south to prevent self-shading from the chamber on the PPFD sensors (Fig. s6). We compared the values of the two sensors before the experiment started to make sure there was no difference between them. The experiment included 6 repetitions, each one started with 4 branches, and every 2 minutes one branch was removed. The data used for PPFD fraction comparison was the two minutes average for the different leaf area classes (0, 0.02, 0.05, 0.07 and 0.09 m²) (n=6). After each round of measurements, we checked to make sure there were no changes in leveling and positioning of the sensors. Note that the attenuation included that of the chamber itself, which was constant, and the calculation relied on the change due to different numbers of leaves.

3.6.2 Estimating ELA using image-based calculation

After establishing the fact that mutual shading has a significant effect on light attenuation, we used the twigs as they are arranged in the branch chamber to quantify the light-absorbing leaf area. This effective leaf area quantification method was based on the photographed shadow cast by the four twigs on a white wooden board next to a measuring tape to later estimate the area. Four different chambers, two from each plot, were used in this experiment. The twigs were taken out from the chamber as they lay in it to represent the mutual shading as it occurs in the current arrangement of the twigs in the chamber. Every four twigs' shade was photographed from a distance of ~50 cm to

maintain the uniformity proportion for all images and from 3 different angles (45°, 90°, and 135°) to simulate the movement of the sun during the day. The images were corrected for perspective and objects that appeared in the picture and we did not want to identify as our object (the shadow from the needles) were painted in the color of the background (GIMP 2.10.20 software). To remove the woody part of the twig from further analysis we calculated its area as follows:

$$\text{Woody area} = D\pi l \quad (9)$$

Where D is the average diameter and l is the total length of the woody part for the four twigs. We used machine learning software (Ilastik software) to differentiate between shade and background and to generate a matrix of pixels with values of 2 or 1 where 2 is the background and 1 is the object. The final calculation of the leaf area was as follows:

$$IPLA = \left(\text{Total area} \cdot \frac{\text{Object pixels}}{\text{Total pixels}} \right) - \text{Woody area} \quad (10)$$

Where $IPLA$ is the image projected leaf area, Total area is the photographed area calculated from converting pixels to the area using the measuring tape, $Object\ pixels$ is the amount of pixels value = 1, $Total\ pixels$ is the amount of pixels value = 2 and Woody area is the calculate woody area (eq.11). More detail and demonstration of the photos, corrections, and products of the machine learning software was provided in the appendix (Fig. s8 and 9). The final IPLA result was the average of the 3 angles. We used the data from all four chambers to create a linear function ($y=ax+b$) that described the relationship between the leaf area (x) and the ratio between leaf area and IPLA (y). The linear function was used to obtain y -values for each given Leaf area and use it to obtain ELA_p according to:

$$ELA_p = \frac{\text{Leaf area}}{y} \quad (11)$$

where ELA_p is the image-based effective leaf area, leaf area is the measured leaf area in m^2 and y is the ratio of leaf area to IPLA.

3.6.3 Estimating ELA by flux attenuation measurements

To quantify the mutual shading effect on the gas exchange rate we measured H_2O and CO_2 fluxes in several chambers from the irrigated plot ($n = 4$, 2 shaded and 2 lit) while reducing the leaf area inside the chamber in a step-wise manner, from 4 to 0 twigs, removing one twig at a time.

The campaign was conducted on several dates ($n = 5$) between September and November 2020 between 10:00 to 14:00 to minimize the variation of the incoming PPFD reaching the measuring chamber. Each chamber and twigs amount measurement lasted 240 seconds to reach a steady state. In addition, chambers were flushed with ambient air for 4-8 minutes after changing branches. On each day of measurements, we measured all four chambers with all twigs amount (0-4 twigs, a total of 5 measurements per chamber). The branches were removed from the bottom twig to the upper twig and for each one removed we measured its leaf area and binned the results to five different leaf area categories (0 - 0.08 m² with 0.02 steps).

The analysis of the flux attenuation by increasing self-shading was done separately for lit and shaded chambers. Classification of shaded or lit was done according to the incoming PPFD as follows: shaded chambers were defined as chambers exposed to PPFD below half of the saturation value and lit chambers were defined as chambers exposed to PPFD above saturation. To find the PPFD saturation point for both Anet and E, the data set of September-November 2020 from the branch chamber (irrigated plot) was used and filtered for the non-limiting condition of VPD and temperature. The saturation value was defined as $F'(X) < 0.001$ for the fitted curve of the data set (curve expert software) (Fig. s15). Chambers with high VPD or PPFD variation during the flux measurement was filtered out, thresholds were maximum difference of 150 $\mu\text{mol m}^{-2}\text{s}^{-1}$ for PPFD and 1 KPa for VPD (Table s3). The ratio between the fluxes calculated with maximum to minimum LA inside the chamber was used to correct the leaf area.

$$ELA_f = \frac{\text{flux with min LA}}{\text{flux with max LA}} \quad (12)$$

Where ELA_f is the flux-based effective leaf area, *flux with min LA* is the measured flux with the minimum LA and *flux with max LA* is the flux with the maximum LA for a given chamber.

Table.1 summarizes the three different leaf area calculation methods (TLSA, PLA1_D, and PLA_2D) and the two leaf area correction methods for effective leaf area (ELA_p and ELA_f).

Table 1. Leaf area calculation and correction summary

Method	Acronym	Equation	Notes
Total leaf surface area (m ²)	TLSA	$TLSA = ((D * \pi * l + D * n * l)) * (N)$	The area based on the cylinder formed from the two needles together with the two inner surfaces of each needle separately
Projected LA 1D (m ²)	PLA_1D	$PLA_{1D} = D * l * N$	Projected area of fascicle (1 diameter for two needles)
Projected LA 2D (m ²)	PLA_2D	$PLA_{2D} = D * l * N * n$	Projected area of needle (1 diameter for one needles)
Image based correction for effective leaf area	ELA _p	$ELA_p = \frac{\text{Projected LA 2D}}{y}$	We use y (the value obtained from solving the linear equation) to correct the measured value for the mutual shading. $y = 37.21X + 0.46$ and X is the projected LA (2D)
Image based correction for effective leaf area	ELA _f	$ELA_f = LA \cdot \text{correction factor}$	Measured leaf area multiplied by specific correction factor derived from the ratio of flux with min to flux with max leaf area.

3.6.4 Leaf-scale gas exchange measurement campaign

A one-day campaign of measurements with a portable photosynthesis system (LI-6400XT, LiCor Bioscience, Lincoln, NE, USA) was carried out. The Li-cor 6400 system relies on exact leaf area with no self-shading and therefore served as a benchmark for our branch chamber fluxes values calculated with the ELA corrections. We measured the leaf net CO₂ assimilation rates (A_{net}) in two different methods. Full chamber (leaves covering all the chamber surface, 6 cm²) and half-filled chamber (leaves covering half of the chamber surface, ~3cm²). For the latter, we used 12 needles for each measurement and later corrected for the actual area using the online version of

the ImageJ software. Needles from 2 trees were sampled (one from each treatment plot) and for each tree, we repeated the measurement 12 times. In all measurements we set the the temperature, PPFD and RH to constant values (Table s2).

3.7 Leaf Water potential (Ψ_w) measurements

Leaf Ψ_w measurements were made once a month at predawn and midday ($\Psi_{w_{pd}}$ and $\Psi_{w_{md}}$) between [months] 2017 and May 2020. Branches were randomly sampled at 6 m height from the north and south sides of four trees per plot, and were used to determine the branch water potentials using a leaf pressure chamber (1505D-EXP; PMS, Albany, USA).

3.8 Stress parameters

Proper quantification of the duration of the different environmental stressors is critical to examine their effect on the resilience and recovery of plants after their removal.

3.8.1 Detection of SWC and VPD stress period

To identify the effect of environmental stressors on the branch-level gas exchange recovery and post-stress activity, we examined separately the effect of soil and atmospheric drought and derived thresholds that described when each one acts as a limiting factor. For soil drought stress, we used the transpirable soil water content (tSWC) limit for the depth profile we measured (0-40 cm), which was determined to be 16.1% (Klein et al., 2014).

To determine the day of VPD stress onset and relief we first set a reference point as the summer VPD average by iterating over the VPD values in the dry period with 60 days moving averages and set the dry period mean value as the highest 60 days average. After setting the dry period mean we iterated again over the VPD values with 11 days window (central day \pm 5 days) to find the last window that is lower than the summer mean by more than 1 standard deviation. The middle day of this window was set as the start of VPD ‘stress relief’. We chose 11 days as the window size to balance between the sensitivity of the detection and the sample size of each window, accounting for missing data points.

3.8.2 Minimal activity period

To understand the stress effect on recovery parameters and peak activity in the subsequent growing season in the different study years, we accounted for the time of the minimal activity period. The

minimal activity period (MAP) was seasonally-based and it was evaluated for each gas exchange variable separately. We estimated the length of the minimal activity period as follows:

$$MAP = DOY_{end} - DOY_{start} \quad (13)$$

Where DOY_{start} is the first day of ‘minimal activity period’ for Anet, E or gb, and DOY_{end} is when the ‘minimal activity period’ ended for each variable. Both points were detected using the stress period detection algorithm (3.8.1).

3.9 Detection of minimal activity period

Average activity of the stress period: Previous methods of season detection (Gonsamo, Chen, & Ooi, 2018) were found unsuitable to our study system. Instead, we created our own season detection algorithm for this purpose. It used daytime means of the variable of interest (i.e. Anet, E, or gb) as an input and produced the ‘starting’ and ‘ending’ days of the minimal activity period. The algorithm consisted of three separate steps. The first step was to identify the mean value of the minimal activity period for each variable and year. The minimal-activity mean value served as a reference to identify the end of that period. To identify the minimal-activity mean value, we iterated over the dry season period (June 1st to November 1st) with a 61-days moving means window with focal day ± 30 days (X). The minimum moving mean was selected and used as the minimal activity value (X_s) and the standard deviation of X_s for the same window was calculated (σ_s).

End day of the stress period: The second step was finding the ‘end of the minimal activity period’, which was also the ‘start of the active season’. To do so, we used a three-day moving mean of X_s (dX_3). dX_3 was calculated starting from the end of minimal activity window (X) forward until the first point satisfying the condition: $|dX_3| > \alpha \cdot \sigma_s$ was found, where α is a parameter that determined how many standard deviations should be dX_3 , depending on the residual (noise level) of the variable’s data set. If more than 1 of 3 daily means in dX_3 were missing, then the averaging interval was extended up to 5 daily means until reaching enough non-missing values.

Spikes detection: The third step was to make sure that the detection of the start/end of the dry season was not attributed to data noise (I.e. spike in the data) during the summer. To do so, we checked for the next 70 days, if $|dX_3| \leq \alpha \cdot \sigma_s$ occurred. If so, we used this point as the starting point

for the detection. If there a rain event occurred within this interval, the corresponding dX_3 was omitted from further analysis.

As the detection was sensitive to the value of α we tried to minimize its value to obtain the most sensitive detection. We checked it first on the least noise data set (Anet) and found that 2 is the lowest possible value. To set the value of α for the other data sets (E and gb), we compared the residuals of the data to a fitted curve using MATLAB and STATISTICA software for each year separately (Fig. s14 and Table s4). The comparison of residuals demonstrated that the gb data set was similar to the Anet data set, and the E residual data set was ~2 times higher than the Anet data set, therefore we used $\alpha=2$ for gb and $\alpha=4$ for E.

3.10 Recovery time and rate

Recovery time (Rt) was defined as the time difference in days between the end of stress to the time of active season start. The end of stress was determined specifically for the different stressors we examined, VPD and SWC, and the season start was determined by the season detection script (methods, 3.8).

$$Rt = Activity\ restoration_{DOY} - Stress\ relief_{DOY} \quad (14)$$

Rr was defined as the average recovery rate at the period between the activity restoration and the beginning of the peak of activity. Rr was calculated as a change in activity based on daytime average, normalized to the activity range of (maximum-minimum), divided by the time difference between the daily values. Rr was calculated separately for each year and variable by the following equation:

$$Rr = \frac{\frac{Y_i - Y_{i-1}}{Y_{min} - Y_{max}}}{X_i - X_{i-1}} \quad (15)$$

where Y is the value of the variable of interest, X is time (days), min and max denote the minimum and maximum value of the variable of interest of a given year, i and i-1 represent a given day average value, and the previous measured day average value respectively. Finally, we get a unitless nominator divided by the number of days so we get the average recovery per day for each variable and year.

Peak activity was calculated based on daytime averages. We defined the peak as the highest 10% (90th percentile) of the data set for each variable and year. We used 10% to make sure we have a large enough data set for all years (20 days or more) and to include the highest number of chambers possible to increase the representatives of the plot without including values that do not represent the peak activity of that season.

3.11 Statistical analysis

Chamber data (E , Anet and gb) were expressed as the average value of all chambers within each plot per hour. For simple pair mean comparisons we used a pair-wise t-test, which was relevant for the comparison of fluxes in the LI-COR 6400 cuvette fully covered with needles vs. fluxes when the cuvette was only 50% covered with needles (4.1.5). For multiple comparisons of means, we used the Tukey HSD test or simple ranking of the sampled data in case the data did not meet the model assumptions, the latter of which was relevant for the comparison of fluxes using different leaf areas in the branch chamber (4.1.3). For analyses that included the different years component of the chamber's data (i.e., peak activity of different years, 4.3.4) we used repeated measures comparisons since we used the same test groups several times.

All statistical comparisons and models were checked at a significance level of 95% (p-value <0.05). All models used for mean comparison were tested for the basic assumptions of ANOVA: variances equality (Levene test) and normality of residual distribution (Shapiro-Wilk test). When one of the two assumptions was not met we performed standard mathematical transformations on the data. All statistical analyses were performed in JMP 15 (JMP, SAS, Statistical discovery software)

For the detection of changes in data over a time series as in the case of the season detection (methods 3.8) or the VPD stress detection (methods 3.71), we used a change detection method. In this study, we used a reference setpoint defined by the minimum or maximum average value from which we want to find the change. After setting the reference point we iterated over the data set of interest in a moving average window of varying size according to the data set and desirable detection resolution. We compared the windows average to see if it was different from the summer average $\pm X$ standard deviation by t-test, where X was a changing number according to the data set noise and desirable detection resolution.

4. Results

4.1 Effective leaf area

4.1.1 Light attenuation by leaf self-shading

We studied the effects of mutual shading in the branch chambers associated with the use of several twigs in their native, complex structure. The results reported in Fig. 3 indicated that the chamber materials reduce the light intensity in the chamber to $79.6 \pm 7.4\%$ of the ambient level (i.e., light attenuation of 20.4%). When leaves are inserted, most of the light is absorbed by the first twig (leaf area= $0.023 \pm 0.002 \text{ m}^2$), with PPFD decreasing by $\sim 62\%$ relative to ambient PPFD. Insertion of one additional twig did not change significantly the light attenuation. Additional light attenuation was observed with the insertion of the third and fourth twigs by $\sim 10\%$ for each twig (Fig.3).

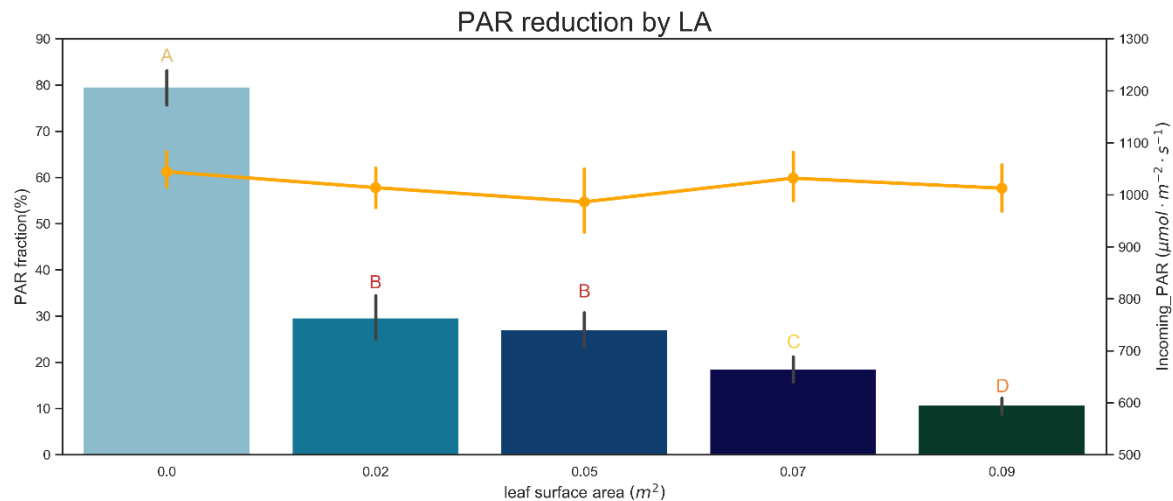


Figure 3. PPFD attenuation by leaf area: Changes in the PPFD fraction (PPFD; ratio of measurements above and below the branch chamber) for different number of twigs, increasing leaf area in the chamber. Incoming PPFD during the experiment is indicated by the yellow line during a one day campaign in December 2020. Values are the average \pm SD; ($n=6$). Different letters indicate significant differences at the $p < 0.05$ level.

4.1.2 Image-based leaf area correction

To account for the light attenuation due to mutual shading (showed in Fig.3) we assessed possible correction approaches to obtain the effective leaf area enclosed in the branch chambers. The first

approach, described in Fig.4, was to correct all three leaf area calculation methods (see Table.1 1-3) to the directly lit leaf area using image analysis. The relationships between the Image-projected leaf area (IPLA) and the measured leaf area depended on the way the leaf area was determined (TLSA, projected, 1D or 2D; see Table.1, lines 1-3). In all cases, the ratio between the IPLA and the measured leaf area (Y axis) linearly correlated with the respective leaf area (R^2 of 0.98; Fig. 4 a-c), indicating that the image-based estimate was robustly related to the actual leaf area. This was true also across the treatment plots, as indicated by the two higher and the two lower points in the plots representing chambers of the irrigated and control plots, respectively, following the same linear relationships. In Fig. 4, panel C, the ratio (Y axis) values of the control plot are lower than 1, ratio values lower than 1 means that the shaded area is larger than the actual leaf. Due to the above, we rejected the 1D leaf area as a possible basis for the correction. The 2D leaf area and TLSA (Fig. 4 panel a and b) resulted in the same final effective leaf area. Since the TLSA method does not take into account the geometry of the needles and therefore, the fact that part of the needle surface is permanently not lit, the values obtained from calculating the fluxes using this method are unrealistically low (Fig. s11), and thus was also excluded from further use. This left the method of 2D leaf area (Fig.4b) as the most robust LA calculation method to use as an input for the image based leaf area correction.

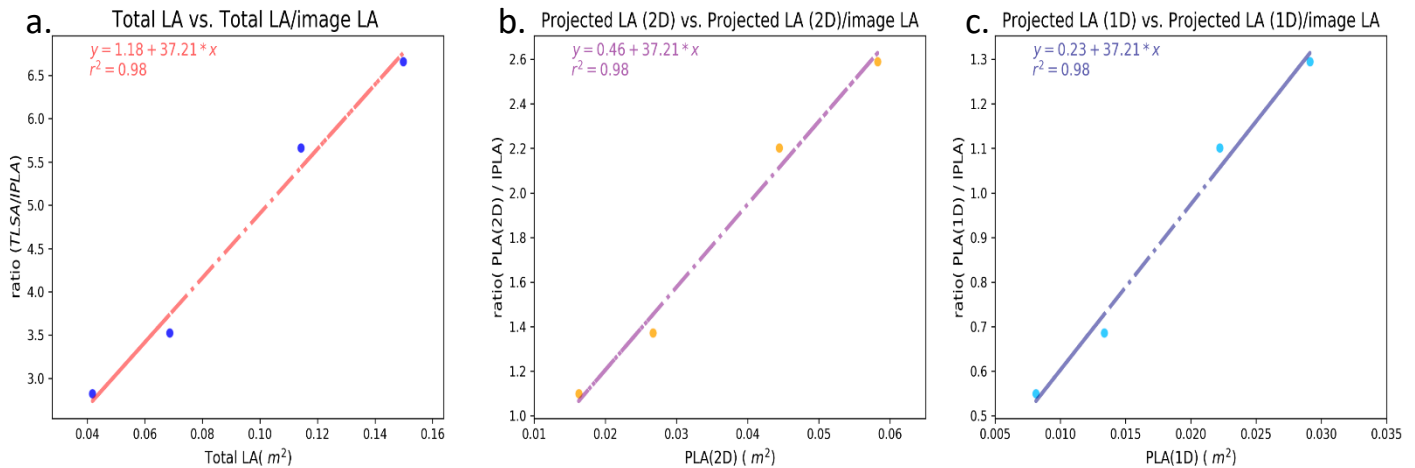


Figure 4. Image Based Leaf Area correction: a) Correlation between Total Leaf Area (TLA) and the ratio between TLA and Image Projected LA (IPLA). b) Correlation between projected LA (2D) and the ratio between Projected LA (2D) and IPLA. c) Correlation between projected LA (1D) and IPLA. Each point in all panels is the average of all images for a given measured leaf area ($n=3$). For all panels, the two higher points are of twigs from the irrigated plot and the two lower points are of twigs from the control plot.

4.1.3 Flux-based leaf area correction

Results of the flux-based estimates of light attenuation in the branch chambers are shown in Fig. 5. The leaf-level gas exchange showed different response patterns to change in LA when the chamber was sun-exposed or shaded. When shaded, flux rates were low and did not respond significantly to the changes in LA. In the sun-exposed chambers, rates were higher and decreased with increasing LA. Anet dropped from $1.14 \pm 0.43 \mu\text{mol m}^{-2} \text{s}^{-1}$ at $\text{LA} = 0.02 \pm 0.01 \text{ m}^2$ ($n=6$) to $0.81 \pm 0.33 \mu\text{mol m}^{-2} \text{s}^{-1}$ at $\text{LA} = 0.08 \pm 0.01 \text{ m}^2$ ($n=6$), leading to a ratio of 1.75 between flux value with lowest and highest LA (Fig. 5 a). Similarly, E decreased from $0.47 \pm 0.29 \text{ mmol m}^{-2} \text{s}^{-1}$ at $\text{LA} = 0.02 \pm 0.01 \text{ m}^2$ ($n=4$) to $0.26 \pm 0.03 \text{ mmol m}^{-2} \text{s}^{-1}$ at $\text{LA} = 0.08 \pm 0.01 \text{ m}^2$ ($n=4$), leading to a ratio of 1.6 (Fig. 5b). The ELA_f was calculated separately for Anet and E based on their specific ratio between flux rates at the lowest to rates at the highest leaf area inside the chamber. The ratios obtained from the experiment were used to correct the leaf area proportionally to the decrease in fluxes due to mutual shading, and thus TLSA for Anet calculation was multiplied by 0.25 and for E calculation by 0.4. Note that this approach assumes constant correction factors (see Discussion).

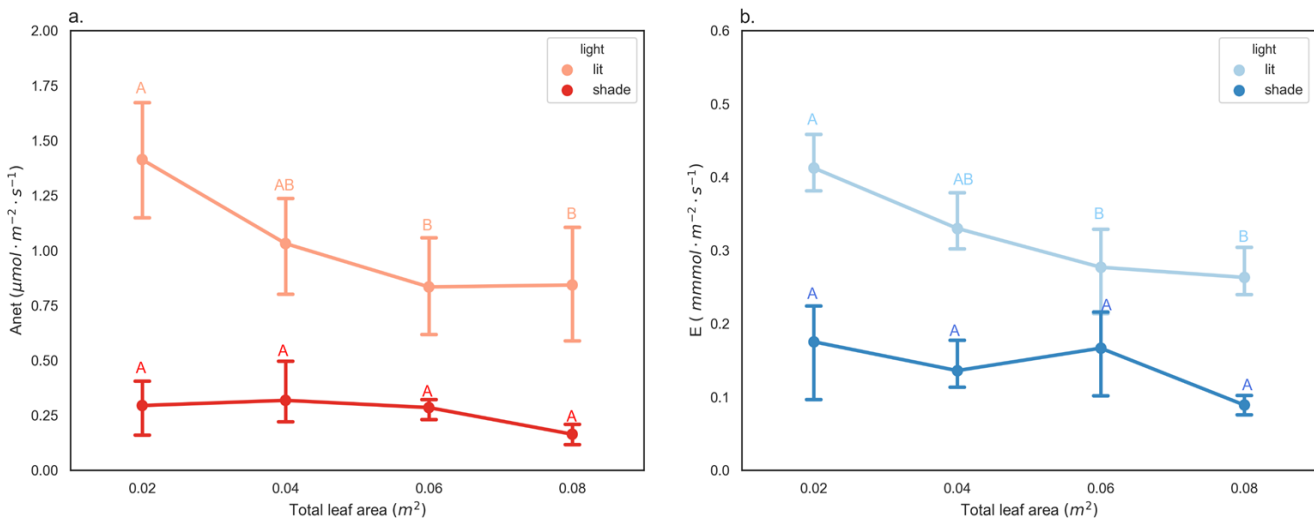


Figure 5. Flux based leaf area correction: a) Average Anet vs binned leaf area (LA) for lit (orange points) and shaded (red points) chambers. b) Average E vs. binned leaf area (LA) for lit (light blue points) and shaded (blue points) chambers. Presented are averages for all dates of measurements, which included values from chambers 5, 2, 3 and 6 (irrigated plot). Different letters indicate statistical difference between LA classes separately for each variable (Anet and E) and sample group (lit and shade), (Tukey HSD test, $p < 0.05$).

4.1.4 Comparison of WUE of the two correction method

To check the robustness of our effective leaf area corrections, we checked the relationships between the rates of carbon assimilation, A_{net} , and evapotranspiration, E , obtained after applying the two corrections. The slopes of these relationships (3.16 and 3.54 for ELAp and ELAf, respectively; Fig. 6), representing instantaneous branch water use efficiency (WUE). The WUE values of the two correction methods were compared with published WUE values, and showed good agreement at similar environmental conditions of high SWC and low VPD (~ 3.3 ; (Grünzweig et al., 2003)).

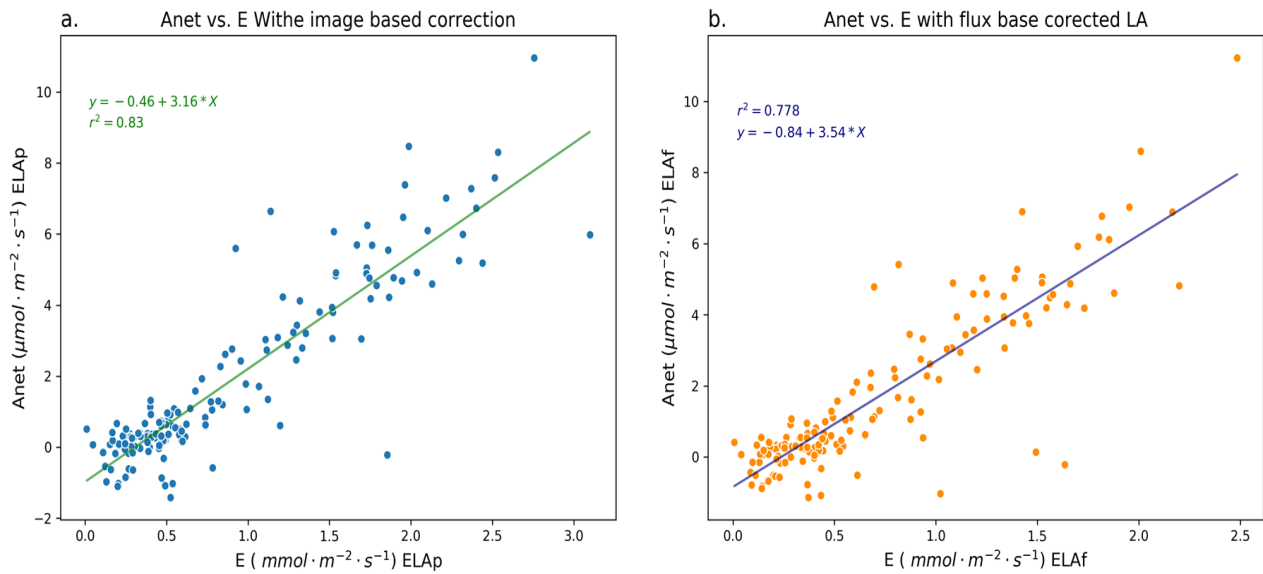


Figure 6. linear correlation between A_{net} and E (WUE). a) Image Based Leaf Area (IBLA) correction and b) Flux Base Leaf Area (FBLA) correction along the PPFD range from 0-1750 $\mu\text{mol} \cdot \text{m}^{-2} \cdot \text{s}^{-1}$. Data includes all values used to create the light response curves for A_{net} and E (Fig.s11).

4.1.5 Leaf chamber gas exchange

In order to use the Li-cor 6400 as a benchmark for comparison with the values obtained from the branch chambers, we first compared two measurement methods that are routinely used with the Li-cor 6400 cuvette. The first approach uses a fully covered cuvette (20-26 needles covering the chamber area of 6 cm^2), and the second, use a half-covered cuvette (12 needles covering $\sim 3 \text{ cm}^2$). Leaf area-based rates of A_{net} were higher by 28.5% for the irrigated plot and by 31.5% for the control plot when using the half-covered as compared to the fully covered cuvette (Fig. 7). The

average difference of both plots was 30%, and this value was used henceforth when rates from the two approaches were compared. The relatively large difference in the rates obtained by the two approaches is likely due to increased light reflectance from the bright chamber wall onto the lower side of the leaves in the half-covered cuvette. The significant difference of 30% between the measurement methods indicated an artifact created by the measurement method of a half-full cuvette. As noted in Methods 3.6.4, the Li-cor 6400 was the benchmark to which we compare the flux values obtained from the branch chambers, therefore we used only the corrected values of the Li-cor 6400 for further comparisons. Note that the environmental conditions maintained constant within the leaf cuvette throughout the campaign (Table s3).

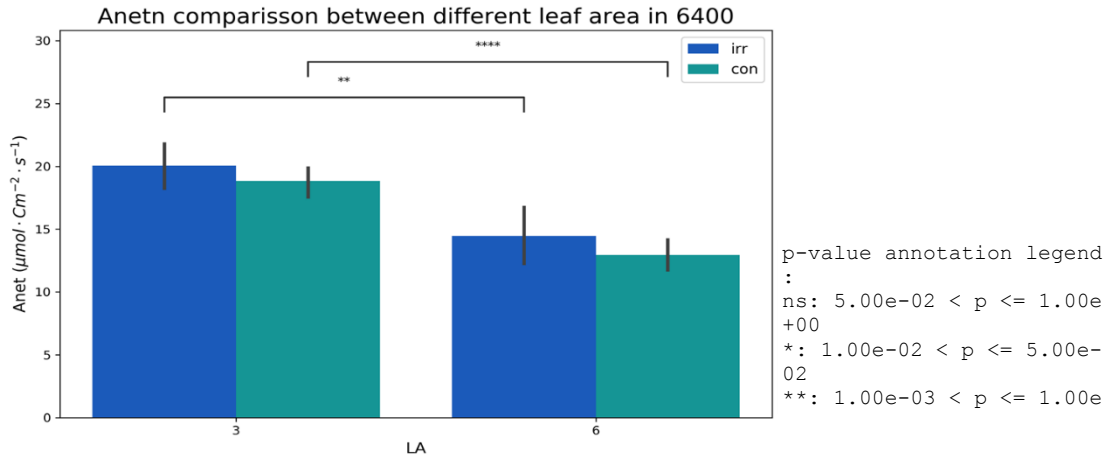


Figure 7. LI-COR 6400 comparison of Anet between full to half full chamber: in the X axis is the two different categories of 3 cm² (half chamber) and 6 cm² (full chamber), in the Y axis is the Anet rate measured for each plot (control in green and irrigation in blue) and category. Values are from one day campaign in January 2021 and from 2 trees, one from each plot. Each value is average \pm stdv of all measurement for a given tree and category (n=6). Asterisks indicate significant differences between different categories (t-test for independent pairs, P-values annotation is given in the low right corner of the figure).

4.1.6 Validation of the leaf area correction methods

In order to assess whether the leaf area correction methods (ELA_p and ELA_f) resulted in comparable flux values with our benchmark, the Li-cor 6400, we compared the values obtained by the two methods at times when the environmental conditions were comparable (see environmental condition comparison in Table s2). Mean Anet obtained using either LA correction was not significantly different from the corrected Li-cor 6400 values, irrespective of measurement months and plot (Fig.8 a, c and e). E rates obtained using either correction were significantly lower than those of the Li-cor 6400 for both plots in September, but not in October (Fig.8 b, d, and f). When comparing the values of the two LA correction methods, ELA_p and ELA_f , no significant difference was observed for Anet and E in the control and irrigated plots. Despite the similarity of Anet and E obtained by the two correction methods, it is evident that the values based on the ELA_p correction were slightly higher than those based on ELA_f , with a difference of 9.6% for Anet and 20.0% for E (Fig. s16). In addition, the ELA_p correction is based on the measured leaf area, as opposed to ELA_f that was based on a constant correction factor. Considering these results, we subsequently used the ELA_p values in all further flux calculations.

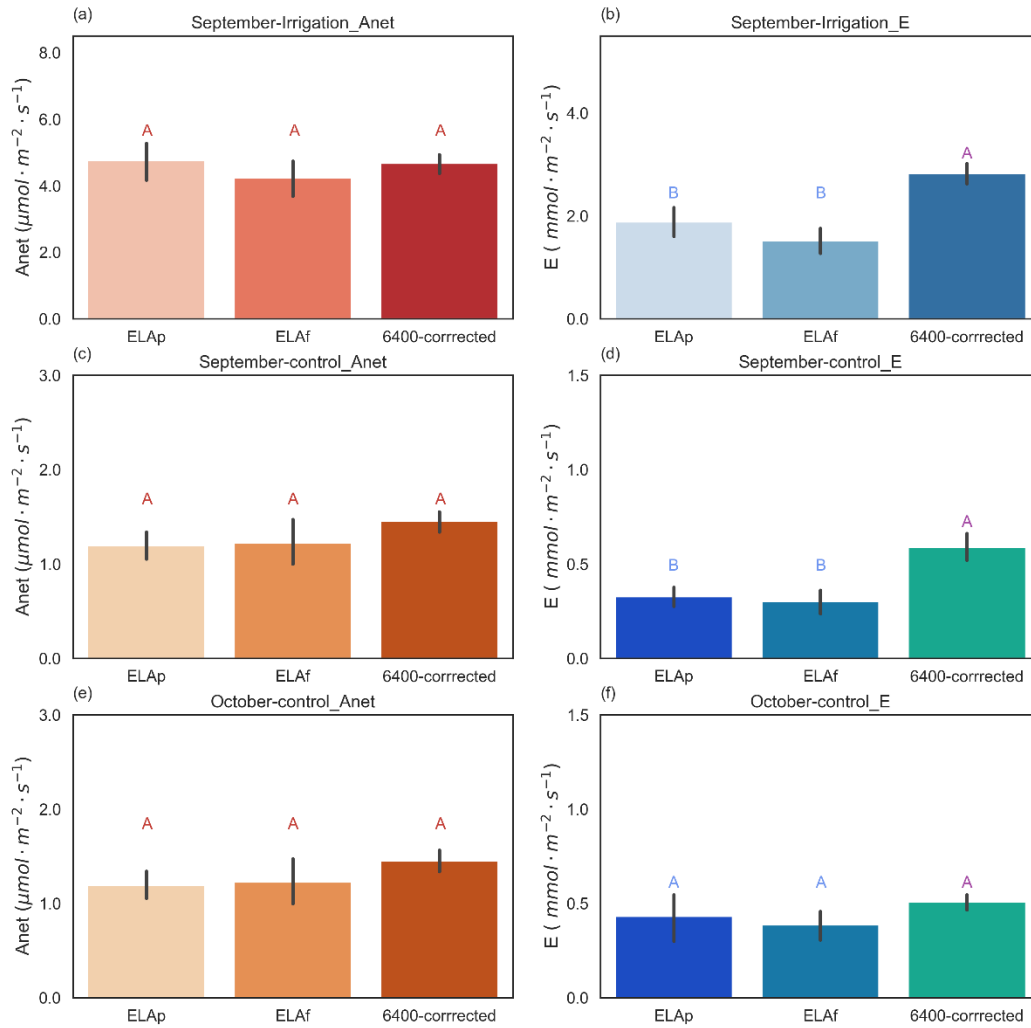


Figure 8. Flux values comparison between methods. Photosynthesis (A_{net}) and Transpiration (E) calculated with ELA_p (IBLA_2D correction) and ELA_f (FBLA correction) compared with LI-COR 6400 values. Comparison was done for both the irrigated (Fig.8 (a) and (b)) and the control plot (Fig.8 (c), (d), (e) and (f)) for September (Fig.8 (a), (b), (c) and (d)) and October (Fig.8 (e) and (f)). The values from the branch chambers were filtered to fit the range of temperature and VPD of the LI-COR 6400 measurement campaign of the same month. For each subplot, different letters indicate statistical difference between sample groups (LSMeans Differences Tukey HSD test, $p < 0.05$).

4. 2 Stress period and environmental conditions

To quantify the stress period we used the length of the minimal activity period (MAP) based on the time difference between the day of stress start and the day of relief (see methods, eq.13). This parameter is based on the activity level of the different LGE variables during the ‘low activity period’ of the four years of measurements. In this section, we report the environmental conditions (SWC and VPD) during the four years and their relations with the MAP length.

MAP varied between LGE variables and between years, and thus it is annual and variable-specific (Fig. 9). MAP was quite similar for Anet and gb during the three years of available data, with a difference in MAP between the two variables averaging 5%. MAP was the longest in 2019 (46% of the entire year) and the shortest in 2017 (Fig. 9a and b).

MAP of E showed a different pattern from those of Anet and gb. For E 2019 was also the year with the longest MAP, but it lasted for 68.5% of the days of the year. MAP of E was the shortest in 2020 rather than in 2017 as for Anet and gb MAP (Fig. 9c). For all three years, MAP of E was longer than MAP of Anet and gb, and the most prominent difference was observed in 2017 when the MAP of E was 68% higher than the average MAP of Anet and gb.

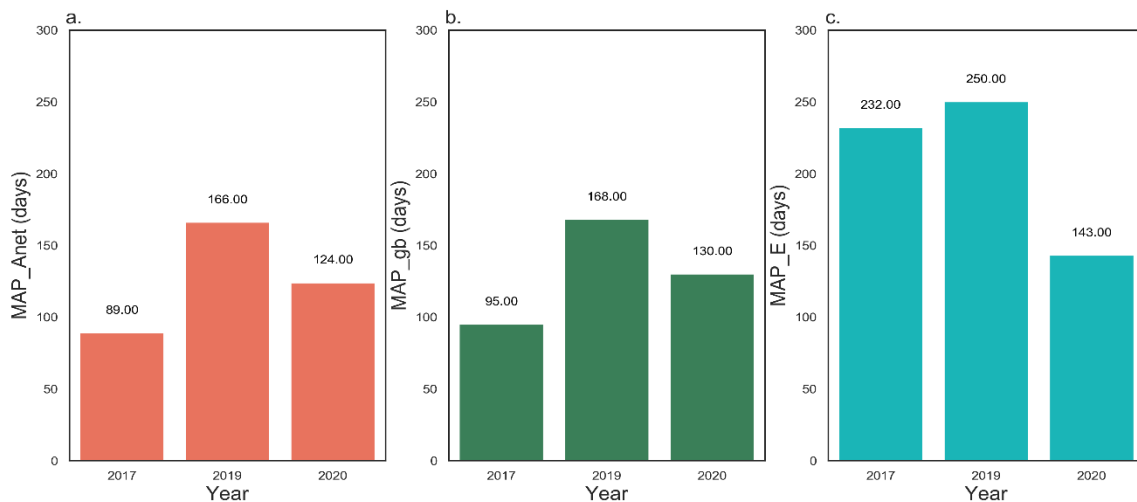


Figure 9. minimal activity period (MAP) of: a) photosynthesis (Anet) in yellow, b) bleu Branch conductance (gb) in green and c) Transpiration (E) in for three years of the experiment. Values of minimal activity period are based on the season start and end date from the season detection script. 2018 data is not shown due to lack of VPD data at the recovery time period.

After obtaining the MAP of the different LGE variables we examined its relationships with the annual cycle of SWC and VPD (Fig.10 a and b). Four years of measurements of volumetric soil water content (SWC) in native conditions (control plot) showed a typical pattern for the Yatir forest, with a peak of high SWC in the wet season, reaching up to ~33%, and a long dry season with low SWC in summer, decreasing to ~11% (Fig. 10b). In all four years, SWC decreased in late spring when the amount of rain decreased simultaneously with an increase in VPD (Fig. 10b and a). SWC increased in late autumn/early winter with the renewal of rains and the decrease in VPD. The winters of 2017-2019 were relatively dry, with 247, 168, and 224 mm, respectively, compared with the long-term average of $279 \pm 90 \text{ yr}^{-1}$. However, the 2019-20 winter was a rare wet one, with annual precipitation of 416 mm. Consequently, the duration of 'dry season' ($\text{SWC} < t\text{SWC}$) ranged from 218 days in 2020 to 242 and 261 in 2017 and 2018 respectively, and 298 in 2019 (Fig. 10b).

The correlation of the MAP with the dry season length varied between the different LGE variables. We can see that MAP of Anet and gb was shorter than the dry season length (the period that the SWC is below the black line for each year; Fig. 10b) as calculated from SWC values for all three years, and the difference between the two was the largest in 2017 reaching 151 days. The MAP of E however was well correlated with the dry season length for 2017 and 2019, with a total difference of 11 and 8 days respectively. In 2020, the difference was larger with a total of 65 days which was attributed solely to the gap at the start of the dry season (Fig.10b).

The VPD record for the study period showed a similar but opposite trend to that of SWC. VPD was low in winter, with minimum values in January ($1.8 \pm 0.07 \text{ kPa}$), and reached its peak in summer in July ($4.2 \pm 0.23 \text{ kPa}$) (Fig. 10a). In summer, maximum VPD might reach extreme values of ~12 kPa. The number of days with summer maximal VPD level (see methods 3.7.1; black vertical lines in Fig 10a) ranged between 119 days in 2017 and 171 days in both 2019 and 2020.

Similar to the case of SWC, the correlation of the MAP to the maximal VPD period varied between the different variables of the LGE. MAP of E was not correlated with the maximal VPD period. In 2017 and 2019, MAP was longer by 115 and 79 days, respectively, than MAP of E, and in 2020, MAP of E was shorter by 28 days and showed only a partial temporal overlap. In contrast to E, MAP of Anet and gb were better correlated with the maximal VPD period in 2017 and 2019, with total differences of 24 and 15 days, respectively. MAP of Anet and gb in 2020 showed a greater

difference and was shorter by 57 days but was within the time of the maximal VPD period. For all three years, the difference between the MAP of Anet and that of gb was attributed mostly to the gap at the start of the maximal VPD period (Fig.10a). In addition, in all years with available dry season length and maximal VPD period, the dry season was longer. MAP of Anet and gb appeared to be shorter than that of E and had better temporal overlap with maximal VPD period rather than with the dry season length. On the contrary, the MAP of E showed a higher temporal correlation with the dry season length (Fig. 10a and b).

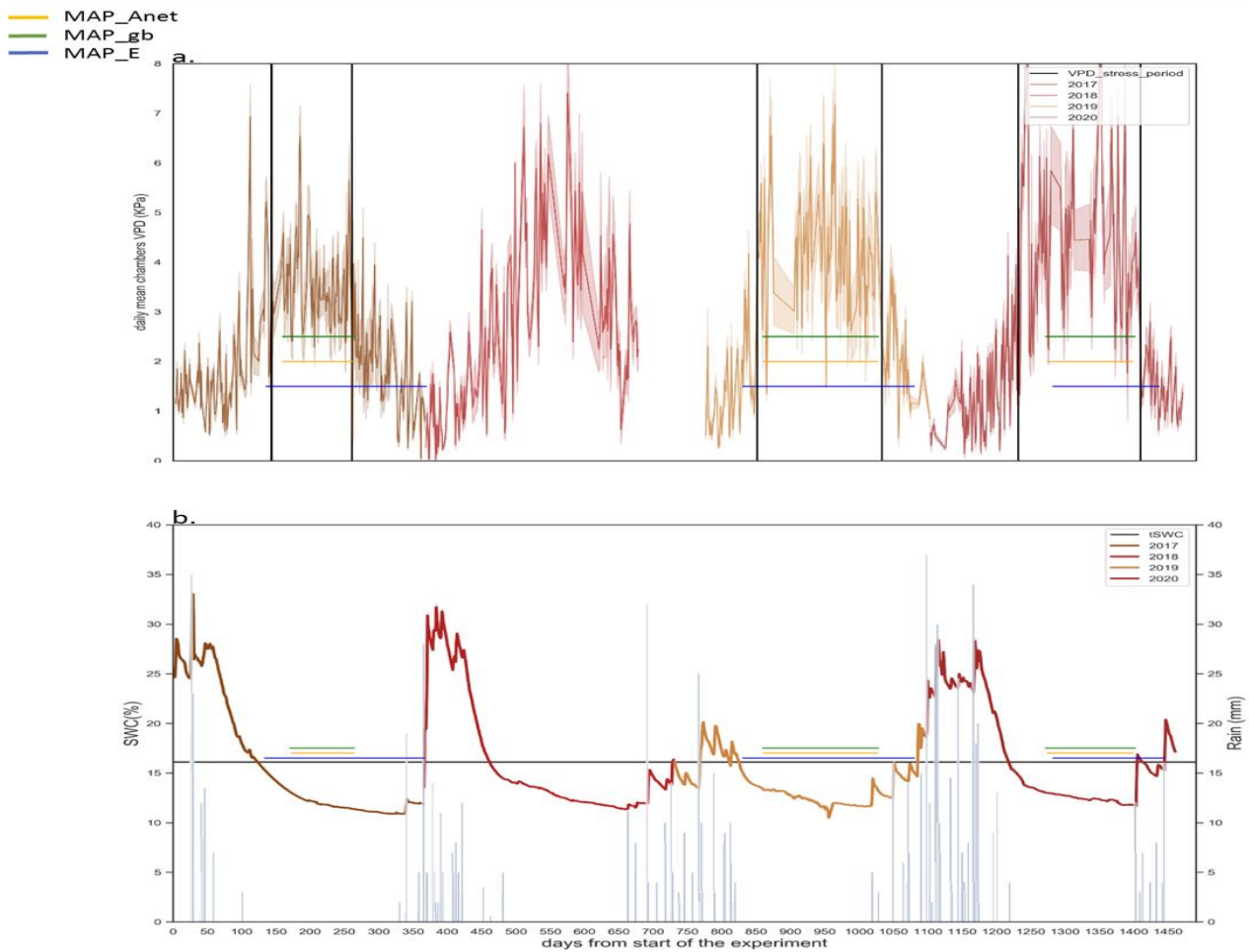


Figure 10. Seasonal cycle of: a) average day-time Vapor Pressure Deficit (VPD; kPa) during the study period and b) Daily average soil water content (SWC; %). For subplot a, black vertical lines represent the VPD stress period start and end for each year. 2018 data are not shown due to lack of data at the recovery time period. For subplot b, black horizontal line represent the transpirable soil water content (tSWC) limit. For both subplots the change in the color of the line represents the change of years, the horizontal green, orange and blue lines represent the minimum activity period length of gb, Anet and E respectively.

The interannual variability of rainfall timing and distribution might significantly affect both the SWC level during the wet season and its length. Two years of rain distribution, SWC, and PET measurements were used to demonstrate this effect. In Fig.11 we compare two years with similar total annual precipitation (24 mm difference) and similar monthly average PET. The first year (2016-17; Fig.11 a) with a long wet season (when SWC > tSWC), and the second year (2018-19; Fig.11 b) with a short wet season. The main differences between the two years were the timing of rainfall, the number of rainy months, and the size of the average rain events in those months. While in 2016-17 rainfall events were mainly concentrated in three months with large rainfall events, in 2018-19 however, rainfall events were spread over five months with smaller rainfall events. In addition, most of the rain in 2016-17 precipitated in the months with the lowest PET (December-February) while in 2018-19 a significant portion of the rain precipitated in the months with relatively high PET (October, November, and March). Those differences resulted in a longer wet season and higher SWC level in 2016-17, despite the similar annual P, 2016-17 wet season was 56 days longer, and the average SWC of the wettest month was 12% higher comparing to 2018-19.

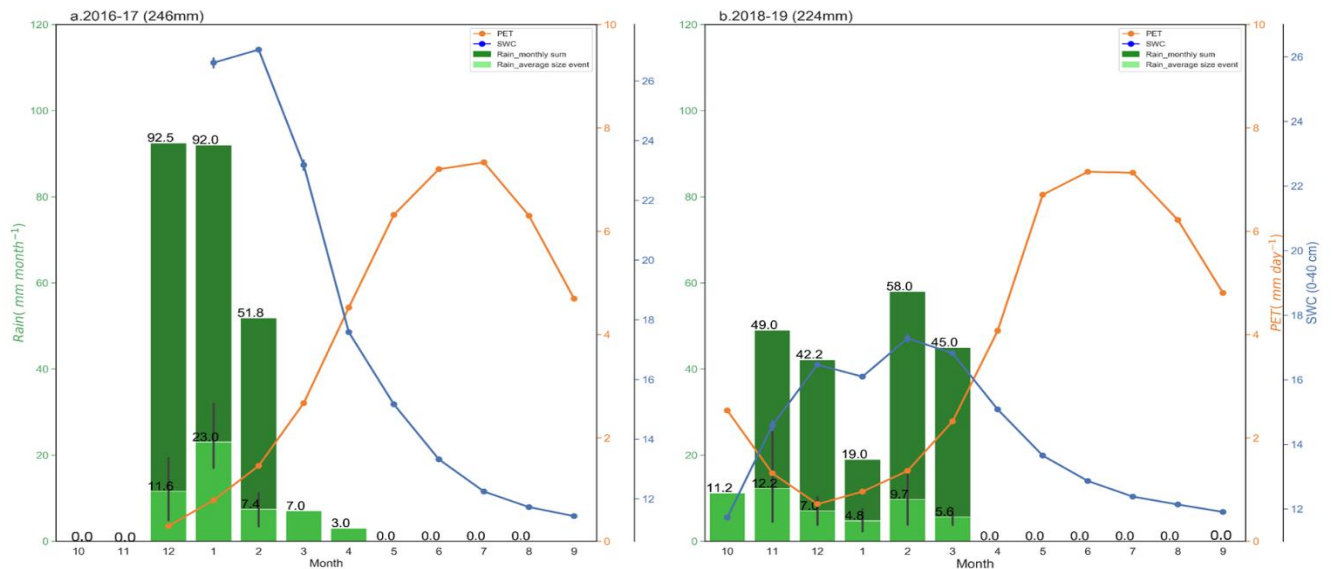


Figure 11. Monthly dynamics of rain (green), potential evapotranspiration (PET in orange) and soil water content (SWC in blue) of: a) 2016-17 winter until 2017 summer and b) 2018-19 winter until 2019 summer. Dark green bars represent the monthly sum of rains and light green bars represent the average rain event size \pm stdev per month, note that months with only a light green bar represent a month with single rain event. Orange points represent the average potential evapotranspiration (PET) for each month based on daily averages from Yatir fluxnet station. Blue points represent the monthly average soil water content (SWC) of the upper 40cm for the two periods based on daily averages \pm stdev per month. Note that in 2016-17 PET record started in December 2016 and SWC record started in January

4.3 Recovery parameters, peak activity and WUE

4.3.1 Leaf gas exchange recovery time and rate

The annual patterns of Anet, E, and gb were consistent with the patterns of the environmental conditions across the study period (compare results in Fig. 12 with Fig. 10a and b). Branch gas exchange peaked in late winter to early spring, and decreased when SWC decreased and VPD increased in the late spring and remained low up to the point of recovery in the late autumn to early winter (Fig. 12).

The relationship between the seasonality of the stress factors (SWC, VPD) and LGE components was reflected in the '*recovery time*' (Rt, see Methods 3.10), the time between relief of the environmental stressor and the restoration of plant activity. Comparison between the Rt of the different variables shows that the average Rt for E was the shortest and the most uniform between the different years, ranging between 0-2 days (Fig. 12c). Anet and gb recovery times (Rt) were quite similar to each other when Rt of gb was one or two days longer than Rt of Anet. The average Rt of Anet and gb was longer and less uniform compared to Rt of E, ranging from 1 to 11 days (Fig. 12a and b)

Another essential difference in recovery time between the variables is the timing at which it occurs. While Anet and gb recovered in early autumn, on average on DOY 286 ± 25 , E recovered only in the beginning of the winter, on average on DOY 360 ± 13 (Fig 12). The significant difference of 74 days on average can be attributed to the differential response of the various variables to the removal of the stressors. While Anet and gb recovery were closely linked to the VPD stress removal in early autumn (Fig. 12a, b), the timing of E recovery is strongly linked to the SWC stress removal, which occurs later, namely in the early winter (Fig. 12c). The time difference between Anet and E recovery resulted in high WUE during the recovery period.

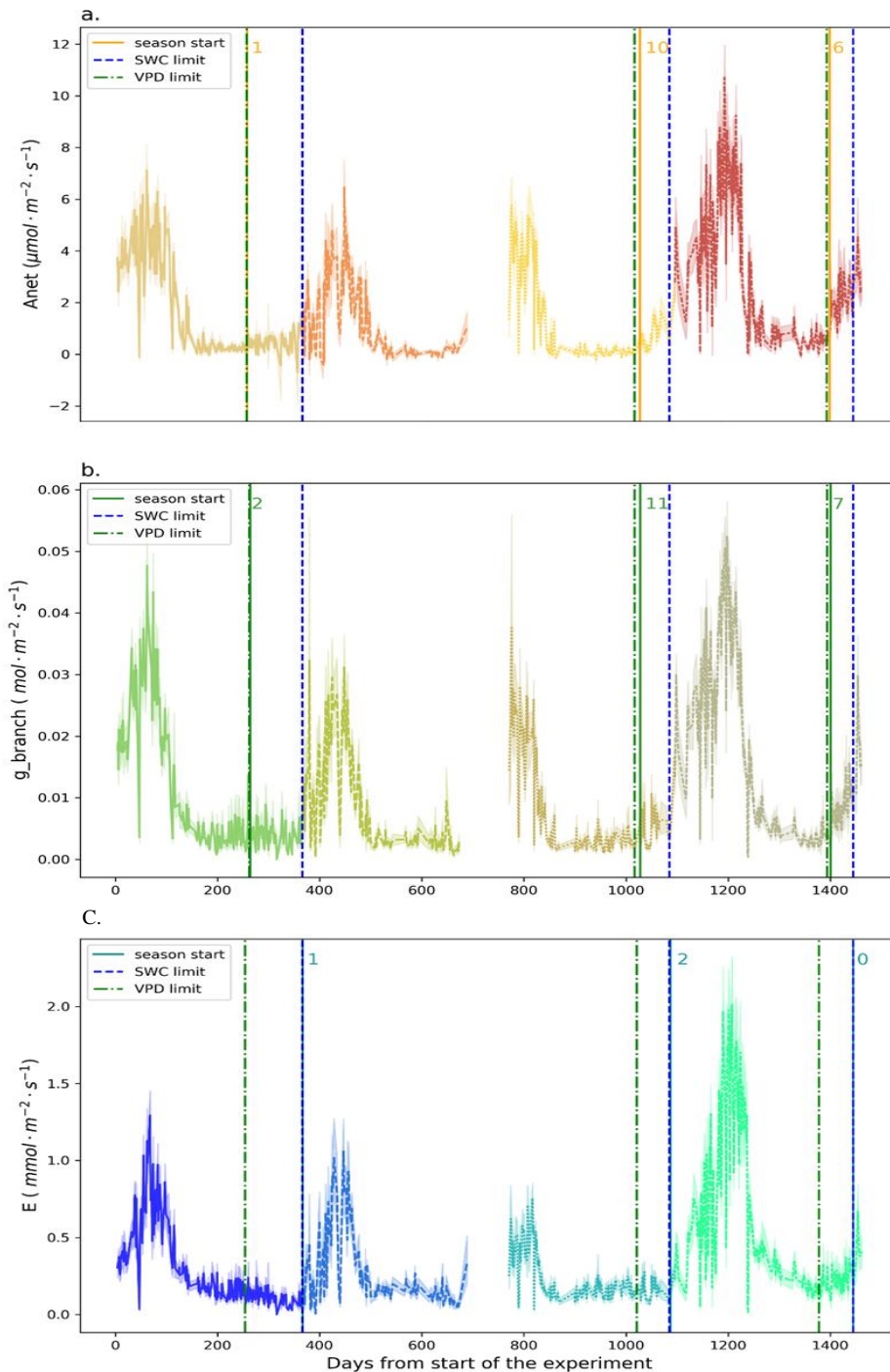


Figure 12. Seasonal cycle and recovery time of leaf gas exchange (LGE): a) Rate of net photosynthetic CO_2 assimilation (A_{net}), b) Branch conductance to water vapor (g_b) and c) Rate of evapotranspiration (E) for the study period. For each panel, each color indicates an annual cycle. Full lines of different colors represent the start of the active season, the number next to each line denotes the time from stress removal to the start of the active season for the respective variable. Dashed blue lines show the day that average soil water content (SWC) was higher than the transpirable soil water content threshold (tSWC). Green dashed and dotted lines show the day that day-time average VPD was lower than the mean summer VPD for the last time. For all LGE variables, day-time average values are presented. 2018-19 recovery time is not presented due to lack of data.

4.3.2 Yearly trend of WUE

The annual pattern of instantaneous WUE (Anet/E; Fig. 13), shows that WUE was affected by the annual cycle of environmental stressors. WUE was high when SWC was high and VPD was low in the winter until the early spring (January to April). With the dehydration of the soil and increase in VPD in the late spring, and throughout summer (between May and September), WUE remains constant and at low values. When VPD dropped along with the first rains in the early autumn (October to December), Anet recovery begins ahead of the increase of E which started to recover only when the SWC exceeds the tSWC limit (Fig. 12), this results in an upward trend of WUE at the recovery period (October to December), reaching its maximum in December-January.

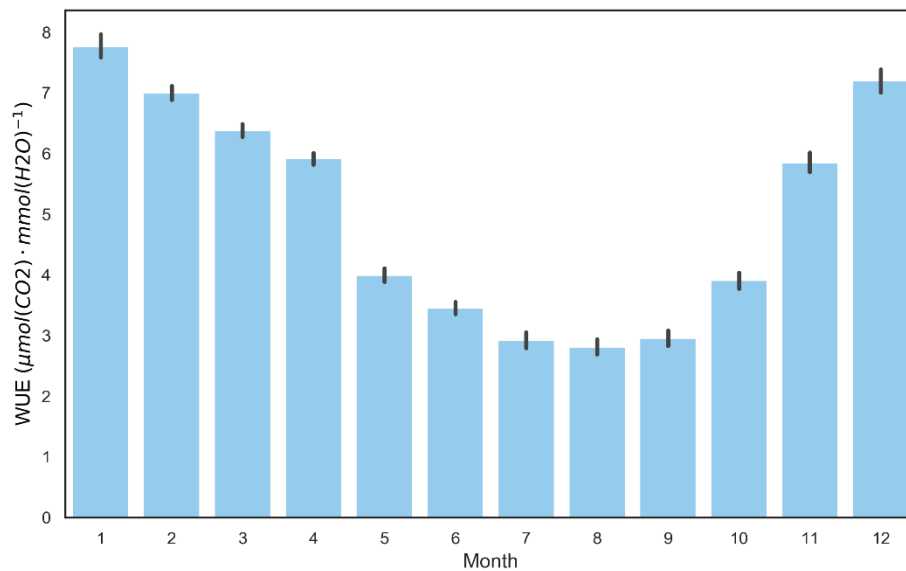


Figure 13. Monthly average (\pm STDEV) of water use efficiency (WUE) for the four years of the study period (2017-2020). Values of WUE were calculated based on day time averages of Anet, E and gb.

4.3.3 Leaf gas exchange Recovery rate

The ‘recovery rate’, Rr, was defined as the average rate of change per day in the period between the start of the active season until the start of the peak activity period (see Methods 3.9) and was determined for each LGE variable separately (only for 2018 and 2020 for which both the start of the active season and start of peak activity period). For both Anet and gb, Rr was higher in 2019-20 than in 2017-18 by a factor of ~2 (Fig. 14a and b). No such difference in Rr was observed for E (Fig.14c). For the two recovery periods that were examined, the average Rr for E was markedly higher by 70% and 97% than Rr of Anet and gb, respectively.

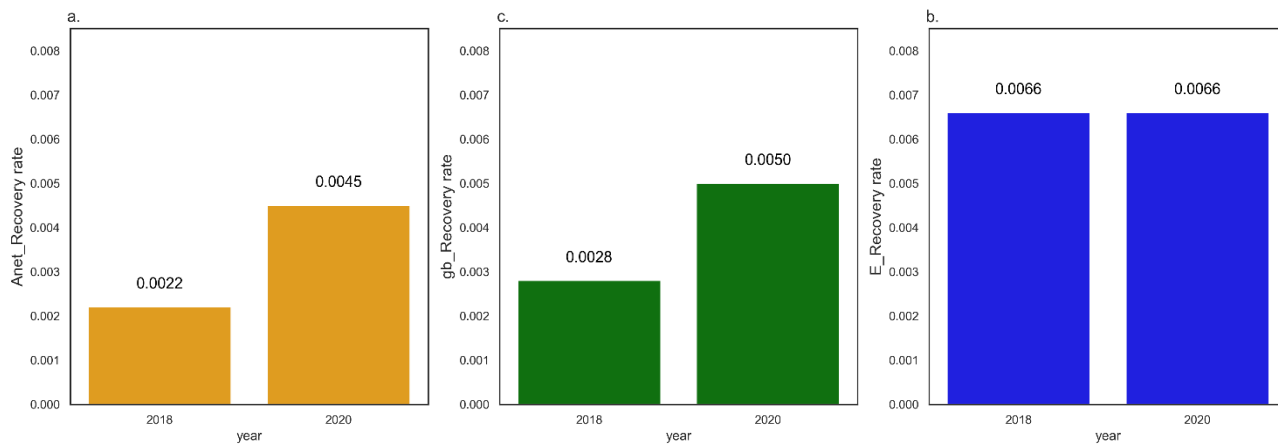


Figure 14. Recovery rate (Rr) of: a) Photosynthesis (Anet), b) Transpiration (E) and c) Branch conductance (gb). Rr values are based on day-time averages for each variable from the season “start” to the “peak activity start”. Number above each bar represents the value of Rr for a given year and variable. 2017 Rr is not shown since we started the measurement after the recovery period of 2016-17 and 2019-20 Rr is not shown due to lack of data at the recovery period.

4.3.4 Leaf gas exchange peak activity and its duration

The results reported above showed that the interannual variability in the environmental conditions results in interannual variations in the temporal patterns of LGE. Beyond the temporal aspects, this is associated also with variations in the average of peak activity rates (top 10% of the daily rates of different LGE variables during one year; Pr) and the duration of the peak activity (the difference between the first day and the last day of the peak activity period (Pt); Fig. 15a, b, and c). Examining the peak activities of the different years showed that for Anet, the 2017 Pr and Pt ($5.2 \pm 0.65 \mu\text{mol m}^{-2} \text{s}^{-1}$, 92 days, respectively) were greater than those of 2018 ($4.0 \pm 0.7 \mu\text{mol m}^{-2} \text{s}^{-1}$, 54 days) and 2019 ($4.6 \pm 0.5 \mu\text{mol m}^{-2} \text{s}^{-1}$, missing Pt). Pr for Anet in 2020 was significantly higher than in the other years, but the Pt period was not longer ($8.0 \pm 0.8 \mu\text{mol m}^{-2} \text{s}^{-1}$, 70 days) (Fig. 15 a and d).

Interannual variation in gb was similar to that of Anet, with the 2017 values of Pr and Pt being higher ($0.03 \pm 0.004 \text{ mol m}^{-2} \text{s}^{-1}$, 62 days) than those of 2018 ($0.02 \pm 0.003 \text{ mol m}^{-2} \text{s}^{-1}$, 43 days), and 2019 ($0.02 \pm 0.004 \text{ mol m}^{-2} \text{s}^{-1}$, missing Pt). In 2020, the Pr of gb was significantly higher and Pt was longer than in the other years ($0.04 \pm 0.005 \text{ mol m}^{-2} \text{s}^{-1}$, 60 days) (Fig. 15 b and e).

The interannual variation in the seasonal Pr and Pt for E was different compared with Pr and Pt of Anet and gb. Both Pr and Pt of E were relatively similar in 2017 and 2018 ($0.82 \pm 0.14 \text{ mmol m}^{-2} \text{s}^{-1}$, 62 days, and $0.82 \pm 0.11 \text{ mmol m}^{-2} \text{s}^{-1}$, 52 days, respectively), which were higher, for Pr, than in

2019 ($0.54 \pm 0.08 \text{ mmol m}^{-2}\text{s}^{-1}$, missing Pt). In 2020, Pr of E was considerably higher than in the other years but Pt was shorter ($1.7 \pm 0.16 \text{ mmol m}^{-2}\text{s}^{-1}$, 47 days) (Fig.15 c and f).

The peak of activity of all LGE variables in the years 2017-2019 occurred at a similar time between the end of January and the end of March (DOY 30-90), while in 2020, the peak of activity was shifted to between the end of March and the beginning of May(DOY 90-130) (Fig.15 a, b and c).

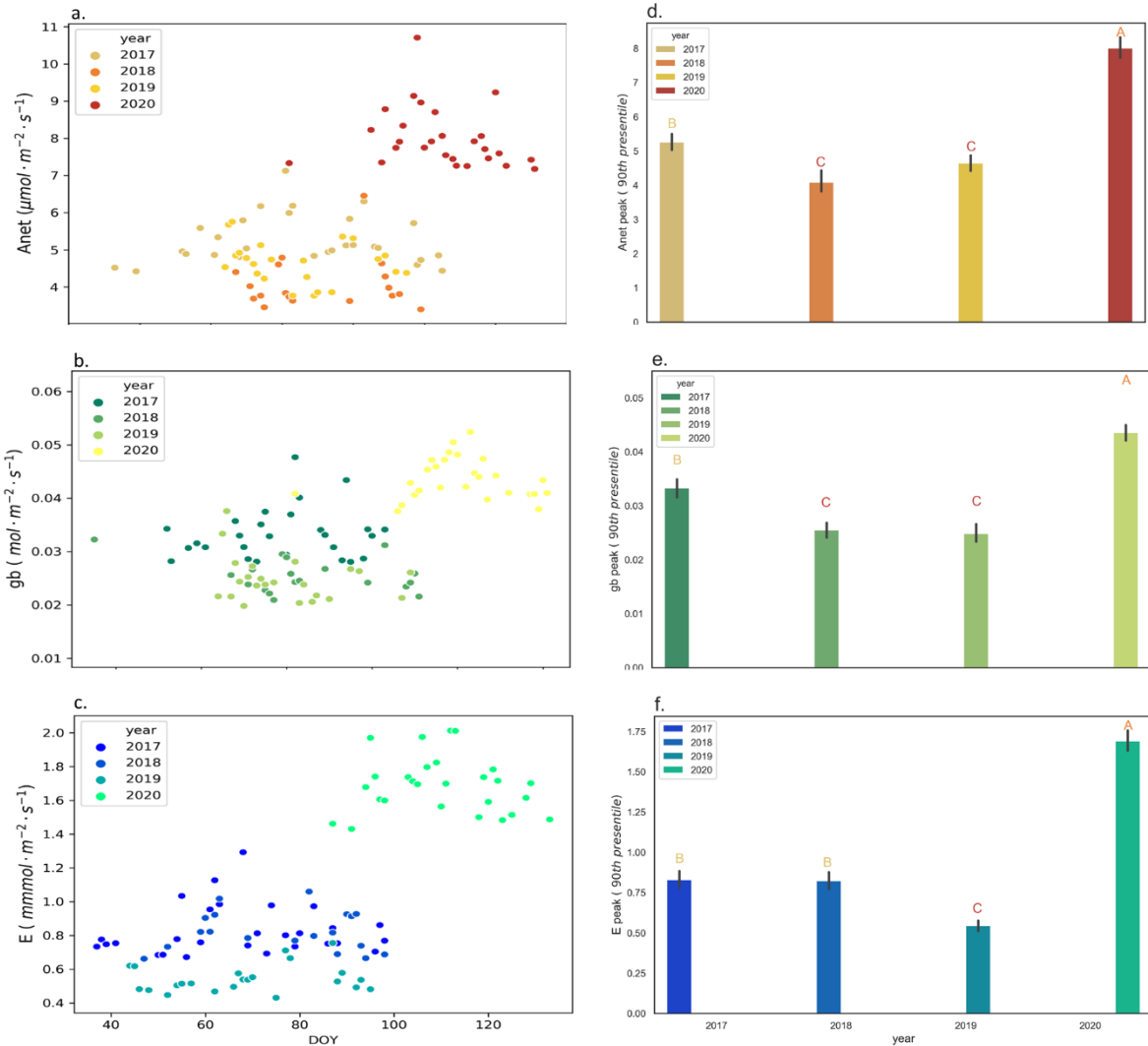


Figure 15 Peak activities timing (Pt) and rates (Pr) of leaf gas exchange (LGE): a) Rate of net Photosynthetic assimilation (Anet), b) Branch conductance to water vapor (gb) and c) Rate of Evaptranspiration (E) for the peak activity of the different years during the study period. For each subplot (a, b and c) the change of color match the change of year from 2017-2020. Points of different colors represent the days included in the peak activity period for each year, each point is a day-time average. Subplots d, e and f variables correspond with a, b and c subplots, showing the average \pm SD of the 90th percentile for each year of each variable. For each panel (d, e and f), different letters represent statistical differences between sample groups (One-Way Repeated-Measures, LSMeans Differences Tukey HSD test, $p < 0.05$). 2019 peak length is not reported due to lack of data at the peak period

4.3.5 WUE during the peak period

The peak activity in the different years occurred under different environmental conditions (Fig.s21). The different environmental conditions resulted in a differential change in the rate of Anet and E (Fig. 15). The resulting WUE (Anet/E) during the peak activity period in the different years ranged from 4 ± 1.1 ($\mu\text{molCO}_2 \cdot \text{mmolH}_2\text{O}^{-1}$) in 2020 to 4.7 ± 1.3 and 5.8 ± 1.4 in 2018 and 2017, respectively, and up to 8.1 ± 1.6 in 2019. Comparing Anet and E rates between the year with the highest and the year with the lowest WUE showed that in 2020, Anet was ~ 2 times and E was ~ 3 times higher than in 2019. The difrential change between E and Anet from the dryest to the wettest year led to the decrease in WUE during peak activity.

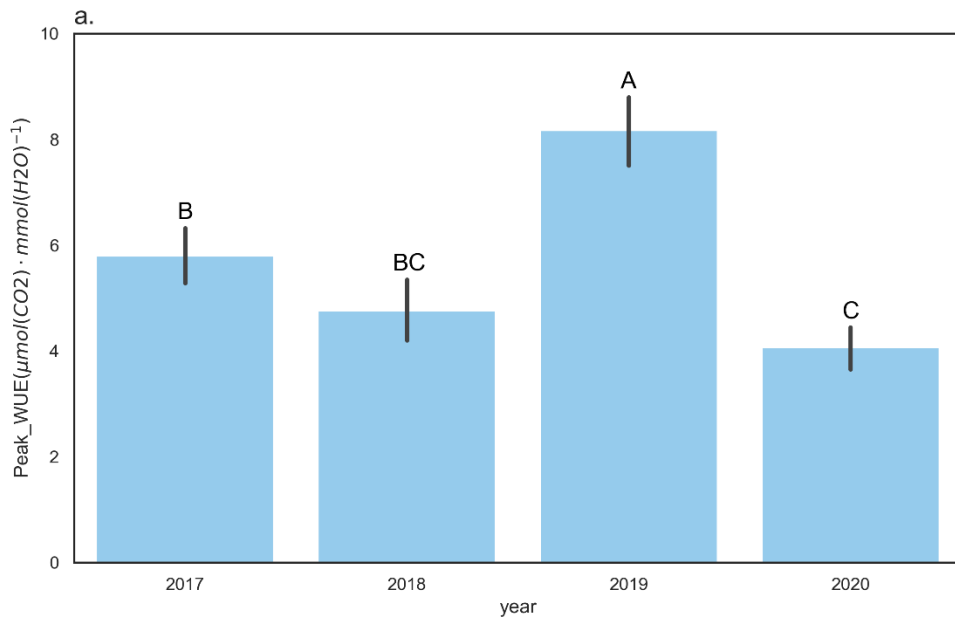


Figure 16. Average water use efficiency (WUE) at the peak activity period of the four years of the experiment (2017-2020). Values of WUE were calculated based on day time averages of Anet and E during thw peak period. Different letters represent statistical differences between sample groups (LSMeans Differences Tukey HSD test, $p < 0.05$).

To understand the cause of the differential change of the various LGE components, we examined the effect of the three most influential environmental factors (T, VPD, and SWC) on the WUE during the peak activity of the different years. The relationships depicted in Fig. 17 a and b indicate that the decrease in the WUE during peak activity can be explained by VPD and T. The average values of the WUE during the peak activity of the various years are arranged on curves a and b

according to the order from the highest WUE (2019) to the lowest (2020), as shown in Fig.16. The non-linear nature of the relationship between VPD (or T, which physically correlates with VPD) and WUE is also consistent with the fact that a small change in VPD at the low values, which are typical to the ‘peak activity period’, result in a significant change in WUE, while at high VPD and temperature, plants become less responsive (Tatarinov et al., 2016). In contrast to the T and VPD, it appears that SWC has no significant effect on the WUE during peak activity (Fig 17. C).

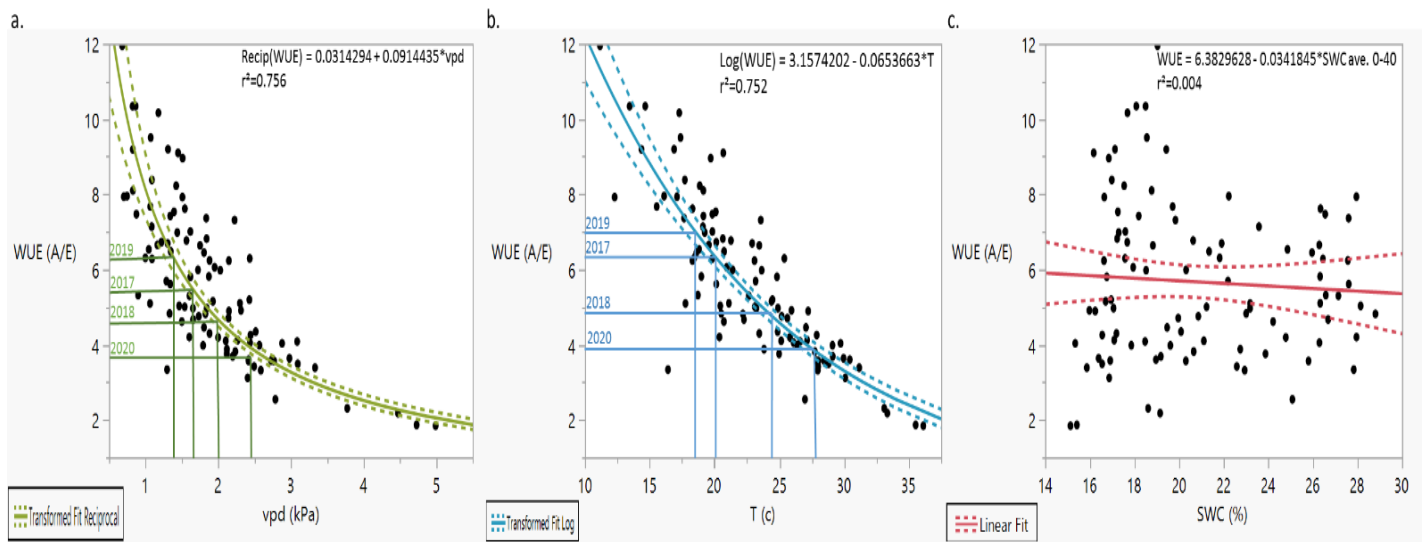


Figure 17. Water use efficiency (WUE) response to: a) Vapor pressure deficit (VPD), b) Temperature (T) and c) Soil water content (SWC) in the peak activity period. Black points are day-time averages WUE of all four study years. Solid lines are the best fit models and the dashed lines are the 95% confident interval. The vertical indicate the average VPD or T value of the different years, and the corresponding expected annual mean WUE value

4.4 Stress legacy effects on recovery

In this section, we examined the relationships between the stress length (MAP), and the recovery indicators, i.e. recovery time (Rt), recovery rate (Rr), and the peak activity rate (Pr) (Fig. 18). Rt of all LGE variables correlated with MAP, as follows: Rt lengthened as the duration of MAP increased. For E, although differences between MAP levels were significant (18, 89, and 107 days), the differences in Rt were relatively small (0-2 days). However, for Anet and gb, although the differences in MAP between years were smaller on average (35, 42, and 77 days), the differences in Rt were larger than for E, ranging between 1-10 days for Anet and 2-11days for gb (Fig. 18 a, d and g), thus better reflected the variations in MAP.

The relationship between Rr and MAP was similar for Anet and gb, but different for E. Rr of E showed higher values but did not change with different MAP levels in 2017-18 and 2019-20. In contrast, Rr of Anet and gb were ~2 times larger in 2019-20 than in 2017-18, corresponding to ~2 smaller MAP (Fig.18 b, e and h).

Examining the relationships of peak activity rate (Pr) and MAP for the different LGE may indicate that the two indicators were not linked. For all three LGE variables, higher MAP values in 2019 were followed by ~2 times higher peak activity in 2020 (Fig.18 c, f, and i).

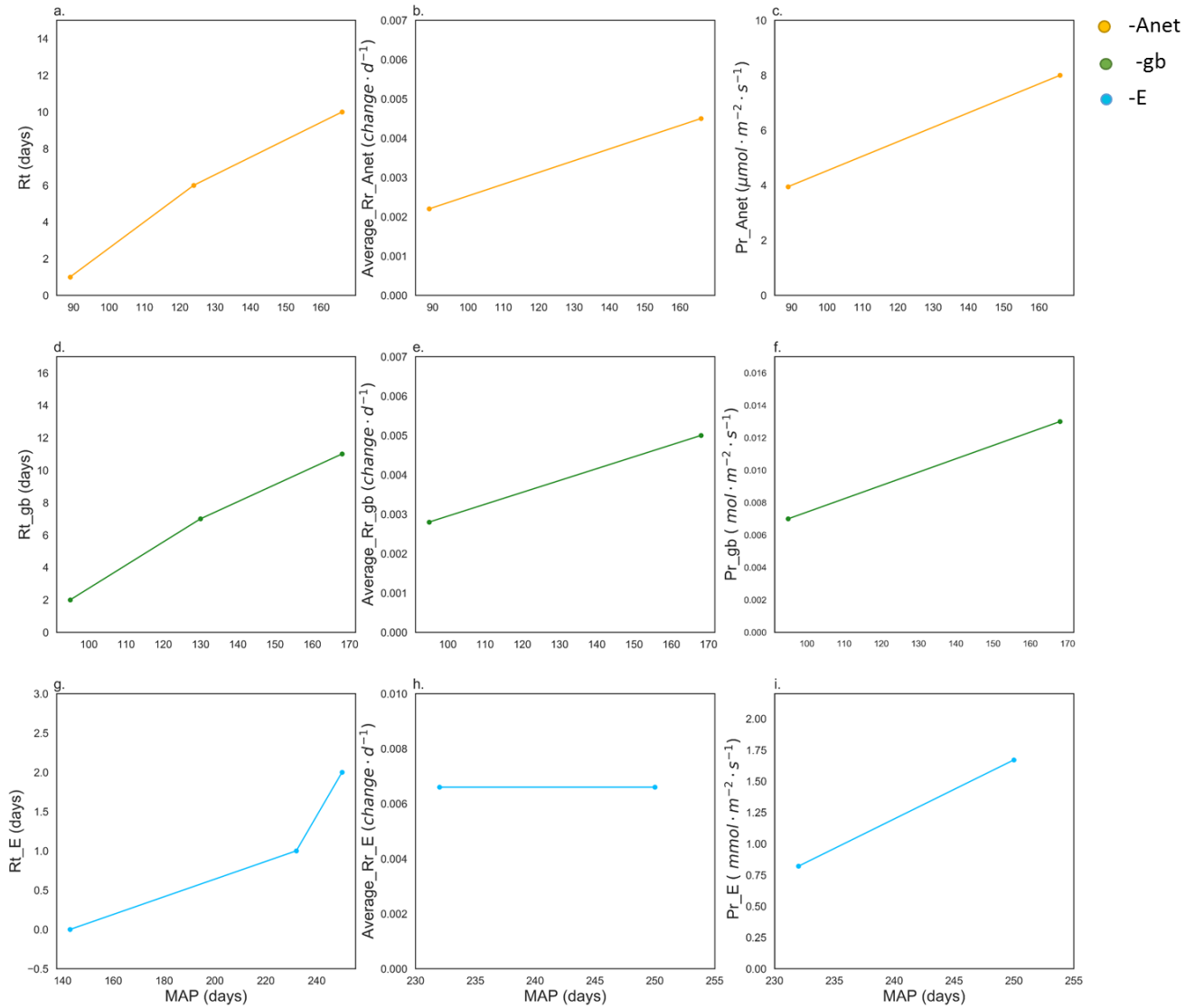


Figure 18. Recovery parameter and peak activity for different MAP of: a-c) Photosynthesis (Anet), d-f) Branch conductance to water vapor (gb) and g-i) Evapotranspiration (E). Left sub-plots (a, d and g) shows the recovery time (Rt) of Anet (a), gb (d) and E (g) for three stress intensity (SI) periods of 2017-18, 2019-20 and 2020-21. The middle sub-plots shows the Average recovery rate (Rr) per day for Anet (b), gb (e) and E (h) for two SI periods of 2017-18, 2019-20. Right sub-plots shows the peak activity rate (90th percentile; Pr) of the data for Anet (c), gb (f) and E (i) for two SI periods of 2017-18, 2019-20. For both recovery parameter and for the peak activity day time daily averages was used for the three leaf gas exchange variables. 2020-21 peak activity and recovery rate are not shown due to the fact that the data set ends in December 2020 before reaching the peak activity.

5. Discussion

5.1 Effective leaf area quantification

At the outset of this study, it became clear that for quantitative branch-scale studies, accurate effective leaf area quantification is critical. However, there was no standard and acceptable approach to measure or estimate the leaf area of a conifer in branch chambers. To address this, great efforts were invested in closing this gap.

In this study, we examined first the needle area based on two approaches: 1) the absolute surface area of the needles (TLSA). 2) the projected area based on the unique geometry of the needles and fascicle (PLA_2D and PLA_1D). And second, we estimated the effective leaf area in the branch chamber and the self-shading effects by two different correction methods (ELA_P and ELA_F). See table.1 for LA calculations (1-3) and effective LA correction (4 and 5).

For the LA calculations, we first estimated the total leaf surface area (TLSA; see Fig.s5), as well as the projected area based on the two needles (PLA_2D) or the single fascicle (PLA_1D; see Table.1 (1-3) for the LA calculation methods). Based on further analysis, we concluded that PLA_2D was the most relevant leaf area calculation method to use as an input for the ‘effective leaf area’ (ELA_P) correction. The choice of PLA_2D was made in two steps, the elimination step and the validation step. The elimination of the PLA_1D was based on the fact that the ratio between the LA and was lower than one, suggesting that the LA was smaller than the shadow it casts (Fig. 4c), which is unreasonable, and therefore PLA_1D was ignored. With the TLSA calculation, the ratio of LA to the IPLA was the highest, this difference between the TLSA to the shaded area is inherently high because the needles are not evenly lit from all directions at a given point in time, and therefore only part of their surface casts a shadow. This large difference between the shaded area and the lit area explains the low flux values obtained when using the total leaf surface area (Fig. s11). Due to the above issues, we used only the PLA_2D for estimates of the effective leaf area, for LGE calculations, and finally for comparisons with the Li-cor 6400 (Fig.8) for validation.

The effective LA corrections focused on the complex leaf arrangements in the branch chamber, which imposed self-shading and reduced the ‘effective’ leaf area involved in CO₂ uptake and evapotranspiration. In this part we examined two approaches: 1) the use of the ratio of the photographic image of the shade projected by the complex branch to the measured leaf area; 2) the

flux attenuation in response to an increasing number of twigs in the chamber. Based on these analyses, the photographic LA correction (ELA_p) proved to be the best way to correct for effective leaf area. The flux attenuation analysis (ELA_f) was used as a validation of this approach and showed a good correlation with ELA_p (see Fig. s16). In order to work with a consistent method, we chose the ELA_p correction since the correction is differential (according to the measured LA) and not constant as in the case of the ELA_f correction.

Considering both points discussed above, the LA calculation method of PLA_{2D} together with the ELA_p correction method were adopted in this study. Flux values calculated with the adopted method were validated against leaf cuvette gas exchange measurements (e.g. Licor 6400 leaf cuvette system; after correction, see Fig. 7 and 8). The comparison between the Anet rate calculated using the leaf area based on the two corrections methods (ELA_p and ELA_f) and that obtained from the leaf cuvette (corrected Li-cor 6400) showed no statistical difference (Fig. 8, a, c and e). For E, however, the corrected values of E measured in the leaf cuvette were higher than E determined in the branch chambers (Fig. 8, b, and d). The fact that in two cases the corrected leaf-cuvette E did not match branch-chamber E might be related to temperature differences between the measurements of the different methods. For comparison, flux data under high PPFD (higher than the saturation point; see Fig.s15 b) were used. At the time of the year we conducted the comparison (November and October 2020), ambient PPFD was not at its annual maximum, and data of PPFD saturation from the branch chambers was not abundant. Consequently, E values from the branch chambers were taken from a wider temperature and VPD range from those of the leaf cuvette and may have been measured at a lower temperature and VPD that affected E rate but not Anet rate.

The range of values between the annual minimum (10th percentile) to maximum (90th percentile) activity obtained from the different LGE variables using the ELA_p correction were in agreement with ranges reported in previous studies obtained by LI-COR 6400 leaf cuvette measurements (Grünzweig, Lin, Rotenberg, Schwartz, & Yakir, 2003; Klein et al., 2016, 2013; Maseyk, 2006). The agreement between the corrected values from the branch chambers both in the saturated part of the Anet and E light response curves and in the range of activity rate from different years and different studies illustrates the robustness of the corrections. We propose that our extensive study

of the ‘effective’ leaf area in branch chamber studies should serve as a basis for a standard approach in this field.

5. 2 Interactions of precipitation patterns, soil moisture, and stress period

As shown by previous studies and the results of this work, LGE is strongly dependent on environmental conditions, such as SWC and VPD (Fig. 10). In dry ecosystems, this dependence is enhanced due to prolonged periods of low soil water availability combined with high VPD (dos Santos et al., 2013; Garonna et al., 2018; Marques et al., 2020; Thomas et al., 2009). An important aspect of these interactions is the compensating effect that large rain events and the timing of rainfall during low VPD periods have on the overall low precipitation amount. This compensatory effect can be manifested given that no runoff takes place and the large rainfall events saturate the soil rather than leave the ecosystem. Yatir Forest ecosystem meets this condition, and the compensating effect influences the amount of available water in the soil during the wet season and shortens the minimal activity period (MAP), which in turn might affect the trees’ survival in water-limited environments (Cobb et al., 2017; Preisler, 2014; Raz-Yaseef, Yakir, Schiller, & Cohen, 2012; Wang et al., 2020).

The interactions of P, VPD, SWC, and the “compensation effects” in the present study are summarized in Fig. 11. The low SWC in the 2018-19 rainy season might be explained by two main factors. First, in the wet period of 2018-19, the rainfall was distributed over 29 rain events over six months (Fig 11b, dark green bars), when 47% of the annual precipitation was early in the wet season (October and November), and at the end of the wet season (March) when the potential evapotranspiration (PET), and consequently VPD, were high (Fig. 11b, orange points). Moreover, the only large rain event of the 2018-19 rainy season happened in November when PET was high (Fig. 11b), possibly reducing the water permeability to the ground due to high VPD that enhanced soil evaporation. Second, in the 2018-19 rainy season, both the amount of rain and the average rain event size were relatively small, compared with the same months in 2016-17 (Fig. 11a and b, light green bars), making the change in SWC less pronounced than in 2016-17 (Fig. 11b, blue points). In addition, in the 2018-19 rainy season, only one of the rain events was larger than 30 mm, a factor that was found to affect SWC in a previous study (Raz-Yaseef et al., 2012).

In contrast to the 2018-19 winter, the total rain amount of 2016-17 was distributed over 20 events, when 95% of the rainfall happened in three consecutive months with low VPD, from December to February (Fig. 11a). In addition, two of the 20 events were larger than 30 mm, with a total amount of 66 mm that made up 26% of the total rainfall. As shown in previous studies, the combination of high total rainfall with large rainfall events, at a time of low PET is the combination that leads to a significant impact on SWC at the root zone, and, in turn, beneficial impact on the trees' physiological activity, as long as only a little rainwater is lost from the forest in the form of runoff.

As discussed above, the compensating effect of the rainfall pattern might affect the 'dry season' length, and therefore the MAP. The shortening of the 'dry season' in turn, increases the 'window of opportunity' for carbon assimilation by the trees. As shown in Figures s17 and s18, and in previous studies, VPD effects on Anet and gb are subjected to the SWC status (Fernandes-Silva, López-Bernal, Ferreira, & Villalobos, 2016; Preisler, 2020). For example, when SWC is high, an increase in VPD under sufficient levels of PAR, positively affects Anet and gb, up to the threshold of ~3.4 kPa (see Fig. s17). On the other hand, when SWC is low, an increase in VPD limits Anet and gb already at low levels of VPD (~1.4 kPa). These indicate that the compensating effects discussed above might result in lower MAP for all LGE variables and positively affect tree physiological activity and growth. Consistent with our findings of this study, both Raz-Yaseef et al., 2012 and Dorman et al., 2015 showed that the amount of large rain events (>30mm) has a significant impact on forest productivity. In addition, Assefa, 2019 showed that the distribution of large rain events determines the seasonal SWC dynamics (Assefa, 2019; Dorman, Perevolotsky, Sarris, & Svoray, 2015; Raz-Yaseef et al., 2012).

5.3 The onset of minimal activity period (MAP) in response to SWC and VPD

The length of the stress period caused by low SWC or high VPD resulted in different MAP for the different LGE variables, indicating a different response to these environmental stressors. While MAP of E was correlated with the length of the dry period ($SWC < tSWC$), MAP of Anet and gb showed a stronger correlation with the length of the 'maximal VPD period' (Fig. 10). While the end of the environmental stress period and the activity restoration showed a high correlation, we observed some discrepancies between the start of the environmental stress period and the time of MAP start.

In the case of E, we observed divergence between the start of the dry period ($SWC < tSWC$) and the start of MAP, with the onset of the ‘dry season’ preceding that of MAP. A significant offset of 65 days was observed in 2020, compared with 10 and 5 days in 2017 and 2019 respectively (Fig. 10b). In 2020, the amount of precipitation was particularly high, and it resulted in a significant increase in SWC down to 1 m depth. SWC at 1 m depth in relatively dry winters (2017-18 and 2018-19) showed no significant increase. Data of SWC at 1 m in winter 2016-17 were not available, but the correlation between the annual rain sum to the change in SWC at 1m depth (see Fig. s19) indicated that there was probably no change in SWC at a depth of 1m that winter.

The time offset of 2020 noted above seems to stem from our definition of tSWC, which is based on the retention curve done by Klein *et.al* 2014, who determined the tSWC limit for depths of 0-60 cm. Setting the tSWC threshold considering the soil profile up to a depth of 1m could change its value, and hence also change the time point of the beginning of the ‘dry season’. When we examined the time difference between the start of MAP of E and the decrease of the SWC at 1m depth to pre-wetting values the observed offset was reduced from 65 to 9 days. Based on the discussion above, it seems that assessing the ‘dry season’ length should rely on tree water use beyond the main root zone, which is at the top 60 cm in the study site (Klein et al., 2014; Preisler et al., 2019).

In contrast to E, Anet and gb MAP showed a higher correlation to the ‘maximal VPD period’, rather than to the stress period determined by SWC. A significant difference was observed between the onset of the ‘maximal VPD period’ and the beginning of the MAP for both 2017 and 2020, with differences of 24 and 51 days respectively, but not for 2019 when the difference was only 9 days.

These results led us to suggest that the onset of the MAP reflects interactions between SWC and VPD in the following way: Once the ecosystem is within the ‘maximal VPD period’, the actual onset of the MAP is then dictated by the SWC reaching a low threshold. This conclusion is supported by the observations that SWC level at the time of the onset of the MAP of Anet and gb (at the ‘maximal VPD period’) was similar in the different years. It showed an average value of $13.1 \pm 0.13\%$ in all cases. This finding is in agreement with Preisler, 2020, who showed that LGE remains at a high level under well-watered conditions, even at high VPD (Preisler, 2020).

5.4 Recovery from SWC and VPD stress of LGE parameters

The relief from the stress period imposed by SWC or VPD is followed by the recovery of the different LGE variables. We found good temporal agreement between the stress removal and the restoration of LGE variables. Note, however, that Anet and gb responded to VPD stress relief, while E responded to SWC stress relief (Fig. 11 a, b, and c).

As discussed above, the results of E response to SWC stress indicated the importance of considering SWC also below the main root zone depth (0-60 cm). Thus, when no change in SWC of the deeper layer (1 m in our case) is observed, the tSWC threshold in the main root zone acts as an on/off switch for transpiration at the start and end of the 'dry season'. But a time lag can develop when SWC at depth increased (e.g. in very wet years such as 2020). These findings reinforce the findings of Klein *et.al* (2014) in most years, but with a caveat regarding exceptionally wet years.

Comparing with E, the timing of recovery of Anet and gb were strongly linked with the end of the 'maximal VPD period', but not with the end of the dry season. Note also that the onset of the Anet and gb recovery always preceded that of E, despite high interannual variations. This resulted in a time lag between the onset of recovery of the different LGE variables. Such effects have been explained by different regulations of the different LGE components under varying water and VPD stress levels (Ye & Yu, 2008).

An important consequence of the temporal offset in the recovery of Anet and E (end of September. And beginning of January, respectively) is the observed increase in water use efficiency (WUE) that reaches its maximum values in December-January (Fig. 13). Both the annual patterns and the values of WUE are in agreement with previously reported trends and values in three other evergreen, Mediterranean sites (Grünzweig *et al.*, 2003; Reichstein *et al.*, 2002).

5.5 Possible interactions of recovery parameters and stress period length

The results clearly showed that there is a time offset between the end of the environmental stress period (i.e. when SWC and VPD recover across a threshold; stress relieve), and the timing of the functional recovery (i.e. when the LGE variable exceed the 'minimal activity period' mean; activity restoration). The question that arises, therefore, is whether there is a link between the MAP and the length of the offset?

The results support such a link (Fig. 18a, d, and g), as initially hypothesized (see section 2.2). The recovery time (R_t) of all LGE variables showed a good correlation with MAP, i.e., the longer the MAP, the longer the difference between the time of ‘stress relief’ and the time of activity restoration (Fig.11a, d, and g). Note, however, the differences in R_t of E (relatively uniform and fast), and of Anet and gb (slow and highly variable; Fig.11). This was also demonstrated in many previous studies (Ruehr et.al, 2019).

According to Flexas *et.al*, (2006), when gb is lower than $0.05 \text{ mol m}^{-2}\cdot\text{s}^{-1}$, which is a typical rate in the dry season in Yatir, the carboxylation capacity decreases and the leaves need to restore their carboxylation capacity after the stress relief (Flexas, et al., 2006). Energy for repairing the hydraulic and photosynthetic systems is also limited after long MAP due to depleted carbon reserves (Galiano, Martínez-Vilalta, & Lloret, 2011, Ruehr et.al, 2019). These findings might explain the longer R_t for Anet and gb after long MAP.

Considering the recovery rate (R_r), and its correlation with antecedent MAP, no clear link was observed (Fig.18b, e and h), consistent with previous reports (Schwalm et al., 2017). Furthermore, it seems that the R_r in different years is similar when considered within the rainy season. For example, the apparent R_r in 2017 and 2020 was different. However, the recovery occurred in late summer, before the onset of rains, while in 2020, it occurred after the onset of rains. If we consider R_r only after the onset of the rainy season, similar values are obtained. The main conclusion is therefore that while the onset of Anet and gb recovery is related to the VPD ‘stress relief’, but high R_r is attained only after the onset of rainfall and increase in SWC as demonstrated in a recent study by (Liu et al., 2020).

Notably, while we focused on the ‘stress relieve’ associated with VPD, the temperature can also be an important factor. Previous studies have shown that the optimum temperature for Anet and stomatal conductance (g_s) in C3 plants in general, and in *Pinus halepensis*, in particular, is ranging between 20-30°C and 18-28°C, respectively (Bonan, 2013; Sperlich, Chang, Peñuelas, & Sabaté, 2019). Indeed, our measurements in 2017 showed that the decline of temperature below the limiting value of 30°C was correlated with a decline in VPD (Fig. s20), consequently, it was difficult to separate the effect of temperature and VPD on the increase of Anet and gb.

5.6 Interactions of post-stress peak rates and the stress period length

As indicated by our results (Fig. 18.c, f and i), ‘peak activity’ (Pr) of the various LGE variables did not correlate with the MAP length. Our results demonstrate that the ‘peak activity’ levels of the different LGE components were not affected by antecedent stress levels or duration. Thus, it is suggested that long MAP did not result in a negative impact on the LGE in the next productive season, or a so-called negative ‘legacy effect’. These findings contradict studies in the field that have examined the effect of drought events on annual tree rings (Anderegg et al., 2015; Camarero et al., 2018). Note, however, that even when legacy effects can be observed in tree ring analysis, such as following the severe drought event in 2012 in a Midwestern US forest (~10% reduction in tree-ring width increment in the following year), it was not observed when examining LGE (Kannenbergh et al., 2019). The differential effect of drought on tree rings and gas exchange demonstrates that growth is more, and earlier restricted than Anet as shown previously by Muller et al., 2011 (B. Muller et al., 2011).

Our results further indicate that the ‘peak activity’ levels of the various LGE components were closely linked with the concurrent environmental conditions (unlike the analysis of MAP). The interannual variability in environmental conditions during the subsequent ‘peak activity period’, resulted in variability in both the rate and timing of this period (Fig. 15). However, this response can take different forms, in case the timing of the rainy season is different, or when the conditions during a similar rainy season vary.

For the first case, we see that for all LGE variables, the post-stress ‘peak activity’ of 2020 was later than in the other years due to the long rainy season (195 days compared with 130 ± 23 days in 2017-2019). This helps keep the SWC in 2020 high until late in the following spring-early summer period. As shown by Wang *et al.*, (2020), the length of the ‘peak activity’ in the Yatir forest, is defined by the combined effects of decreasing SWC and increasing temperature and radiation in spring. In 2017-2019, SWC imposed a ‘peak activity period’ in sub-optimal radiation and temperature conditions. In 2020, however, the long wet period allowed optimal conditions of SWC, radiation, and temperature to co-occur, accompanied also by high VPD values (Fig. s21 a and b). This unusual combination of environmental conditions resulted in later and higher LGE ‘peak activity’ than in the other years.

In the second case, as can be seen in Fig.15, the ‘peak activity’ of the different LGE variables in the years 2017, 2018 and 2019 showed different rates in the different years even though the time in the year was quite similar (between DOY 36 and DOY 98). As stated above, during the ‘peak activity’ of the different years the values of T and VPD varied considerably (Fig. s21 a and b), resulting in different ‘peak activity’ levels in the different years and LGE variables.

5.7 WUE reflects differential environmental effects on the different LGE components

Previous studies that were done in the Yatir forest had shown that different combinations of SWC, leaf Ψ_w , and VPD may result in decoupling between water and carbon fluxes, and therefore affect the water use efficiency (Maseyk, 2006; Maseyk, Hemming, Angert, Leavitt, & Yakir, 2011). For example, drier conditions and lower VPD resulted in higher WUE. As expected, in the present study too, the change in the SWC and VPD conditions led to a differential change in Anet and E during the ‘peak activity period’ (Fig. 15), and consequently to a significant difference in WUE between years, as shown in Fig. 16 and 17.

The results provided two contrasting examples of this. The first case is the comparison of ‘peak activity’ between 2017 and 2018, with similar SWC, but different VPD (Fig. s21). In this case, 2017 ‘peak activity’ showed higher Anet but similar E compared with that of 2018, resulting in higher WUE in 2017 (see Fig.15 and 16). As demonstrated before, when SWC is high, an increase in VPD causes a decrease in gb and Anet but has little effect on E (Tatarinov *et al.*, 2016; Preisler, 2020; McAdam and Brodribb, 2015; Novick *et al.*, 2016). The lower VPD at the ‘peak activity’ period of 2017 resulted in higher gb compared with 2018, and thus the Anet in 2017 was also higher.

The second case, contrast, 2019 and 2018 with similar Anet while the rate of E was significantly lower in 2019. In 2019, lower SWC resulting in lower leaf water potential (Fig. s22), combined with lower VPD resulted in lower E. This did not have significant effects on Anet and therefore supported higher WUE in that year. This observation is supported by the results of Tatarinov *et al.* (2015) that showed that changes in CO₂ flux can be expected only when gb decreases due to increasing VPD, under high SWC conditions. The E response noted above is also consistent with the work of Vesala *et al.*, 2017 showing that E is proportional to the gradient between the water vapor concentration in the sub-stomatal cavity, and water vapor concentration in the ambient air

(i.e., VPD) which reflects in Ψ_w (Mielke et al., 2000; Vesala et al., 2017). In the case of the ‘peak activity period’ of 2019 the low Ψ_w and VPD reduced the driving force for E.

Finally, it is important to note that despite the apparent contrasting behavior between the years discussed above, the changes in WUE across years are systematic and must reflect a similar physiological response, as shown in Fig. 17.

The discussion above seems to indicate that changes in WUE values can be explained by the consistent but differential effects of the environmental factors at the ‘peak activity period’ on the individual LGE components, g_b and A_{net} , on the one hand, and E, on the other hand.

5.8 Conclusions

We utilized a long-term dataset, obtained from our automatic branch chambers gas exchange measurement system to study the effect of the length of environmental stressors on the recovery and post-stress activity of *Pinus halepensis* at the dry edge of the Mediterranean climate.

We obtained accurate quantitative data of branch-level water and carbon fluxes using a new methodology for effective leaf area quantification. The flux rates calculated using the effective leaf area were compared to our standard, the Li-cor 6400, and showed that our method is robust. The different variables of the leaf gas exchange (LGE) were the parameters by which we assessed the activity level of the trees under changing environmental conditions.

We developed a new framework to assess the effect of the two main environmental stressors in dry and hot ecosystems, i.e high VPD and low SWC, on the recovery and post-stress activity of different LGE variables. Our results demonstrate that different variables of the LGE respond differently to different environmental stressors. While E seasonal cycle was strongly linked with the SWC level, the annual cycles of A_{net} and g_b were more linked with the VPD level. We further demonstrate that although g_b and A_{net} were closely linked with the VPD level, their increase under decreasing VPD is limited under low SWC conditions.

We also found evidence that the length of the minimal activity period imposed by environmental stress does affect the recovery time (the time between stress relief and activity restoration), But

not on the recovery rate or post-stress activity that were more affected by the environmental conditions prevailing at the time.

These results suggest that the prolonged dry season expected in the future may cause the productive season to shorten but does not pose a threat to forests in a semi-desert environment, provided that the SWC and temperatures during the productive season will remain optimal. In addition, the projected decrease in precipitation might be compensated by a change in their pattern, when in an arid environment where there is no runoff the vegetation can benefit from large rainfall events concentrated in the cold months of winter.

6. References

- Anderegg, W. R.L., Schwalm, C., Biondi, F., Camarero, J. J., Koch, G., Litvak, M., ... Pacala, S. (2015). Pervasive drought legacies in forest ecosystems and their implications for carbon cycle models. *Science*, 349(6247), 528–532. <https://doi.org/10.1126/science.aab1833>
- Anderegg, William R.L., Wolf, A., Arango-Velez, A., Choat, B., Chmura, D. J., Jansen, S., ... Pacala, S. (2018). Woody plants optimise stomatal behaviour relative to hydraulic risk. *Ecology Letters*, 21(7), 968–977. <https://doi.org/10.1111/ele.12962>
- Arthur Sampson, D., & Smith, F. W. (1993). Influence of canopy architecture on light penetration in lodgepole pine (*Pinus contorta* var. *latifolia*) forests. *Agricultural and Forest Meteorology*, 64(1–2), 63–79. [https://doi.org/10.1016/0168-1923\(93\)90094-X](https://doi.org/10.1016/0168-1923(93)90094-X)
- Assefa, S. (2019). *No Title*. Weizmann institute.
- Bamberger, I., Ruehr, N. K., Schmitt, M., Gast, A., Wohlfahrt, G., & Arneth, A. (2017). Isoprene emission and photosynthesis during heat waves and drought in black locust. *Biogeosciences Discussions*, 1–26. <https://doi.org/10.5194/bg-2017-32>
- Muller, B., Pantin, F., Génard, M., Turc, O., Freixes, S., Piques, M., & Gibon, Y. (2011) Water deficits uncouple growth from photosynthesis, increase C content, and modify the relationships between C and growth in sink organs, *Journal of Experimental Botany*, Volume 62, Issue 6, March 2011, Pages 1715–1729
- Birami, B., Gattmann, M., Heyer, A. G., Grote, R., Arneth, A., & Ruehr, N. K. (2018a). Heat Waves Alter Carbon Allocation and Increase Mortality of Aleppo Pine Under Dry Conditions. *Frontiers in Forests and Global Change*, 1(November), 1–17. <https://doi.org/10.3389/ffgc.2018.00008>
- Birami, B., Gattmann, M., Heyer, A. G., Grote, R., Arneth, A., & Ruehr, N. K. (2018b). Heat Waves Alter Carbon Allocation and Increase Mortality of Aleppo Pine Under Dry Conditions. *Frontiers in Forests and Global Change*, 1(November), 1–17. <https://doi.org/10.3389/ffgc.2018.00008>

- Blackman, C. J., Brodribb, T. J., Jordan, G. J., Jordan, J., & Blackman, J. (2014). Leaf hydraulic vulnerability is related to conduit dimensions and drought resistance across a diverse range of woody angiosperms. *New Phytologist Research*, 188(4), 1113–1123.
- Bonan, G. B. (2008). Forests and climate change: Forcings, feedbacks, and the climate benefits of forests. *Science*, 320(5882), 1444–1449. <https://doi.org/10.1126/science.1155121>
- Bonan, G. B. (2013). Leaf photosynthesis. *Ecological Climatology*, 237–252. <https://doi.org/10.1017/cbo9780511805530.018>
- Breuninger, C., Oswald, R., Kesselmeier, J., & Meixner, F. X. (2012). The dynamic chamber method: Trace gas exchange fluxes (NO, NO₂, O₃) between plants and the atmosphere in the laboratory and in the field. *Atmospheric Measurement Techniques*, 5(5), 955–989. <https://doi.org/10.5194/amt-5-955-2012>
- Brodribb, T. J., & McAdam, S. A. M. (2013). Abscisic acid mediates a divergence in the drought response of two conifers. *Plant Physiology*, 162(3), 1370–1377. <https://doi.org/10.1104/pp.113.217877>
- Buck Arden L. (1981). *New Equations for Computing Vapor Pressure and Enhancement Factor*. 1527.
- Camarero, J. J., Gazol, A., Sangüesa-Barreda, G., Cantero, A., Sánchez-Salguero, R., Sánchez-Miranda, A., ... Ibáñez, R. (2018). Forest growth responses to drought at short- and long-term scales in Spain: Squeezing the stress memory from tree rings. *Frontiers in Ecology and Evolution*, 6(FEB), 1–11. <https://doi.org/10.3389/fevo.2018.00009>
- Cobb, R. C., Ruthrof, K. X., Breshears, D. D., Lloret, F., Aakala, T., Adams, H. D., ... Zeppel, M. J. B. (2017). Ecosystem dynamics and management after forest Die-Off: A global synthesis with conceptual state-and-transition models. *Ecosphere*, 8(12). <https://doi.org/10.1002/ecs2.2034>
- Cruz, M. de la, Quintana-Ascencio, P., Cayuela, L., Espinosa, C., & Escudero, A. (2017). More than Drylands but Less of Dry Forests. *BioRxiv*, 147942. <https://doi.org/10.1101/147942>
- Dangel, U. (2016). The World's Forests. In *Turning Point in Timber Construction*. <https://doi.org/10.1515/9783035608632-002>

- Dorman, M., Perevolotsky, A., Sarris, D., & Svoray, T. (2015). Amount vs. temporal pattern: On the importance of intra-annual climatic conditions on tree growth in a dry environment. *Journal of Arid Environments*, *118*, 65–68. <https://doi.org/10.1016/j.jaridenv.2015.03.002>
- dos Santos, C. M., Verissimo, V., Wanderley Filho, H. C. de L., Ferreira, V. M., Cavalcante, P. G. da S., Rolim, E. V., & Endres, L. (2013). Seasonal variations of photosynthesis, gas exchange, quantum efficiency of photosystem II and biochemical responses of *Jatropha curcas* L. grown in semi-humid and semi-arid areas subject to water stress. *Industrial Crops and Products*, *41*(1), 203–213. <https://doi.org/10.1016/j.indcrop.2012.04.003>
- Duffy, K. A., Schwalm, C. R., Arcus, V. L., Koch, G. W., Liang, L. L., & Schipper, L. A. (2021). How close are we to the temperature tipping point of the terrestrial biosphere? *Science Advances*, *7*(3), 1–9. <https://doi.org/10.1126/sciadv.aay1052>
- Evans, J. P. (2009). 21st century climate change in the Middle East. *Climatic Change*, *92*(3–4), 417–432. <https://doi.org/10.1007/s10584-008-9438-5>
- Eyal Rotenberg, & Yakir, D. (2010). *Zizpus*. *327*(327), 451–454.
- Fernandes-Silva, A. A., López-Bernal, Á., Ferreira, T. C., & Villalobos, F. J. (2016). Leaf water relations and gas exchange response to water deficit of olive (cv. Cobrançosa) in field grown conditions in Portugal. *Plant and Soil*, *402*(1–2), 191–209. <https://doi.org/10.1007/s11104-015-2786-9>
- Flexas, J., Bota, J., Galmés, J., Medrano, H., & Ribas-Carbó, M. (2006). Keeping a positive carbon balance under adverse conditions: Responses of photosynthesis and respiration to water stress. *Physiologia Plantarum*, *127*(3), 343–352. <https://doi.org/10.1111/j.1399-3054.2006.00621.x>
- Freeman, B. M. (1980). Temperate forest trees and stands under severe drought. *Research in Veterinary Science*, *28*(3), 389–390. [https://doi.org/10.1016/s0034-5288\(18\)32731-0](https://doi.org/10.1016/s0034-5288(18)32731-0)
- Galiano, L., Martínez-Vilalta, J., & Lloret, F. (2011). Carbon reserves and canopy defoliation determine the recovery of Scots pine 4yr after a drought episode. *New Phytologist*, *190*(3), 750–759. <https://doi.org/10.1111/j.1469-8137.2010.03628.x>
- Garonna, I., De Jong, R., Stöckli, R., Schmid, B., Schenkel, D., Schimel, D., & Schaepman, M. E.

- (2018). Shifting relative importance of climatic constraints on land surface phenology. *Environmental Research Letters*, 13(2). <https://doi.org/10.1088/1748-9326/aaa17b>
- Gonsamo, A., Chen, J. M., & Ooi, Y. W. (2018). Peak season plant activity shift towards spring is reflected by increasing carbon uptake by extratropical ecosystems. *Global Change Biology*, 24(5), 2117–2128. <https://doi.org/10.1111/gcb.14001>
- Grace, J. C. (1987). Note: Theoretical ratio between “one-sided” and total surface area for pine needles. *New Zealand Journal of Forestry Science*, 17(2–3), 292–296.
- Gray, V. (2007). Climate change 2007: The physical science basis summary for policymakers. *Energy and Environment*, 18(3–4), 433–440. <https://doi.org/10.1260/095830507781076194>
- Gregersen, H., Lundgren, A., & Byron, N. (1998). Forestry for sustainable development. *Journal of Forestry*, 96(3), 6–10. <https://doi.org/10.1093/jof/96.3.6>
- Griffith, D. M., Lehmann, C. E. R., Strömberg, C. A. E., Parr, C. L., Pennington, R. T., Sankaran, M., ... Bond, W. J. (2017). Comment on “The extent of forest in dryland biomes.” *Science*, 358(6365), 27–30. <https://doi.org/10.1126/science.aao1309>
- Grossiord, C., Buckley, T. N., Cernusak, L. A., Novick, K. A., Poulter, B., Siegwolf, R. T. W., ... McDowell, N. G. (2020). Plant responses to rising vapor pressure deficit. *New Phytologist*, 226(6), 1550–1566. <https://doi.org/10.1111/nph.16485>
- Grünzweig, J.M., T.Lin, E.Rotenberg, A.Schwartz, & D.Yakir. (2003). *Carbon sequestration in arid-land forest*. 791–799.
- Grünzweig, J. M., Gelfand, I., Fried, Y., & Yakir, D. (2007). Biogeochemical mechanisms contributing to enhanced carbon sequestration following afforestation in a semi-arid region. *Biogeosciences*, 4, 891–904.
- Grünzweig, J. M., Lin, T., Rotenberg, E., Schwartz, A., & Yakir, D. (2003). Carbon sequestration in arid-land forest. *Global Change Biology*, 791–799.
- Haverd, V., Smith, B., Canadell, J. G., Cuntz, M., Mikaloff-Fletcher, S., Farquhar, G., ... Trudinger, C. M. (2020). Higher than expected CO₂ fertilization inferred from leaf to global observations. *Global Change Biology*, 26(4), 2390–2402. <https://doi.org/10.1111/gcb.14950>

- Huang, J., Ji, M., Xie, Y., Wang, S., He, Y., & Ran, J. (2016). Global semi-arid climate change over last 60 years. *Climate Dynamics*, 46(3–4), 1131–1150. <https://doi.org/10.1007/s00382-015-2636-8>
- Ingrisch, J., & Bahn, M. (2018). Towards a Comparable Quantification of Resilience. *Trends in Ecology and Evolution*, 33(4), 251–259. <https://doi.org/10.1016/j.tree.2018.01.013>
- Jarraud, M., & Steiner, A. (2012). Summary for policymakers. In *Managing the Risks of Extreme Events and Disasters to Advance Climate Change Adaptation: Special Report of the Intergovernmental Panel on Climate Change* (Vol. 9781107025). <https://doi.org/10.1017/CBO9781139177245.003>
- Kannenberg, S. A., Novick, K. A., Alexander, M. R., Maxwell, J. T., Moore, D. J. P., Phillips, R. P., & Anderegg, W. R. L. (2019). Linking drought legacy effects across scales: From leaves to tree rings to ecosystems. *Global Change Biology*, 25(9), 2978–2992. <https://doi.org/10.1111/gcb.14710>
- Klein, T. (2020). A race to the unknown: Contemporary research on tree and forest drought resistance, an Israeli perspective. *Journal of Arid Environments*, 172(August 2018), 104045. <https://doi.org/10.1016/j.jaridenv.2019.104045>
- Klein, T., Cohen, S., Paudel, I., Preisler, Y., Rotenberg, E., & Yakir, D. (2016). Diurnal dynamics of water transport, storage and hydraulic conductivity in pine trees under seasonal drought. *IForest*, 9(5), 710–719. <https://doi.org/10.3832/ifor2046-009>
- Klein, T., & Hoch, G. (2015). Tree carbon allocation dynamics determined using a carbon mass balance approach. *New Phytologist*, 205(1), 147–159. <https://doi.org/10.1111/nph.12993>
- Klein, T., Rotenberg, E., Cohen-Hilaleh, E., Raz-Yaseef, N., Tatarinov, F., Preisler, Y., ... Yakir, D. (2014). Quantifying transpirable soil water and its relations to tree water use dynamics in a water-limited pine forest. *Ecohydrology*, 7(2), 409–419. <https://doi.org/10.1002/eco.1360>
- Klein, T., Shpringer, I., Fikler, B., Elbaz, G., Cohen, S., & Yakir, D. (2013). Relationships between stomatal regulation, water-use, and water-use efficiency of two coexisting key Mediterranean tree species. *Forest Ecology and Management*, 302, 34–42. <https://doi.org/10.1016/j.foreco.2013.03.044>

- Kooijmans, L. M. J., Maseyk, K., Seibt, U., Sun, W., Vesala, T., Mammarella, I., ... Chen, H. (2017). Canopy uptake dominates nighttime carbonyl sulfide fluxes in a boreal forest. *Atmospheric Chemistry and Physics*, *17*(18), 11453–11465. <https://doi.org/10.5194/acp-17-11453-2017>
- Liu, L., Gudmundsson, L., Hauser, M., Qin, D., Li, S., & Seneviratne, S. I. (2020). Soil moisture dominates dryness stress on ecosystem production globally. *Nature Communications*, *11*(1), 1–9. <https://doi.org/10.1038/s41467-020-18631-1>
- Lloret, F., Keeling, E. G., & Sala, A. (2011). Components of tree resilience: Effects of successive low-growth episodes in old ponderosa pine forests. *Oikos*, *120*(12), 1909–1920. <https://doi.org/10.1111/j.1600-0706.2011.19372.x>
- Madi Amer. (2020). *Quantifying water & carbon usage in a mosaic of ecosystems under dry Mediterranean climate*. Weizmann Institute of Science.
- Mariotti, A., Zeng, N., Yoon, J. H., Artale, V., Navarra, A., Alpert, P., & Li, L. Z. X. (2008). Mediterranean water cycle changes: Transition to drier 21st century conditions in observations and CMIP3 simulations. *Environmental Research Letters*, *3*(4). <https://doi.org/10.1088/1748-9326/3/4/044001>
- Marques, T. V., Mendes, K., Mutti, P., Medeiros, S., Silva, L., Perez-Marin, A. M., ... Bezerra, B. (2020). Environmental and biophysical controls of evapotranspiration from Seasonally Dry Tropical Forests (Caatinga) in the Brazilian Semiarid. *Agricultural and Forest Meteorology*, *287*(February), 107957. <https://doi.org/10.1016/j.agrformet.2020.107957>
- Martínez-Vilalta, J., Piñol, J., & Beven, K. (2002). A hydraulic model to predict drought-induced mortality in woody plants: An application to climate change in the Mediterranean. *Ecological Modelling*, *155*(2–3), 127–147. [https://doi.org/10.1016/S0304-3800\(02\)00025-X](https://doi.org/10.1016/S0304-3800(02)00025-X)
- Maseyk, K. (2006). *Ecophysiological and phenological aspects of Pinus halepensis in an arid-Mediterranean environment*. Weizmann institute.
- Maseyk, K., Hemming, D., Angert, A., Leavitt, S. W., & Yakir, D. (2011). Increase in water-use efficiency and underlying processes in pine forests across a precipitation gradient in the dry Mediterranean region over the past 30 years. *Oecologia*, *167*(2), 573–585.

<https://doi.org/10.1007/s00442-011-2010-4>

- Masson-Delmotte, V., P. Zhai, H.-O. Pörtner, D. Roberts, J. Skea, P.R. Shukla, A. Pirani, W. Moufouma-Okia, C. Péan, R. Pidcock, S. Connors, J.B.R. Matthews, Y. Chen, X. Zhou, M.I. Gomis, E. Lonnoy, T. Maycock, M. Tignor, and T. W. (2018). *IPCC, 2018: Global Warming of 1.5°C*.
- McAdam, S. A. M., & Brodribb, T. J. (2015). The evolution of mechanisms driving the stomatal response to vapor pressure deficit. *Plant Physiology*, 167(3), 833–843. <https://doi.org/10.1104/pp.114.252940>
- McDowell, N., Pockman, W. T., Allen, C. D., Breshears, D. D., Cobb, N., Kolb, T., ... Yezpez, E. A. (2008). Mechanisms of plant survival and mortality during drought: Why do some plants survive while others succumb to drought? *New Phytologist*, 178(4), 719–739. <https://doi.org/10.1111/j.1469-8137.2008.02436.x>
- Mielke, M. S., Oliva, M. A., De Barros, N. F., Penchel, R. M., Martinez, C. A., Da Fonseca, S., & De Almeida, A. C. (2000). Leaf gas exchange in a clonal eucalypt plantation as related to soil moisture, leaf water potential and microclimate variables. *Trees - Structure and Function*, 14(5), 263–270. <https://doi.org/10.1007/s004680050012>
- Muller, B., Pantin, F., Génard, M., Turc, O., Freixes, S., Piques, M., & Gibon, Y. (2011). Water deficits uncouple growth from photosynthesis, increase C content, and modify the relationships between C and growth in sink organs. *Journal of Experimental Botany*, 62(6), 1715–1729. <https://doi.org/10.1093/jxb/erq438>
- Muller, J. D., & Oz, I. (2021). *Branch-chamber-fluxes*. <https://doi.org/10.5281/ZENODO.5007008>
- Muller J and Oz I. (2021). *Branch-chamber-fluxes*. <https://doi.org/10.5281/ZENODO.4284487>
- Nadin, Ruehr, Rudiger Grote, S. M. and A. A. (2019). *beyond the extreme: recovery of carbon and water relations in woody plants following heat and drought stress.pdf*. *Tree Physiology*.
- Navrátil, M., Špunda, V., Marková, I., & Janouš, D. (2007). Spectral composition of photosynthetically active radiation penetrating into a Norway spruce canopy: The opposite dynamics of the blue/red spectral ratio during clear and overcast days. *Trees - Structure and*

- Function*, 21(3), 311–320. <https://doi.org/10.1007/s00468-007-0124-4>
- Nimmo, D. G., Mac Nally, R., Cunningham, S. C., Haslem, A., & Bennett, A. F. (2015). Vive la résistance: Reviving resistance for 21st century conservation. *Trends in Ecology and Evolution*, 30(9), 516–523. <https://doi.org/10.1016/j.tree.2015.07.008>
- Nogués, S., Munné-Bosch, S., Casadesús, J., López-Carbonell, M., & Alegre, L. (2001). Daily time course of whole-shoot gas exchange rates in two drought-exposed Mediterranean shrubs. *Tree Physiology*, 21(1), 51–58. <https://doi.org/10.1093/treephys/21.1.51>
- Novick, K. A., Ficklin, D. L., Stoy, P. C., Williams, C. A., Bohrer, G., Oishi, A. C., ... Phillips, R. P. (2016). The increasing importance of atmospheric demand for ecosystem water and carbon fluxes. *Nature Climate Change*, 6(11), 1023–1027. <https://doi.org/10.1038/nclimate3114>
- Posch, S., & Bennett, L. T. (2009). Photosynthesis, photochemistry and antioxidative defence in response to two drought severities and with re-watering in *Allocasuarina luehmannii*. *Plant Biology*, 11(SUPPL.1), 83–93. <https://doi.org/10.1111/j.1438-8677.2009.00245.x>
- Poulter, B., Frank, D., Ciais, P., Myneni, R. B., Andela, N., Bi, J., ... Van Der Werf, G. R. (2014). Contribution of semi-arid ecosystems to interannual variability of the global carbon cycle. *Nature*, 509(7502), 600–603. <https://doi.org/10.1038/nature13376>
- Preisler, Y. (2014). *Processes underlying tree mortality in semi-arid Aleppo pine forest following consecutive drought years*. Hebrew University of Jerusalem.
- Preisler, Y. (2020). *Water-use strategies leading to resilience of pine trees to global climatic change*. Hebrew University of Jerusalem.
- Preisler, Y., Tatarinov, F., Grünzweig, J. M., Bert, D., Ogée, J., Wingate, L., ... Yakir, D. (2019). Mortality versus survival in drought-affected Aleppo pine forest depends on the extent of rock cover and soil stoniness. *Functional Ecology*, 33(5), 901–912. <https://doi.org/10.1111/1365-2435.13302>
- Priestley, c. h. b., & Taylor, r. j. (1972). On the Assessment of Surface Heat Flux and Evaporation Using Large-Scale Parameters. *Monthly Weather Review*, 100(2), 81–92. [https://doi.org/10.1175/1520-0493\(1972\)100<0081:otaosh>2.3.co;2](https://doi.org/10.1175/1520-0493(1972)100<0081:otaosh>2.3.co;2)

- Pumpanen, J. S., Heinonsalo, J., Rasilo, T., Hurme, K. R., & Ilvesniemi, H. (2009). Carbon balance and allocation of assimilated CO₂ in Scots pine, Norway spruce, and Silver birch seedlings determined with gas exchange measurements and ¹⁴C pulse labelling. *Trees - Structure and Function*, 23(3), 611–621. <https://doi.org/10.1007/s00468-008-0306-8>
- Raupach, M. R., Canadell, J. G., & Le Quéré, C. (2008). Anthropogenic and biophysical contributions to increasing atmospheric CO₂ growth rate and airborne fraction. *Biogeosciences*, 5(6), 1601–1613. <https://doi.org/10.5194/bg-5-1601-2008>
- Raz-Yaseef, N., Yakir, D., Schiller, G., & Cohen, S. (2012). Dynamics of evapotranspiration partitioning in a semi-arid forest as affected by temporal rainfall patterns. *Agricultural and Forest Meteorology*, 157, 77–85. <https://doi.org/10.1016/j.agrformet.2012.01.015>
- Reichstein, M., Tenhunen, J. D., Rouspard, O., Ourcival, J. M., Rambal, S., Miglietta, F., ... Valentini, R. (2002). Severe drought effects on ecosystem CO₂ and H₂O fluxes at three Mediterranean evergreen sites: Revision of current hypotheses? *Global Change Biology*, 8(10), 999–1017. <https://doi.org/10.1046/j.1365-2486.2002.00530.x>
- Ruehr, N. K., Grote, R., Mayr, S., & Arneth, A. (2019). Beyond the extreme: recovery of carbon and water relations in woody plants following heat and drought stress. *Tree Physiology*, 1285–1299. <https://doi.org/10.1093/treephys/tpz032>
- Salmon, Y., Dietrich, L., Sevanto, S., Hölttä, T., Dannoura, M., & Epron, D. (2018). Drought impacts on tree phloem: From cell-level responses to ecological significance. *Tree Physiology*, 39(2), 173–191. <https://doi.org/10.1093/treephys/tpy153>
- Schwalm, C. R., Anderegg, W. R. L., Michalak, A. M., Fisher, J. B., Biondi, F., Koch, G., ... Tian, H. (2017). Global patterns of drought recovery. *Nature*, 548(7666), 202–205. <https://doi.org/10.1038/nature23021>
- Serra-Maluquer, X., Mencuccini, M., & Martínez-Vilalta, J. (2018). Changes in tree resistance, recovery and resilience across three successive extreme droughts in the northeast Iberian Peninsula. *Oecologia*, 187(1), 343–354. <https://doi.org/10.1007/s00442-018-4118-2>
- Speckman, H. N., Frank, J. M., Bradford, J. B., Miles, B. L., Massman, W. J., Parton, W. J., &

- Ryan, M. G. (2015). Forest ecosystem respiration estimated from eddy covariance and chamber measurements under high turbulence and substantial tree mortality from bark beetles. *Global Change Biology*, *21*(2), 708–721. <https://doi.org/10.1111/gcb.12731>
- Sperlich, D., Chang, C. T., Peñuelas, J., & Sabaté, S. (2019). Responses of photosynthesis and component processes to drought and temperature stress: Are Mediterranean trees fit for climate change? *Tree Physiology*, *39*(11), 1783–1805. <https://doi.org/10.1093/treephys/tpz089>
- Sprintsin, M., Cohen, S., Maseyk, K., Rotenberg, E., Grünzweig, J. M., Karnieli, A., ... Yakir, D. (2011). Long term and seasonal courses of leaf area index in a semi-arid forest plantation. *Agricultural and Forest Meteorology*, *151*(5), 565–574. <https://doi.org/10.1016/j.agrformet.2011.01.001>
- Stuart-Haëntjens, E., De Boeck, H. J., Lemoine, N. P., Mänd, P., Kröel-Dulay, G., Schmidt, I. K., ... Smith, M. D. (2018). Mean annual precipitation predicts primary production resistance and resilience to extreme drought. *Science of the Total Environment*, *636*(April), 360–366. <https://doi.org/10.1016/j.scitotenv.2018.04.290>
- Tal, A., & Billig, M. (2020). The impact of visits to dryland forests on environmental outlook: Results from a national survey. *Forests*, *11*(8), 1–15. <https://doi.org/10.3390/f11080872>
- Tatarinov, F., Rotenberg, E., Maseyk, K., Ogée, J., Klein, T., & Yakir, D. (2016). Resilience to seasonal heat wave episodes in a Mediterranean pine forest. *New Phytologist*, *210*(2), 485–496. <https://doi.org/10.1111/nph.13791>
- Thomas, C. K., Law, B. E., Irvine, J., Martin, J. G., Pettijohn, J. C., & Davis, K. J. (2009). Seasonal hydrology explains interannual and seasonal variation in carbon and water exchange in a semiarid mature ponderosa pine forest in central Oregon. *Journal of Geophysical Research: Biogeosciences*, *114*(4), 1–22. <https://doi.org/10.1029/2009JG001010>
- Tsamir, M., Gottlieb, S., Preisler, Y., Rotenberg, E., Tatarinov, F., Yakir, D., ... Klein, T. (2019). Stand density effects on carbon and water fluxes in a semi-arid forest, from leaf to stand-scale. *Forest Ecology and Management*, *453*(June), 117573. <https://doi.org/10.1016/j.foreco.2019.117573>

- Tuovinen, J.-P. (2006). Foliage surface ozone deposition: a role for surface moisture? *Biogeosciences Discussions*, 2(6), 1739–1793. <https://doi.org/10.5194/bgd-2-1739-2005>
- Tyree, M. T., & Sperry, J. S. (1989). Cavitation and Embolism. *Water*, 19–38. <https://doi.org/10.1146/annurev.pp.40.060189.000315>
- Väänänen, P. J., Osem, Y., Cohen, S., & Grünzweig, J. M. (2020). Differential drought resistance strategies of co-existing woodland species enduring the long rainless Eastern Mediterranean summer. *Tree Physiology*, 40(3), 305–320. <https://doi.org/10.1093/treephys/tpz130>
- Vesala, T., Sevanto, S., Grönholm, T., Salmon, Y., Nikinmaa, E., Hari, P., & Hölttä, T. (2017). Effect of leaf water potential on internal humidity and CO₂ dissolution: Reverse transpiration and improved water use efficiency under negative pressure. *Frontiers in Plant Science*, 8(FEBRUARY), 1–10. <https://doi.org/10.3389/fpls.2017.00054>
- von Caemmerer, S., & Farquhar, G. D. (1981). Some relationships between the biochemistry of photosynthesis and the gas exchange of leaves. *Planta*, 153(4), 376–387. <https://doi.org/10.1007/BF00384257>
- Wang, H., Gitelson, A., Sprintsin, M., Rotenberg, E., & Yakir, D. (2020). Ecophysiological adjustments of a pine forest to enhance early spring activity in hot and dry climate. *Environmental Research Letters*, 15(11). <https://doi.org/10.1088/1748-9326/abc2f9>
- Ye, Z. P., & Yu, Q. (2008). A coupled model of stomatal conductance and photosynthesis for winter wheat. *Photosynthetica*, 46(4), 637–640. <https://doi.org/10.1007/s11099-008-0110-0>
- Yu, F.-H., Roiloa, S. R., & Alpert, P. (2016). Editorial: Global Change, Clonal Growth, and Biological Invasions by Plants. *Frontiers in Plant Science*, 7, 1467. <https://doi.org/10.3389/fpls.2016.01467>
- Ziv, B., Saaroni, H., Pargament, R., Harpaz, T., & Alpert, P. (2014). Trends in rainfall regime over Israel, 1975–2010, and their relationship to large-scale variability. *Regional Environmental Change*, 14(5), 1751–1764. <https://doi.org/10.1007/s10113-013-0414-x>

7. Supplementary information

Pictures of the branch chambers



Figure s1. Pictures of the branch chamber located in the mid-canopy, at ~6 m height (left) and a close look at the branch chamber (right).

Schematic diagram of the experimental chamber setup

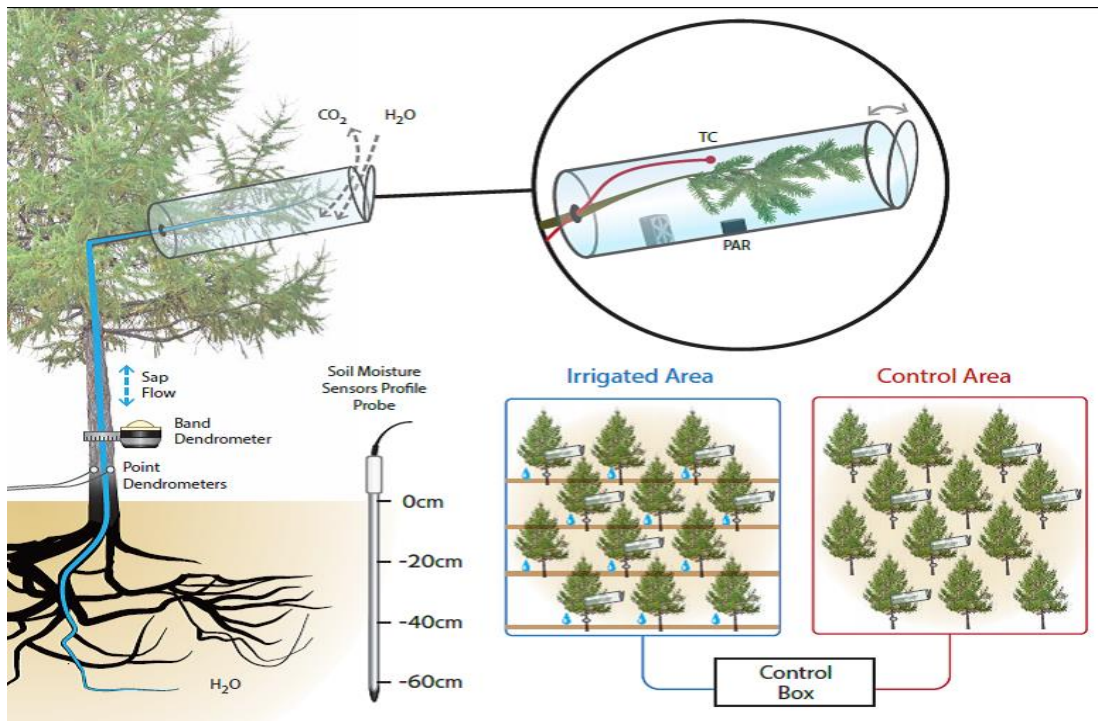


Figure s2. Experimental setup illustration showing the two plots in the right bottom corner, the profile soil humidity sensor at the middle, sap flow and dendrometer on the tree stems (data not shown in this study) and the branch chamber located on the tree. On the upper right corner, a focused illustration of the branch chamber components including TC, fan and PAR sensor (actually located outside of the chamber).

Schematic diagram of the branch chamber setup

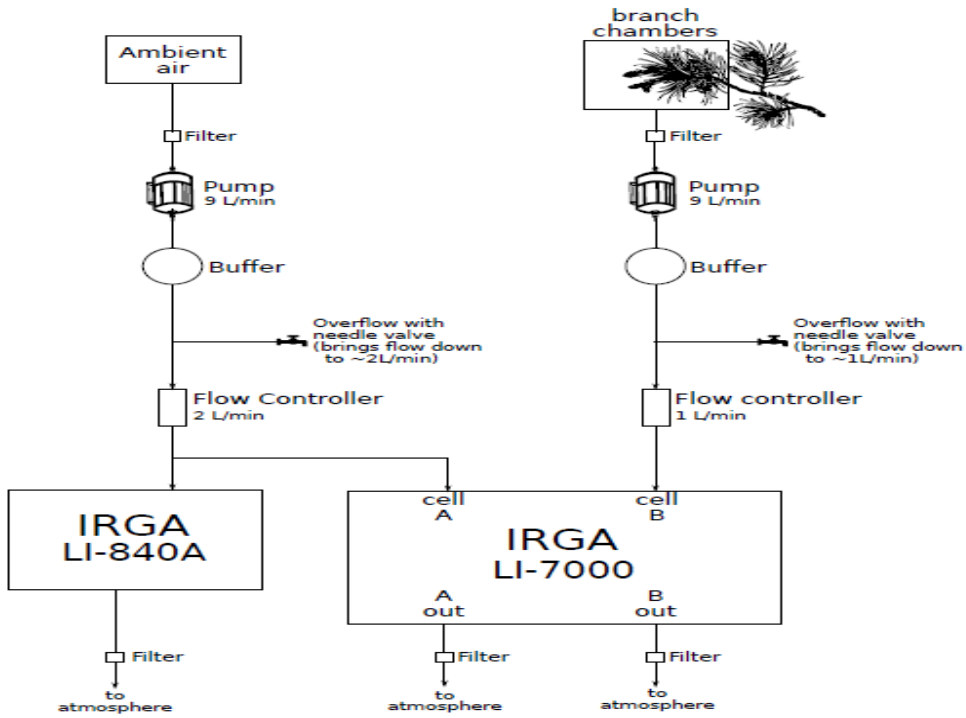


Figure s3. Diagram of the gas exchange branch chambers setup. Note that for simplification the setup is shown for one sample chambers, but was extended to 14 chambers of both plots. The air flows from the measuring chamber through the filter, pump, buffer tube, flow meter, flow controller and finally in to the measurement cell inside the IRGA (either the Li-840A or the Li-700 –cell A/B). The direction of the airflow is indicated by the small arrows.

List of variables

Table s1. List of output variables from the branch chamber system

variable	units	variable	units
TIMESTAMP	“yy:mm:dd:hh:ss”	Co2_Flux	$\mu\text{mol} \cdot \text{m}^{-2} \cdot \text{s}^{-1}$
H2o_840	$\text{mmol} \cdot \text{mol}^{-1}$	PAR_chamber	$\mu\text{mol} \cdot \text{m}^{-2} \cdot \text{s}^{-1}$
Co2_840	$\mu\text{mol} \cdot \text{mol}^{-1}$	AirFlow_Sample	LPM
H2o_7000	$\text{mmol} \cdot \text{mol}^{-1}$	AirFlow_ambient	LPM

Co2_7000	$\mu\text{mol} * \text{mol}^{-1}$	Ambient_RH	%
Temp_840	$^{\circ}\text{C}$	Ambient_TempAir	$^{\circ}\text{C}$
Temp_7000	$^{\circ}\text{C}$	Tc(1:16)	$^{\circ}\text{C}$
Prees_7000	Pa	PAR_ambient	$\mu\text{mol} * \text{m}^{-2} * \text{s}^{-1}$
H2o_Flux	$\text{mmol} * \text{m}^{-2} * \text{s}^{-1}$	ChamberON	No.
Counter	seconds	VPD_Ambient/chamber	KPa

Branch chambers flushing time

To make sure that the flushing time is sufficient we made sure the delta concentration in each measurement reaches steady state. After checking the time it takes to reach steady state in different environmental conditions (high RH, high/ low activity, etc.) a clear flushing time of 210 seconds was determined. The data used for the final calculation is the average of the last 30

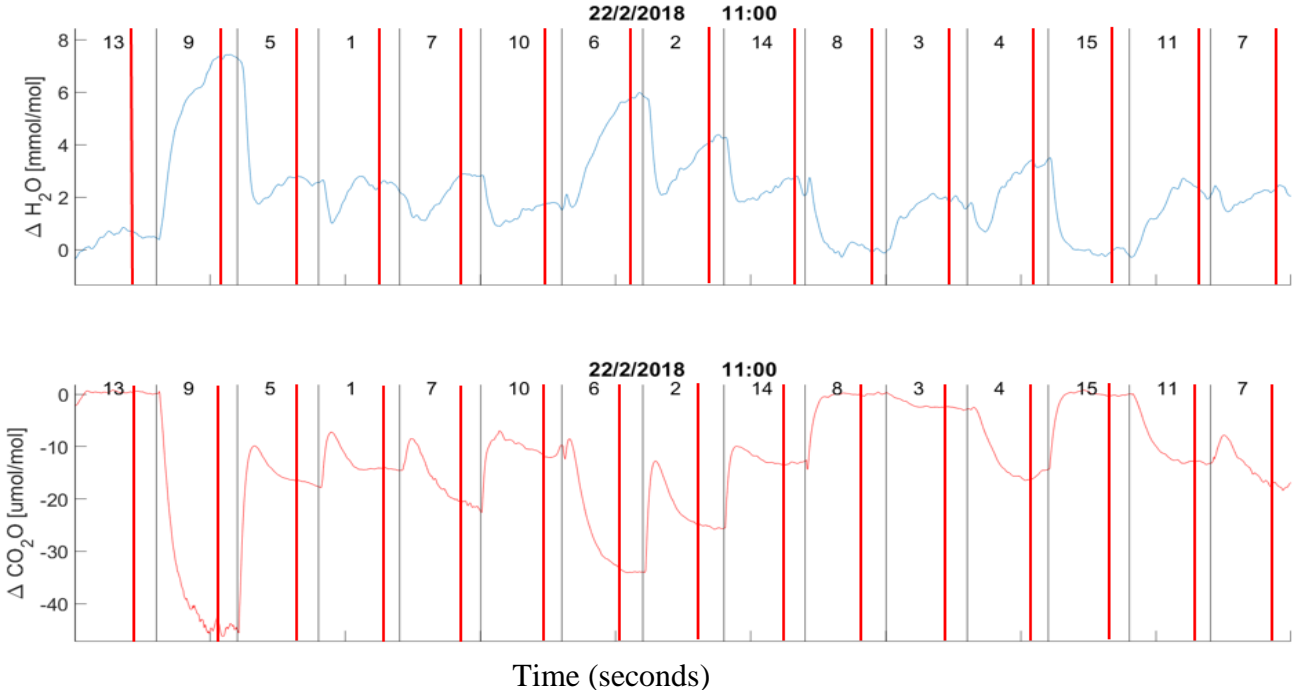
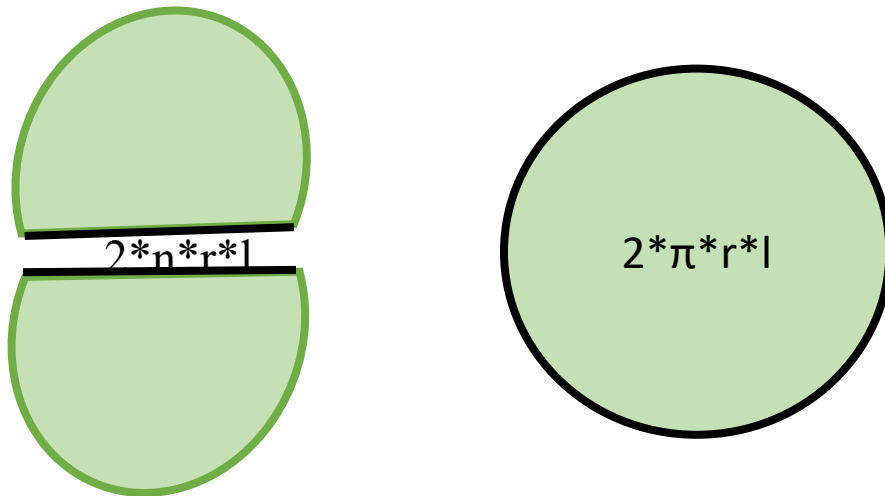


*Figure s4. Example of flushing times from all the different chambers at the 22 of February 2018. In the Y axis is the $\Delta\text{H}_2\text{O}$ ($\text{mmol} * \text{mol}^{-1}$) for the upper panel and ΔCO_2 ($\mu\text{mol} * \text{mol}^{-1}$) for the lower one. The X axis is time in seconds divided to 240 seconds sections by the gray horizontal lines. The red horizontal lines represents the last 30 seconds of each chamber measurement. The numbers at the top of each measurement section represent the chamber number.*

Total leaf area surface calculation



$$\text{Surface area (m}^2\text{)} = ((2 * \pi * r * l + 2 * n * r * l)) * (N)$$

Figure s5. Visual description of needle surface area. The black lines represent the surfaces that we take in account for the leaf area surface calculation. The formula in each of the drawings represent their part in the general equation. Where r is average needle radius (m), l is average length of needle in cuvette (m), n is number of needles in the fascicle and N is the number of fascicles.

Experimental setup for PPFD redaction by LA



Figure s6. Experimental setup for PPFD redaction by LA. 2 PAR sensors were used, one inside at the bottom of the chamber and one is outside next to the chamber. 3 twigs are inside the chamber, shading the PAR sensor at the bottom of the chamber.

Measurement of both sensors out of the chamber

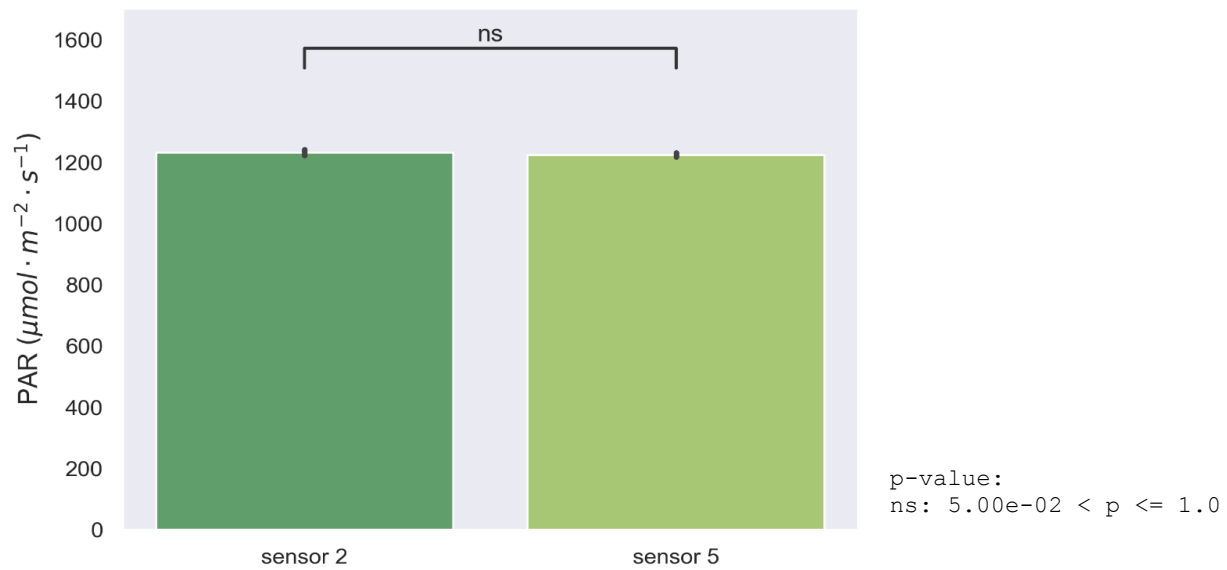


Figure s7. Incoming PPFD of the two sensors used for the experiment. The results shown are for the two sensors outside the chamber. X axis is the different sensors and Y axis is PAR. Value shown are the average \pm stdv of 5 measurement of both sensors, each measurement is the average of one minute. The two sensors showed no statistically significant difference. Significant difference given * (ANOVA, t-test $P \leq 0.05$).

Photos perspective correction

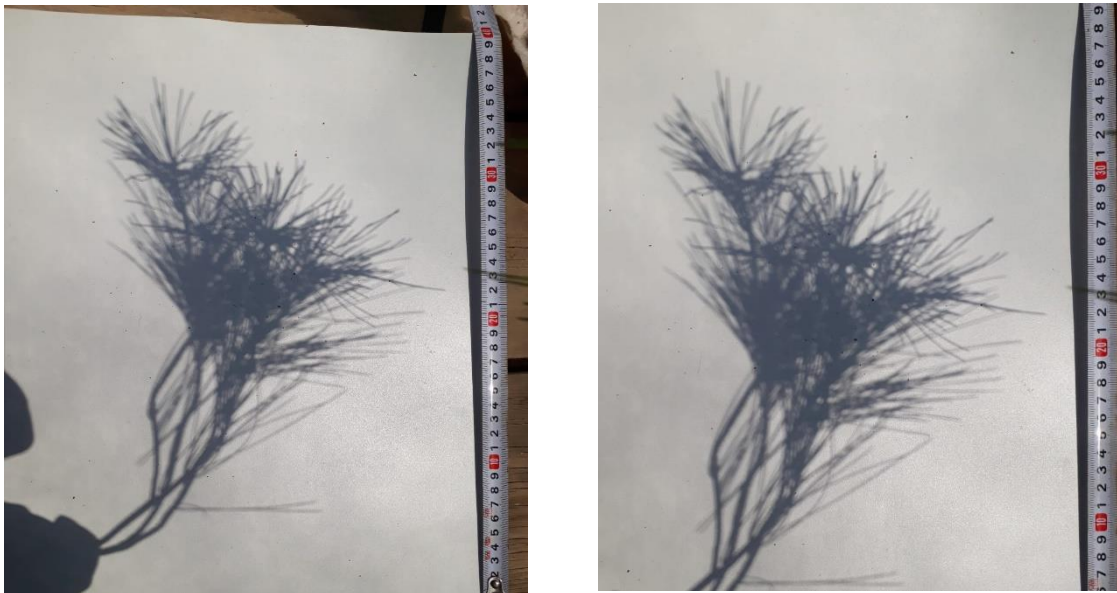


Figure s8. Image correction for image based leaf area correction. The shade casted by the four twigs as they arranged in the chamber before (left) and after (right) the image correction.

Photos after object detection

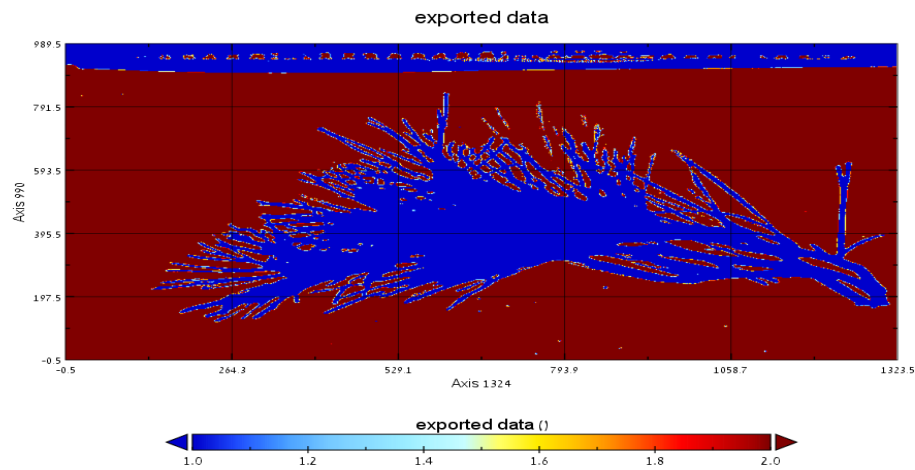


Figure s9. Twigs shade pixel classification. X & Y axis denotes the length of axis in pixels. The color bar shows the numeric classification by color. Data is calculated from the last pixels line containing blue pixels of the measuring tape.

Effective leaf area from image based correction

Effective leaf area obtained by image based correction (ELA_p) when using different leaf area quantification methods. Fig s10 shows the correlation between ELA_p of TLSA and projected_2D.

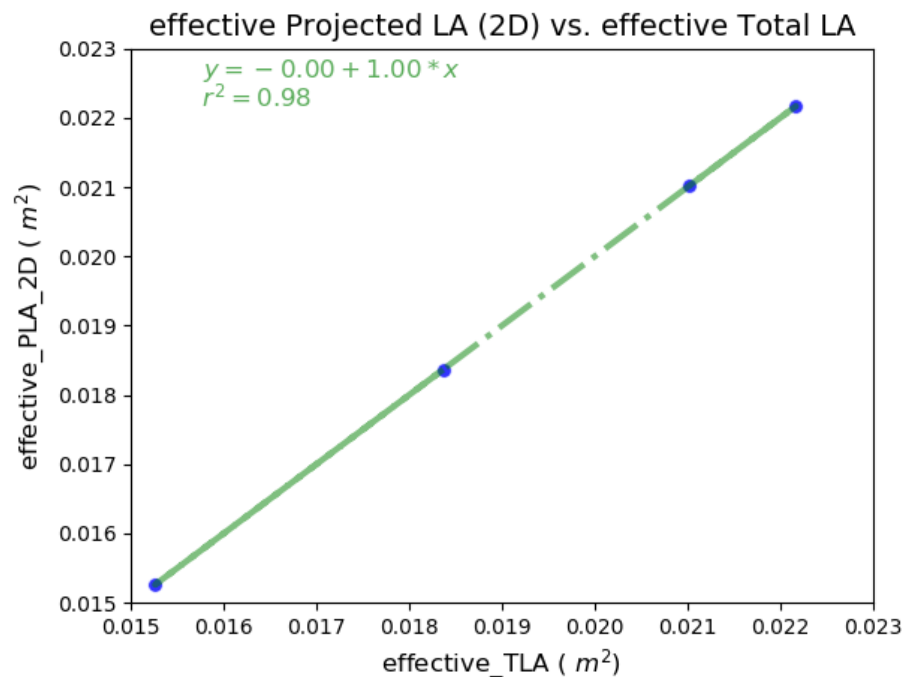


Figure s10. Correlation between image based leaf area (ELA_p) calculated based on both TLSA (X axis) and projected_2D (Y axis).

Environmental variables for li-cor 6400 campaign

Environmental variables comparison between full to half chamber measurements for li-cor 6400 campaign. Significant treatment effects are given (ANOVA, t-test $P \leq 0.05$).

Table S2. Environmental conditions difference between full and half chamber in li-cor 6400

<i>Variable</i>	<i>n</i>	<i>Mean difference</i>	<i>Std dev</i>	<i>P-value</i>
Temp. difference	12	1	0.01	$P < 0.05$
VPD difference	12	0.983	0.08	$P < 0.05$
PAR difference	12	0.99	0.0009	$P < 0.05$

Light response curve

Anet and E response to PPFD with different LA calculations to our benchmark, LI-COR6400 (corrected and not corrected) (Fig. s11). Comparison to the LI-COR 6400 was done only for Anet since Temperature, RH and therefore VPD were constant throughout the measurement so no significant change in E was observed. Anet values from the branch chambers calculated with different LA quantification methods showed that maximal rate ($Anet_{max}$) was the highest and most similar to the corrected values of the LI-COR 6400 when using the ELA_p (IBLA) correction or the ELA_f (FBLA) correction (Fig. s11 a). Slope (α) was also highest and show similar results to the corrected values of the LI-COR 6400 when using the ELA of the two methods (Table ; Fig. s11).

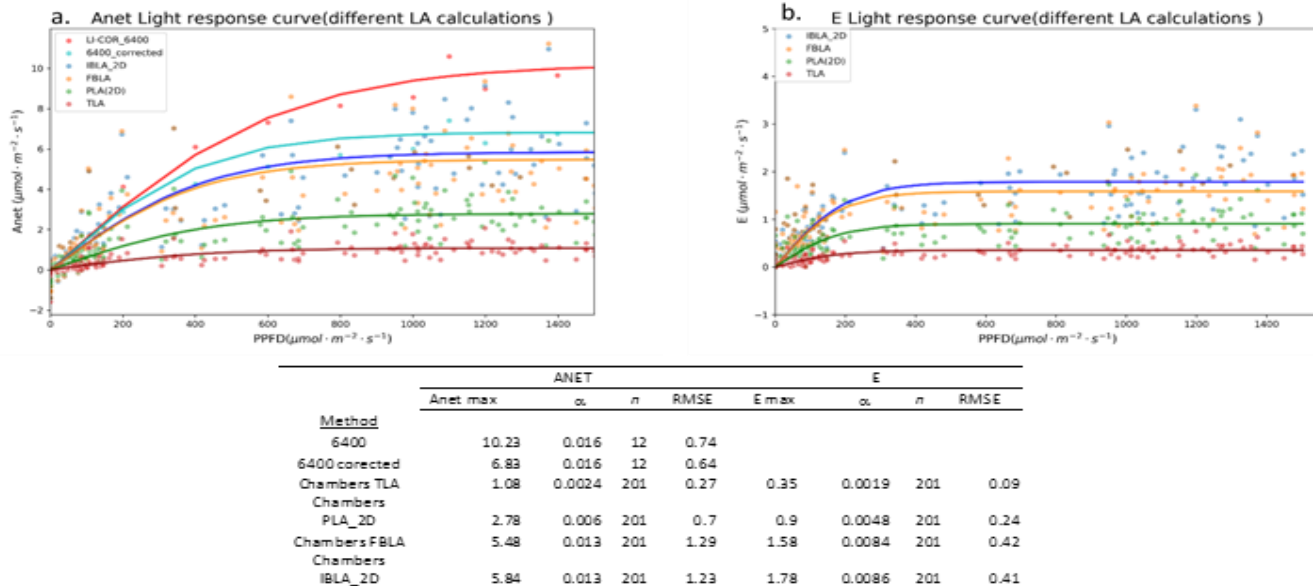


Figure. s11 Light response curve of: a) Photosynthesis (Anet) and b) Transpiration (E) vs. Photosynthetic Photon Flux Density (PPFD) calculated based on different LA corrections. Image based corrected LA (IBLA_2D; Blue), flux based corrected projected Leaf Area (FBLA; Orange), li-cor 6400 (Red), li-cor 6400 corrected (Light blue), Total LA (TLA; Dark red), and Projected LA (PLA_2D; green). Branch chambers data includes values from all chamber in the irrigated plot (n=6) from September to November 2020 data was filtered to match the conditions of LI-COR 6400 measurements in terms of Temperature and VPD range. LI-COR 6400 values are the average of two campaign days in September and October also from the irrigated plot. The table summarizes the parameters and statistics of the J model for both Anet and E. First column for each variable is the maximal activity rate, second column (α) is the response rate (slope of linear part) and finally two last columns are the sample size (n) and the root mean square error which represent the error of the model.

PAR sensor calibration setup (in vs. outside the chamber)



Figure s12. Calibration setup for the PAR sensors

Calibration curve (in vs. outside the chamber)

We found that PPFD measured outside of the chamber is higher by ~13%. This value is used in the analysis script to correct the PPFD values we are measuring outside of the chamber.

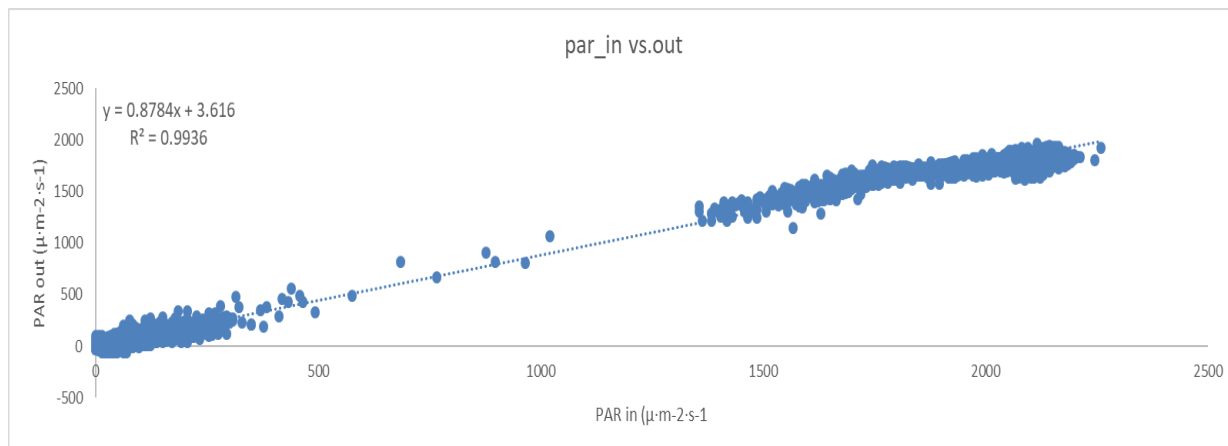


Figure s13. PAR sensor Calibration between outside the chamber (X axis) and in the chamber (Y axis). Data for calibration is from the 10's to the 13's of July 2020. Each point in the graph is one minute average from both sensors.

Environmental variables (PAR and VPD) - twigs removal experiment

VPD and PAR maximum difference and range within a chambers measurement were use to filter out bad data. No measurement exceeded the VPD threshold. PAR values were filtered from measurement where delta was higher than the threshold and range was lower from its threshold. The last column denotes how many good measurement we had for each chamber each day.

Table s3. Environmental variables in the twigs removal experiment.

day	light	chamber	Max Delta PAR	Max Delta VPD	Good measurements
1	lit	2	124	0.3	4
2	lit	2		0.2	0
3	lit	2	24	0.8	0
4	lit	2	132	0.3	4
5	lit	2	830	0.5	1
1	lit	5	100	0.9	4
2	lit	5	133	0.4	4
3	lit	5		0.1	1
4	lit	5	31	0.1	4
5	lit	5	49	0.4	3

day	light	chamber	Max Delta PAR	Max Delta VPD	Good measurements
1	shaded	3	124	0.4	0
2	shaded	3	127	0.1	2
3	shaded	3	584	0.2	0
4	shaded	3	38	0.3	4
5	shaded	3	118	0.1	0
1	shaded	6	23	0.4	4
2	shaded	6	72	0.3	2
3	shaded	6	10	0.1	0
4	shaded	6		0.1	0
5	shaded	6	55	0.5	0

Residual comparison for α determination

We compared the average residual value of each variable for the four years of measurements in order to quantify how noisy is the data comparing to the least noisy data set (Anet, average residual =5%). The average residual for the four years of branch conductance (gb) was almost the same as for the Anet (4.7%) while for the Transpiration (E) it was higher (7.1%). Ther for we didn't change α for season detection for the gb but we did change it for E detection ($\alpha=4$).

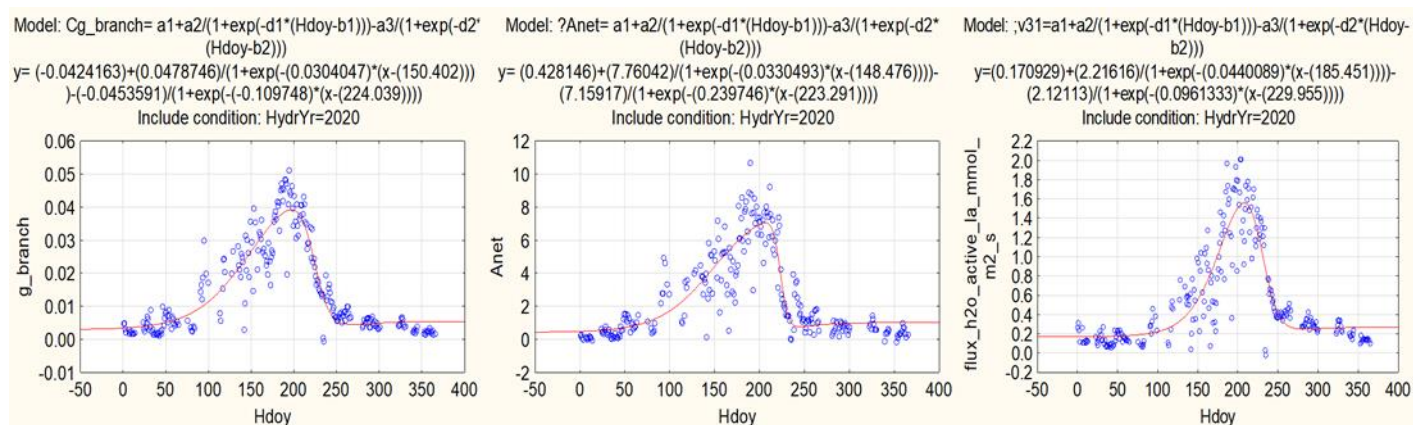


Figure s14. Example of the fitted model by variable for 2020. E (Flux h2o(mmol-m-2-s-1), right panel), Anet (($\mu\text{mol-m-2-s-1}$, central panel) and gb (mol-m-2-s-1 , left panel)- all in Y axis by the hydrological day of year(Hdoy) in the X axis. Blue points denotes daily averages and red lines represent the fitted modeled curve. All models were significant (p -value <0.05). Above each figure is the model equation and r^2 .

Table s4. Models ditales and statistics

Year	Var Y	R ²	Eqn	Sum of Squares	DF	Mean Squares	F-value	p-value
2017	E		0.83 Gonsamo	31.59	7	4.512615	397.0605	0.00
2018	E		0.76 Gonsamo	19.39	7	2.769869	221.7361	0.00
2019	E		0.80 Gonsamo	11.36	7	1.623023	354.4283	0.00
2020	E		0.80 Gonsamo	136.37	7	19.48091	348.5730	0.00
2017	Anet		0.89 Gonsamo	Matlab				
2018	Anet		0.70 Gonsamo	Matlab				
2019	Anet		0.78 Gaussian	575.95	4	143.9869	255.1973	0.00
2020	Anet		0.80 Gonsamo	3095.57	7	442.2245	317.0662	0.00
2017	gb		0.90 Gonsamo	0.05	7	0.007056	532.9818	0.00
2018	gb		0.74 Gonsamo	0.02	7	0.002738	202.6929	0.00
2019	gb		0.79 Gaussian	0.02	4	0.004260	318.7347	0.00
2020	gb		0.87 Gonsamo	3095.57	7	442.2245	317.0662	0.0000

Light saturation detection of E and Anet

Light response curves for both Anet and E from the branch chambers. Using curve_expert software, the best fit line was created for each data set. The point of PPFd saturation was determined as a point where the derivative of the fitted line is less than 0.01 for Anet and below 0.001 for E.

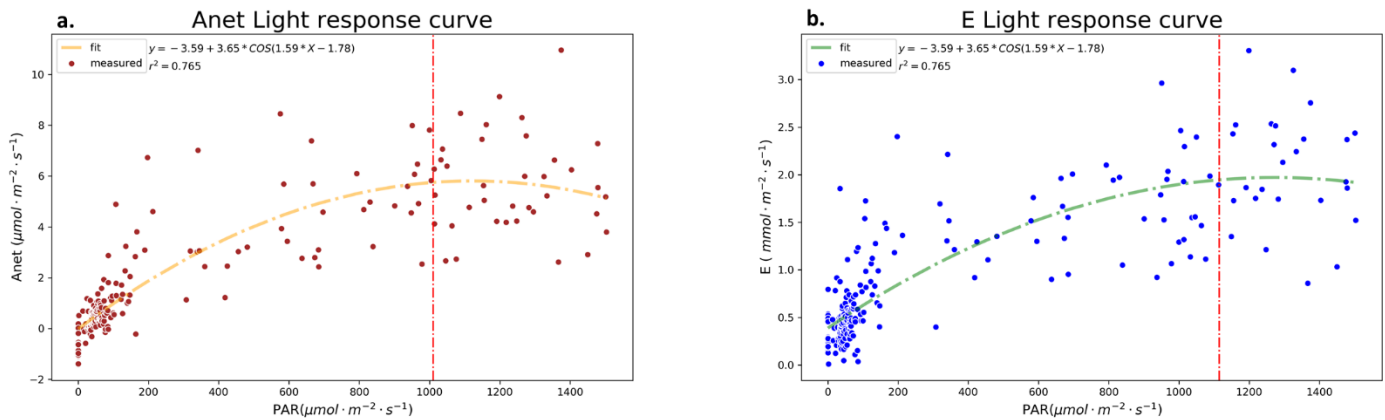


Figure s15. Light response curves for: a) photosynthesis (Anet) and b) transpiration (E): for both panel a and b the X axis shows the incoming Photosynthetic Photon Flux Density (PPFD) in the chamber and the red dashed line shows the saturation limit ($f'(X) < 0.001$). The points for the two panels shows the measured values while the lines sows the best fit for the two data sets. Data for both panels is from September to November 2020 from all chambers of irrigated plot ($n=6$).

Comparison of Anet and E for the two correction methods (IBLA_2D and FBLA)

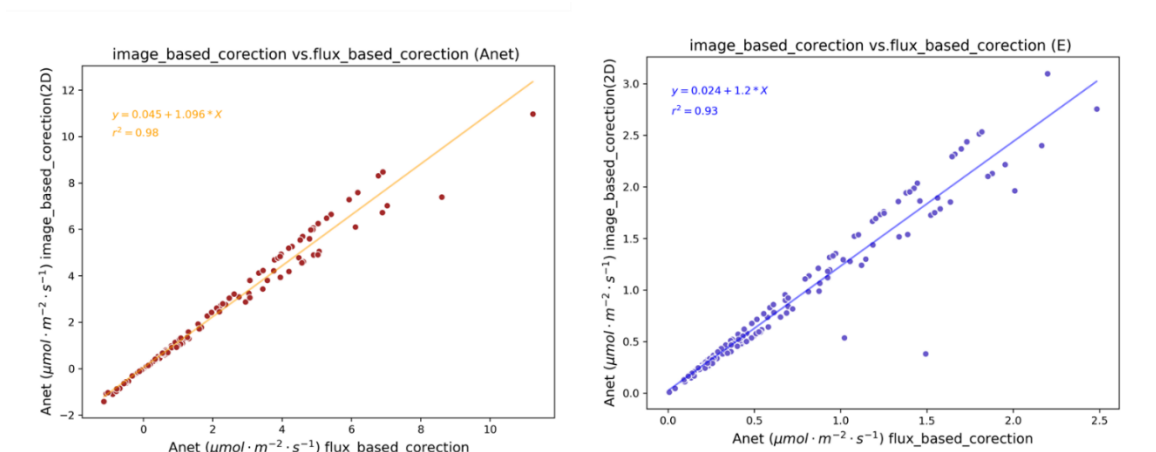


Figure s16. Correlation between Image Based Leaf Area (IBLA_2D) correction and Flux Based Leaf Area (FBLA) correction for: a) Anet and b)E. 2D represent two needles per fascicle (2 diameters) as the projected area. Data is from all chamber (n=6) of the irrigated plot between September to November 2020.

Gas exchange response to VPD (SWC > tSWC)

We found that when SWC is high transpiration (E) does not decrease in response to VPD increase in appose to Photosynthesis (Anet) and branch conductance (gb) that do decrease at ~ 3.4 KPa.

The decrease was considered as 10% or more change from the maximum.

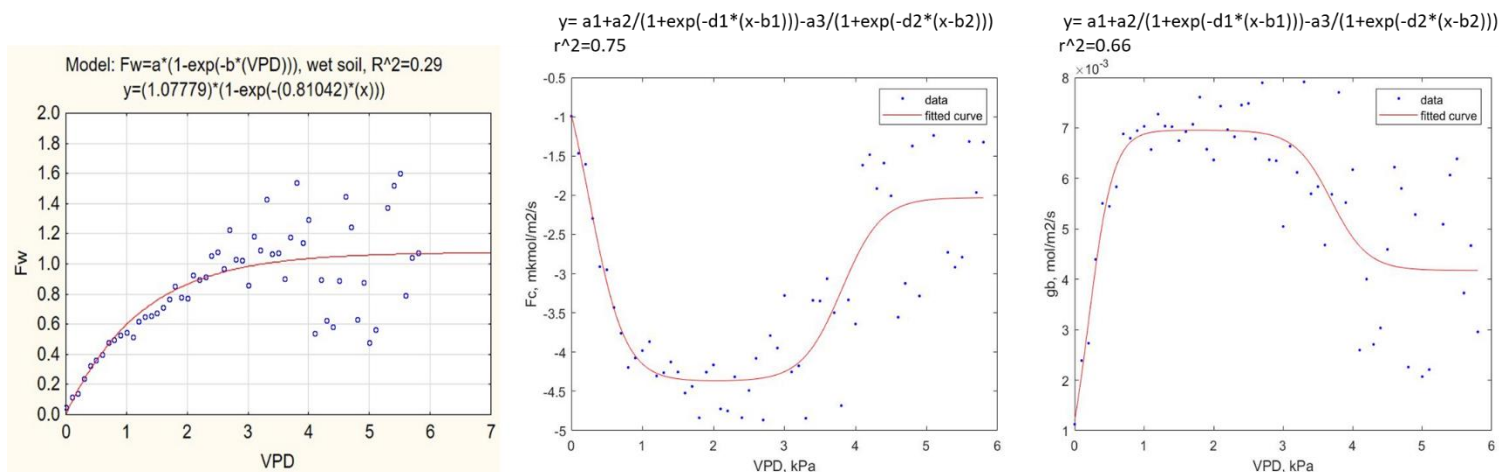


Figure s17. VPD response of leaf gas exchange: E (FW(mmol·m⁻²·s⁻¹), left panel), Anet (Fc(μmol·m⁻²·s⁻¹), central panel) and gb (mol·m⁻²·s⁻¹, right panel)- all in Y axis in response to binned VPD (KPa) in the X axis. All models were significant (p-value <0.05). Above each figure is the model equation and r².

Gas exchange response to VPD (SWC < tSWC)

We found that when SWC is low transpiration (E) still does not decrease in response to VPD increase in appose to Photosynthesis (Anet) and branch conductance (gb) that do decrease at ~1.4 KPa. The decrease was considered as 10% or more change from the maximum.

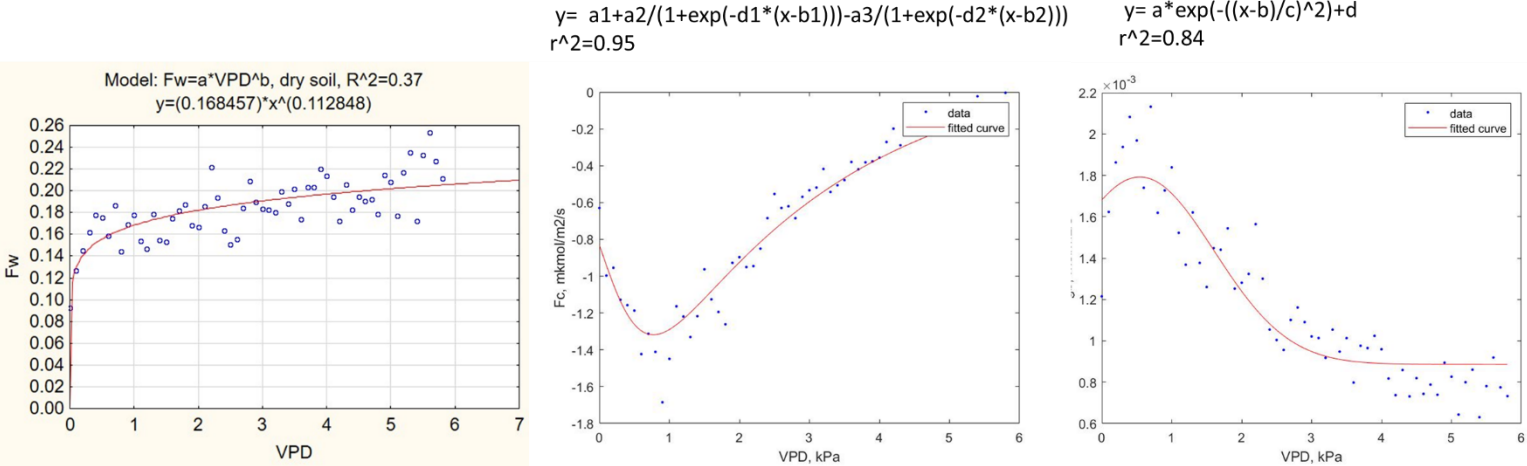


Figure s18. VPD response of leaf gas exchange : E (FW(mmol-m-2-s-1), left panel), Anet (Fc(μmol-m-2-s-1), central panel) and gb (mol-m-2-s-1, right panel)- all in Y axis in response to binned VPD (KPa) in the X axis. All models were significant (p-value <0.05). Blue points denotes daily averages and red lines represent the fitted modeled curve. Above each figure is the model equation and r².

Rain amount and its effect on the SWC 1m depth

SWC at 1m depth changed significantly in four out of eight years at the time of SWC measurements at this depth. The significant increases in SWC occurred in the winters of 2013-14, 2014-15, 2016-17 and 2019-20 (Note that data of the winter 2017-28 and part of the peak of 2019-

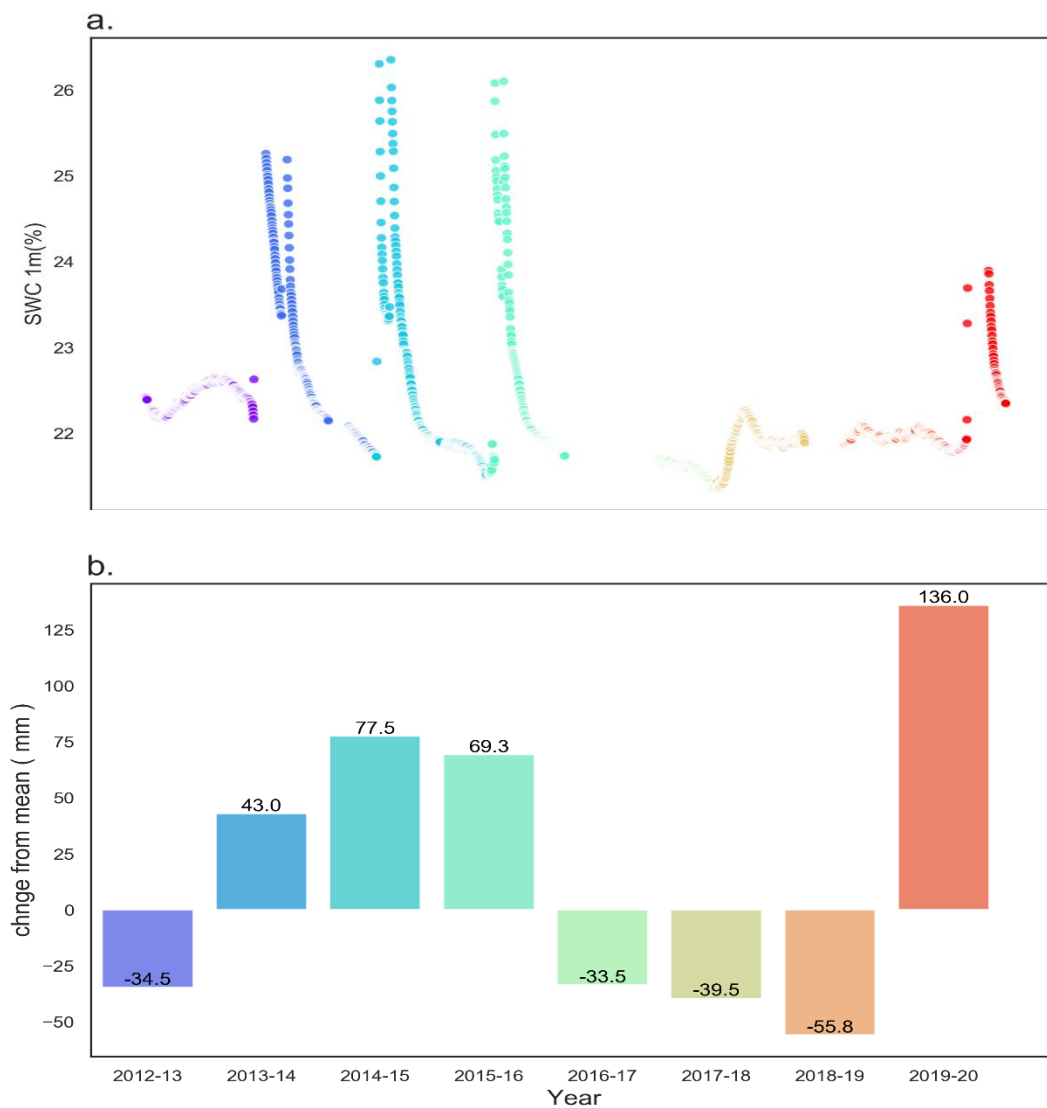


Figure 19. Soil water content (SWC) in 1m depth from 2012-13 winter until 2019-20 winter (a), and the change of precipitation amount from the long-term average (279 ± 90 mm) for the same winters. Different colors represent the different years in both subplots. Data for SWC is based on two sensors at 106 and 125 cm. Precipitation amount is from the meteorological station in "Bet hayaran" located in Yatir forest.

20 are missing) (Fig. s19). The significant changes observed in the SWC at a depth of 1m were correlated with the amount of precipitation that winter

Temperature decries in 2017

The drop below the 30 °C threshold after which the temperature did not return to summer temperature occurred at DOY 259, on the same day of the rise in Anet and the day after the end of the maximum VPD period.

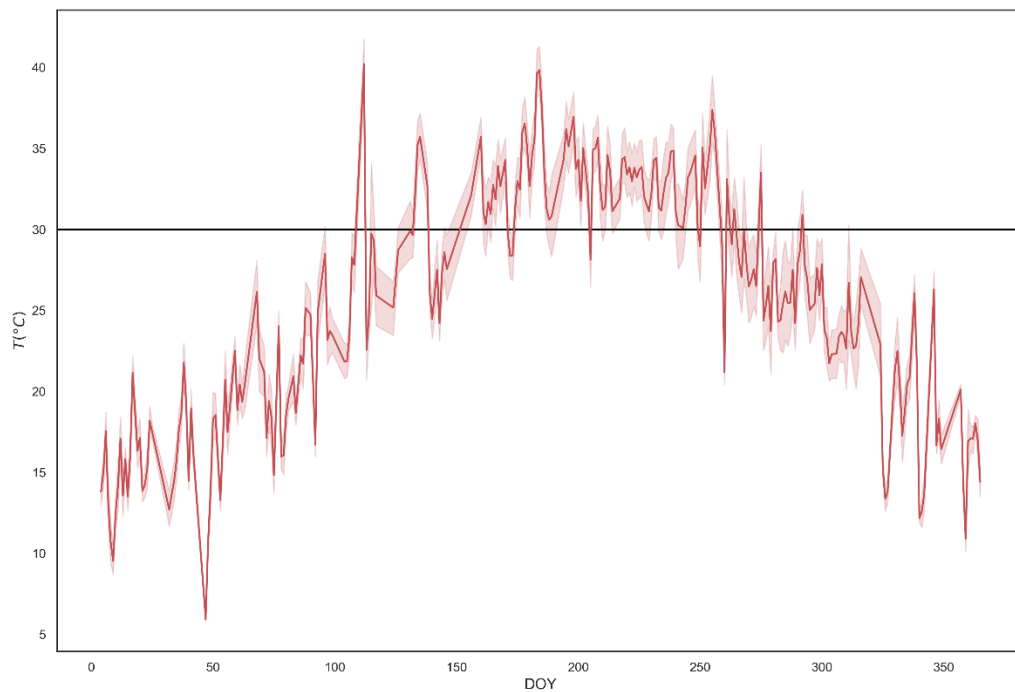


Figure s20. Air temperature adjacent to the leaves inside the branch chambers. Red line shows the day-time average of the temperature in 2017. Black horizontal line represents the upper temperature value of the optimum, above which an increase in temperature causes a decrease in activity.

VPD comparison for the peak activity period

VPD of the peak period in the different years ranged between 1.4 ± 0.8 in 2019 which was the lowest, to 1.6 ± 0.6 and 2 ± 0.8 in 2017 and 2018 respectively up to 2.4 ± 0.9 in 2020 when the peak was the latest in the year (Fig s.21 a). Temperature (T) showed similar relationships between the peak period of the different years when T in 2019 and 2017 were statistically similar and the least hot with values of 18.5 ± 3.79 and 20 ± 2.8 respectively, 2018 was warmer with average temperature of 24.5 ± 4.1 and 2020 peak period was the warmest with average temperature of 27.6 ± 3.5 (Fig s.21 b).

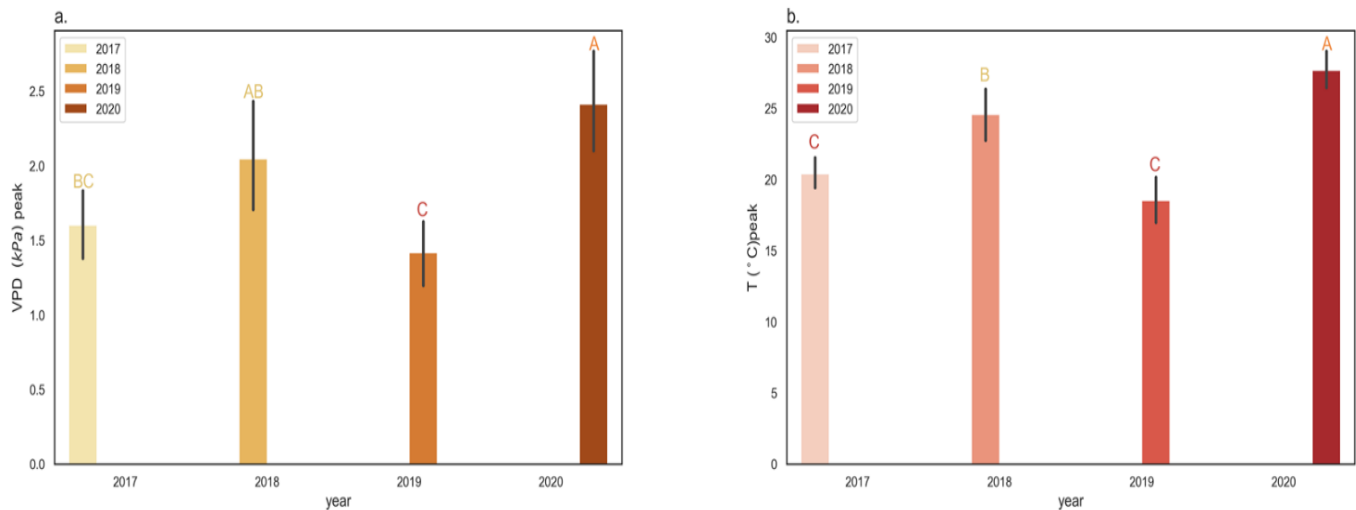


Figure s21. VPD (kPa) and T(°C) at the peak activity period of the different years. Bars showing the average VPD (a) or T (b) \pm STDEV of the 90th percentile for each year. Different letters represent statistical differences between sample groups (LSMeans Differences Tukey HSD test, $p < 0.05$).

Pre-dawn Ψ_w comparison for the peak activity period of 2018 and 2019

Average Ψ_w of the peak activity was calculated based on monthly values that corresponded with the months of peak LGE. In 2019 peak activity period Ψ_w was lower in ~36%.

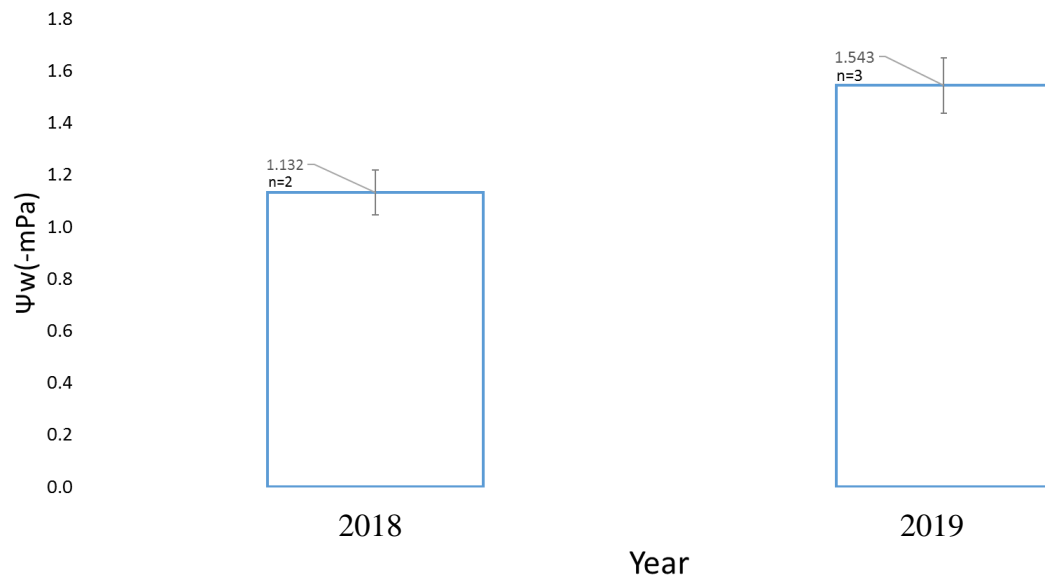


Figure s22. Leaf water potential (Ψ_w , -mPa) at the peak activity period of 2018 and 2019. Bars showing the average VPD (a) or T (b) \pm STDEV.